ABSTRACT

Title of Dissertation: STRATEGIES FOR ENHANCING PERFORMANCE OF FLAPPING WING AERIAL VEHICLES USING MULTIFUNCTIONAL STRUCTURES AND MIXED FLIGHT MODES

Alex E. Holness

Directed by: Professor Hugh A. Bruck
Department of Mechanical Engineering

Biological flapping wing flight offers a variety of advantages over conventional fixed wing aircraft and rotor craft. For example, flapping propulsion can offer the speed of fixed wing aircraft at similar scales while providing the maneuverability of rotor craft. Avian species easily display feats of perching, payload carrying, endurance flying, and transition behavior. In light of these characteristics, emulating and recreating flapping flight in biomimetic or bioinspired work is important in the development of next generation aerial systems. Unfortunately, recreating flapping wing flight is not easily achieved despite numerous efforts to do so. This is in large part due to technological deficiencies. With emerging technologies, it has been possible to begin to unravel the intricacies of flapping flight. Despite technological advancements, offsetting weight with mechanical systems robust enough to provide power and torque while sustaining loading remains difficult. As a result platforms either have simple flapping kinematics with fair payload or have more complex kinematics with limited excess power which in turn limits payload. The former limits capabilities to mirror biological performance characteristics and the latter limits the energy available to power flight which ultimately negatively impacts

mission capabilities. Many flapping wing systems are subpar to traditional flying vehicles. Flapping systems can become more competitive in achieving various mission types with increased system performance. In particular, if endurance is coupled with desirable features such as those displayed in nature, i.e., avian perching, they may become superior assets. In this work, four strategies for increasing performance were pursued as follows: (1) increases to maneuverability and payload via a mixed mode approach of flapping wing used in conjunction with propellers, (2) rapid deceleration and variation of flight envelope via inertial control using the battery, (3) increased endurance via integrated energy storage in the wings, and (4) providing endurance to the point of complete energy autonomy using a design framework considering flapping wings with integrated high efficiency solar cells.

STRATEGIES FOR ENHANCING PERFORMANCE OF FLAPPING WING AERIAL VEHICLES USING MULTIFUNCTIONAL STRUCTURES AND MIXED FLIGHT MODES

by

Alex E. Holness

Dissertation submitted to the Faculty of the Graduate School of the
University of Maryland, College Park in partial fulfillment
of the requirements for the degree of
Doctor of Philosophy
2018

Advisory Committee:
Professor Hugh Bruck, Chair/Adviser
Professor Abhijit Dasgupta
Professor Martin Peckerar, Deans Representative
Professor Miao Yu
Professor Satyandra K. Gupta

Dedication

This work is dedicated my family, friends, educational staff members, supporters and to those who seek to learn and explore despite setbacks, failures, challenges, varying levels of support, limited representation, and difficulties.

Acknowledgement

Thank you to my immediate family, extended family, friends, academic staff, fellow lab members, colleagues, and supporters who have provided encouragement and support. Thank you to my advisor Dr. Hugh Bruck and project co-advisor Dr. S.K. Gupta. This work was supported by a National Science Foundation (NSF) Bridge to Doctoral (BD) graduate fellowship granted via the University of Maryland, College Park Center for Minorities in Science and Engineering and AFOSR grant FA9550-15-1-0350 with Dr. Byung-Lip 'Les' Lee as program manager. Thank you to the Meyerhoff Scholarship program at the University of Maryland, Baltimore County (UMBC) for steering me towards this path and to the many mentors who invited me into their laboratories during my undergraduate studies.

Contents

List of Figures

List of Tables

Abbreviations

A-Si	**A**morphous **S**ilicon
ELO	**E**pitaxial **L**ift-**O**ff
FWUAV	**F**lappping **W**ing **U**nmanned **A**erial **V**ehicle
FWAV	**F**lappping **W**ing **A**erial **V**ehicle
GaAs	**G**allium **A**rsenide
HE	**H**igh **E**fficiency
IMU	**I**nertial **M**easurement **U**nit
NASA	**N**ational **A**eronautics and **S**pace **A**dministration
RC	**R**emote **C**ontrolled
RX	**R**eceiver
TX	**T**ransmitter
MPPTs	**M**aximum **P**ower **P**oint **T**racking
UAS	**U**nmanned **A**erial **S**ystem
UAV	**U**nmanned **A**erial **V**ehicle

Chapter 1

Introduction

1.1 Background

Fixed wing flight is mature and can be implemented by drawing on extensive knowledge and resources available (such as Anderson [2012]). Unfortunately, rigid fixed wing flight tends to suffer in low Reynolds regimes ($< 10^5$ Ho et al. [2003], Song et al. [2008]) and at high angles of attack ($> 25°$ using the data for airfoil lift coefficients provided by Anderson [2012] for context) Gerdes et al. [2013b], Pines and Bohorquez [2006], Zhao et al. [2009]. In contrast, flapping flight can be favorable in these areas, opening flight regimes and capabilities unparalleled by fixed weight platforms or traditional rotorcraft. Unsteady airflow mechanics, like leading vortex creation and shedding, operate favorably to produce forces at high angles of attack with flapping flight Jones and Babinsky [2010], Muijres et al. [2008], Shyy et al. [2013], Zhao et al. [2009]. Birds generate and control these effect to achieve high maneuverability and force generation by utilizing coordinated synchronous and asynchronous flapping gaits, body attitude, and modifying lift surface geometry in multiple degrees of freedom via control of their wings, tail

and body motions Jones and Babinsky [2010], Shyy et al. [1999, 2013], Thomas [1996, 1993], Tobalske [2007], Usherwood et al. [2003]. For example, birds are able to modify their wing geometries with variations in anhedral, dihedral, planform, camber, aspect ratio, and sweep Pines and Bohorquez [2006], Rayner [1988], Shyy et al. [1999, 2013], Thomas [1993], Tobalske [2007], Wu et al. [2010] in addition to wing warping. This is possible because avian morphology elegantly combines lightweight structure, exceptional control, energy density, and distribution of power-dense actuators Shyy et al. [2013], Tobalske [2007]. Similar feats of aerodynamic force control through actuation have been seen in mammalian flight Muijres et al. [2008]. Duplicating these feats in engineered systems proves to be difficult because direct force measurements on flying animals is difficult to perform and analyze Hubel and Tropea [2009], Song et al. [2008], Usherwood et al. [2003]; current aerodynamic models tend not to adequately predict behavior at low Reynolds numbers (¡10^5) Evans et al. [2002], Mancini et al. [2015a], Shyy et al. [1999], Viieru et al. [2006], and current actuator technologies impose limitations due to design challenges and system integration Gerdes et al. [2015].

1.2 Motivation for Research

Energy requirements for flying is higher than other forms of locomotion such as swimming, walking or running Schmidt-Nielsen [1972]. Furthermore, power is important for bird flight because work must be delivered at an adequate rate Tobalske [2007]. A high energy density system may not be able to provide that energy at a high enough rate to achieve effective flight, giving importance to power density. Actuator design and performance have been a limitation for flapping platforms, primarily because the actuators tend to be localized, heavy, and/or unable to meet the power demands for flight. While

many can provide adequate torque, they are unable to do so quickly enough to attain flapping frequencies that are aerodynamically effective for a given wing size. Hence, a major drawback of current engineered flapping winged flight is that payload is typically limited because flapping winged flight is challenging to achieve. Vehicles must be as light as possible to maintain flight let alone carry meaningful payload. With a limited payload, the battery that is used to power the vehicle is typically small which limits the energy available, resulting in reduced flight times and, consequently, overall mission capabilities. As a means of surpassing these limitations, strategies increase energy storage capacity via increased lift and energy density are important as well as harvesting techniques. Additionally, biological systems have rich capabilities yet unparalleled by robotic systems. Maneuverability is desirable for obstacle avoidance, grasping tasks, and transition behaviors for adjusting flight characteristics.

1.3 Goal and Scope

This work aims to increase the performance of a flapping wing aerial vehicles by increasing maneuverability and energy storage capacity via payload gains, increased mass economy and using otherwise parasitic mass in a multifunctional approach to increase maneuverability, integration of high energy density batteries, and development of an energy harvesting framework to consider energy independence. The specific goals are the following:

1. To validate that a mixed mode approach using propellers to generate thrust in conjunction with flapping flight is viable. Specifically, to determine that coupling in a mixed mode, propeller-assisted flapping wing vehicle is minimal and thus allows for usage of a mixed mode approach to provide improvements to flight payload

such that additional battery mass can be carried to improve system endurance despite increased power requirements.

2. To demonstrate inertial control via the usage of battery mass as a strategy to provide rapid deceleration to enhance maneuverability. Applications include collision avoidance, improving imaging of a target area by providing additional time over target, and perching capabilities.

3. To further approaches for integrating flexible media, specifically high efficiency photovoltaic solar cells and flexible batteries to the existing wing structure of the vehicle. Considerations of the load bearing nature of the wings for generation of both lift and thrust must be accounted for such that compliance, and thus performance, is not compromised. Successful integration of high efficiency solar cells can lead to self-charging and increased flight endurance in addition to gains provided by storage capacity provided by flexible batteries or capacitors, or even energy independence if adequate energy is provided.

4. The development framework for assessing energy gathering potential via the usage of solar cells to inform design of a flapping wing systems with multifunctional wings towards energy independence and autonomy

Chapter 2

Literature Review

2.1 Biological Flight Systems

As noted in the introduction, flapping flight displays flight regimes and capabilities unparalleled by fixed wing platforms or traditional rotor craft. Avian systems are impressive at generating and controlling unsteady airflow mechanics Jones and Babinsky [2010], Muijres et al. [2008], Shyy et al. [2013], Zhao et al. [2009]. Birds generate and control these effects to achieve high maneuverability and force generation by utilizing coordinated synchronous and asynchronous flapping gaits, body attitude, and modifying lift surface geometry in multiple degrees of freedom via control of their wings, tail and body motions Jones and Babinsky [2010], Shyy et al. [1999, 2013], Thomas [1996, 1993], Tobalske [2007], Usherwood et al. [2003]. Birds modify their wing geometries with variations in anhedral, dihedral, planform, camber, aspect ratio, and sweep in addition to wing warping (see Pines and Bohorquez [2006], Rayner [1988], Shyy et al. [1999, 2013], Thomas [1993], Tobalske [2007], Wu et al. [2010]). This is possible because avian morphology elegantly combines lightweight structure, exceptional control, energy density,

and distribution of power-dense actuators Shyy et al. [2013], Tobalske [2007]. There are also numerous examples of control of unsteady mechanics in mammalian flight Muijres et al. [2008], Swartz et al. [2012] and at smaller scales with insect flight Ellington [1984a,b,c], Tarascio et al. [2005].

2.2 Engineered Flapping Wing Systems

There are a number of commercially developed flapping systems in addition to a number of notable flapping platforms, warping wing and flapping wing characterization systems developed in the research community. These include, but are not limited, to Robird, Delfly, Festo's Smartbird, BatBot, and Harvard's Robo Bee Delfly [2016], Festo [2016], Hamamoto et al. [2010], Park et al. [2012], Ramezani et al. [2017], Solutions [2016], Teoh et al. [2012], Wu et al. [2010]. As a means of reducing system complexity and weight, many successful flapping wing platforms rely on a single actuator Doman et al. [2011], Shkarayev et al. [2010] to drive one degree of freedom while other degrees of freedom are generated using passive means to achieve complex kinematics Bejgerowski et al. [2010], Gerdes [2010], Gerdes et al. [2012], Madangopal et al. [2004], Platzer et al. [2008], Swartz et al. [2012], Teoh et al. [2012], Wu et al. [2010]. One such approach is the usage of flexible membranes which provides performance with passive deformation Mancini et al. [2015b], Platzer et al. [2008]. It must be noted that usage and benefits of flexible membranes are not limited to just flapping wing flight Ifju et al. [2002], Shyy et al. [2005]. Among the engineered flapping wing vehicles is *Robo Raven* which was developed at the University of Maryland Gerdes et al. [2014]. The hallmark of Robo Raven is the ability to program the servos to independently control the wings with both high torque and high speed. There have been different versions of Robo Raven for

various research pursuits: platform wing sizing and motor performance (II) Gerdes et al. [2013b, 2015], harvesting solar energy with low efficiency solar cells (III) Perez-Rosado et al. [2014, 2015a,b], and autonomous flight control (IV) Roberts et al. [2014, 2015, 2016].

2.3 Multifunctional Approaches in Unmanned Systems

The multifunctional approach, making materials and structures perform multiple tasks, is useful because it reduces parasitic mass and can provide added functionality. There are a number of examples of the usage of energy harvesting and storage in fixed wing aircraft systems in the research community Anton and Inman [2008], Thomas et al. [2002], Thomas and Qidwai [2005]. These are examples of energy harvesting of vibrational energy, solar energy harvesting and integration of battery systems into the wing designs of unmanned systems. A framework for inclusion of solar cells were described by Zhang and Hu [2016] for flapping with aerial vehicles. Success in the Robo Raven III platforms Perez-Rosado et al. [2014, 2015a,b] has shown the benefits of solar integration even with low efficiency solar cell integration.

2.4 Hybrid Systems

There are a number of hybrid systems such as Boeing's V-22 Osprey tilt roto craft Boeing [2016] and do-it-yourself kits such as a tilt rotor quadrotor combined with an airfoil to provide vertical takeoff and forward flight efficiency AimDroix [2016]. A walking and flying, bat-inspired, morphing vehicle was developed by Daler et al. [2013], where propeller driven propulsion was paired with bio-inspired terrestrial locomotion. Hybrid

systems leverage advantages to provide capabilities which are difficult to achieve using a single parent technology. The advantages of the hybrid approach, despite the performance trade-offs and difficulties achieving a functional design are typically worth while to achieve specific mission goals.

2.5 Inertial Control

There are numerous examples of biological systems leveraging their body mass and inertial to control their movement. For example: Lizard species right themselves and control aerial motion using the mass and inertia of their tails Chang-Siu et al. [2013], Libby et al. [2012]; Cheetah that use their tails to provide turning stability and break when running Briggs et al. [2012], Patel and Braae [2014], and people leverage their arm mass while jumping Hayashi and Tsujio [2001]. Birds demonstrate abilities such as perching, rapid turning, and grasping tasks Doyle [2011], Thomas et al. [2014], leveraging adaptive morphology to manipulate mass Mintchev and Floreano [2016] and airflow mechanisms. Given the growing interest in increasing capabilities of unmanned aircraft systems (UAS) and unmanned aerial vehicles (UAV), achieving similar feats to natural flyers with man made aerial systems is compelling. For example, maneuverability is useful for obstacle avoidance in cluttered environments. Additionally, perch and stare capabilities are appealing as they allow for imaging and station keeping with low energy cost or may even allow for recharging if used in conjunction with photovoltaics Doyle [2011].

The richness of the feature set demonstrated by natural systems has prompted a number of robotic platforms as a result of bio-inspiration. A cheetah inspired robot capable of running and jumping over obstacles that controls reaction forces with the ground has

been developed Wensing et al. [2017]. Usage of an inertial tail was proposed to provide stability to that robot Briggs et al. [2012]. In work by Rone et al. [2018] continuous deformations of biological tails were mimicked using a serpentine robotic capable of exerting forces on its base. Future applications of this tail include integration with a bipedal robot to provide control. In addition to biological strategies, there are other means of generating forces and moments including reaction wheels, reaction masses, and propellers which are of note, given their usage on robotics platforms Briggs et al. [2012], Rone et al. [2018]

A spinning mass was used for inertial control of a small legged terrestrial robot in Casarez et al. [2013]. A limited tail was used to improve turning of a terrestrial legged robot in Kohut et al. [2013a]. In related work to Kohut et al. [2013a], aerodynamic steering of a terrestrial robot was considered. It was found that the sail could be dynamically actuated to cause a rapid change in body orientation through inertial effects alone Kohut et al. [2013b]. In Iida et al. [2002] swinging pendulums were used to induce bipedal hopping gaits and human inspired jumping using winging pendulum arms has been studied Hayashi and Tsujio [2001]. A rolling robot with the ability to jump to clear obstacles uses a 1 DOF tail to control position during the jump Zhao et al. [2013, 2015]. Following that work, and inspired by lizards, an active tail was used to self right on a wheeled terrestrial robot Chang-Siu et al. [2011], Li et al. [2015]. Also following the biological example of lizards, control of a tail was used for self righting of a 2 DOF robot Chang-Siu et al. [2013]. A strictly jumping robot, which uses a series elastic actuator in conjunction with a variable mechanical advantage to store energy and jump, used an inertial tail to stabilize while in air Haldane et al. [2016]. Later, thrusters were used to stabilize midair in addition to inertial tail Haldane et al. [2017]. Battery mass was used to augment control of a quadrotor in Bouabdallah et al. [2006]. Specifically, the

battery was actuated in order to move the center of mass relative to the thrust vectors produced by the propellers. The mass and inertia of the manipulator mounted to a quadrotor was utilized in order to stabilize quadrotor as a secondary task when not gripping Santamaria-Navarro et al. [2014], making the gripper serve multiple functions. In a flapping wing case, an inertial tail was used to provide control on a nano air vehicle Penskiy et al. [2012].

2.6 Adaptive Morphology

Supported with biological evidence, adaptive morphological changes can extend dynamic performances by reducing trade-offs during locomotion an provide new functionality Mintchev and Floreano [2016]. Bio-inspired adaptive designs were considered for a robot capable of jumping and gliding to cover larger terrain Kovač et al. [2011]. Feather style wings were shown in a propeller powered aerial vehicle which was capable of retracting a wing in order to roll Di Luca et al. [2017]. A morphological change can alter the position of center of mass or provide a dynamic change of inertia, which adds an interesting level of design depth considering the interial control work noted previously. As a means of achieving perching, a morphing aircraft was developed to maintain elevator control as a means of providing practical perching maneuvers for low thrust-to-weight aircraft Wickenheiser and Garcia [2006, 2008].

2.7 Avian Tasks and Strategies

Using conventional designs, control and perching of a fixed wing aircraft has been studied in a controls realm Cory and Tedrake [2008], Glassman et al. [2012], Hoburg and Tedrake

[2009], Roberts et al. [2009] with an application of landing on power lines Moore and Tedrake [2009]. It was noted in Roberts et al. [2009] that the thrust can be valuable in rejecting disturbances compared to glider performance, although at the cost of increased system complexity. A dihedral based control for gliding flight was demonstrated by Paranjape et al. [2013] using a fixed wing platform with articulated wingtips past the quarter span as a test case (though it would primarily be meant to be used in flapping wing aircraft where the wings are inherently articulated). In work by Crowther [2000] which also considered fixed wing perching, it was noted that many birds flap when approaching a perch. It was postulated that flapping is used to generate additional aerodynamic braking while at low speed in the final steps of the landing sequence to decelerate.

Holding on to a perch and grasping have been explored using conventional platforms. Perching using optic flow and range finders on a model helicopter for landing Danko et al. [2005] and grasping using vision and optical flow was investigated using a quadrotor based system Thomas et al. [2014]. Notably, the position of the grasping device was changed in flight in Thomas et al. [2014] to lower the relative velocity between gripper and object in a bio-inspired approach. A bio-inspired (avian) passive grasping mechanism for perching was developed for usage with a quadrotor Doyle [2011], Doyle et al. [2013]. In that work, the paradigm of recharging the robots power source through the use of photovoltaics was highlighted as a key feature that a perching capability could allow Doyle [2011].

Chapter 3

Robo Raven Design and Manufacturing

Robo Raven is a flapping wing aerial vehicle developed by the University of Maryland, College Park Gerdes et al. [2014]. Biologically inspired, it has a wingspan similar to a Common Raven, *Corvus Corax*. Each wing is a flexible membrane that is reinforced with carbon fiber rods which are separately driven by software programmable Futaba S9352HV servo motor (or the more recent S9372HV sBus motor) and the tail is operated as a rudder inclined such that it provides a static elevator functionality. Design of the wings is shown in 3.1, where the values of the parameters are given in Table 3.1.

The original Robo Raven I had a 3D printed frame for the servo box. A frame composed of laser cut Delrin plastic parts has largely replaced this 3D printed version. Consistent with the initial design, the remainder of the parts were laser cut. The addition of a 2 DOF tail has been added in subsequent versions which have the payload capacity for an additional actuator for active elevator control. Additionally, the tail geometry has been modified, and informed by findings of Thomas [1993].

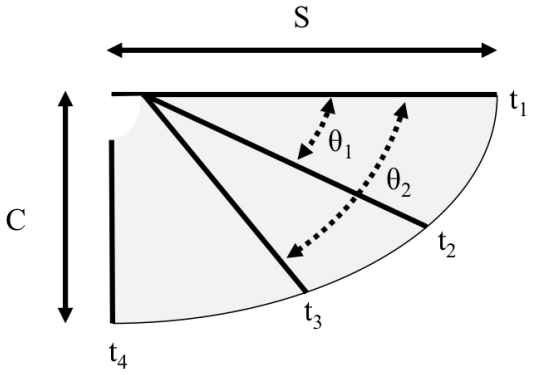

FIGURE 3.1: Robo Raven standard wing design

TABLE 3.1: Robo Raven I wing design parameter values

Component	Value	Unit
S	605.8	mm
C	362.0	mm
t_1	3.18	mm
t_2	1.63	mm
t_3	1.63	mm
t_4	1.63	mm
θ_1	0.358	rad
θ_2	0.750	rad

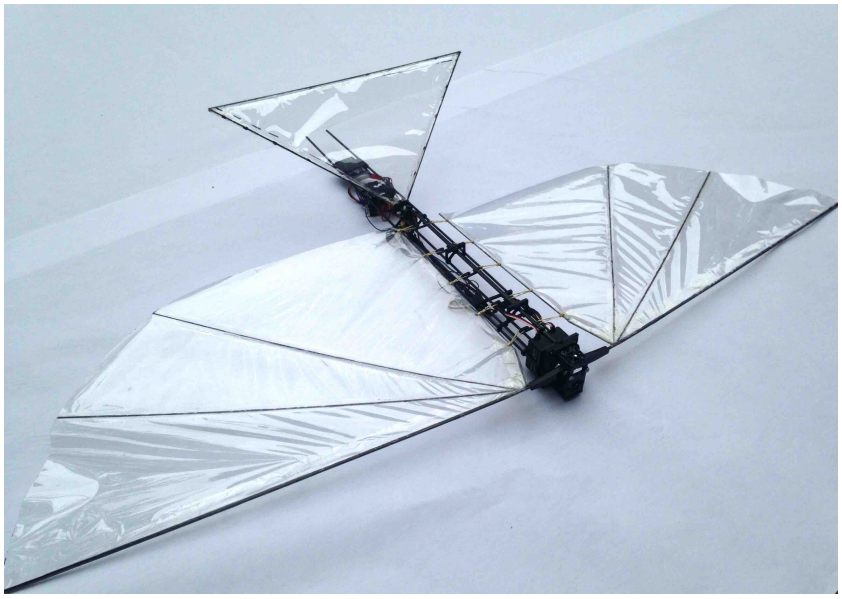

FIGURE 3.2: Robo Raven 1 flapping wing aerial vehicle

Chapter 4

Propeller Assisted Flight to Improve Endurance via Payload Increase

4.1 Introduction

Fixed wing flight is mature and can be straightforward to implement with the extensive knowledge available Anderson [2012]. Unfortunately, rigid fixed wing flight tends to suffer in low Reynolds regimes ($<10^5$ Ho et al. [2003], Song et al. [2008]) and at high angles of attack ($>25°$ using the data for airfoil lift coefficients provided by Anderson [2012] for context) Gerdes et al. [2013b], Pines and Bohorquez [2006], Zhao et al. [2009]. In contrast, flapping flight can be favorable in these areas De Croon et al. [2009]. Unsteady airflow mechanics, like leading edge vortex (LEV) creation and shedding, operate favorably to produce forces at high angles of attack with flapping flight Jones and Babinsky [2010], Muijres et al. [2008], Shyy et al. [2013], Zhao et al. [2009]. Birds

generate and control these effects to achieve high maneuverability and force generation which shine in displays of transient flight manipulation tasks like mid-air grasping and perching. These are feats which are not easily completed by conventional fixed wing systems though there are successful examples with rotorcraft Jiang and Voyles [2013], Thomas et al. [2013]. This is achieved via coordinated, synchronous and asynchronous flapping gaits, body attitude, and modification of lift surface geometry in multiple degrees of freedom via control of their wings, tail and body motions Jones and Babinsky [2010], Shyy et al. [1999, 2013], Thomas [1996, 1993], Tobalske [2007], Usherwood et al. [2003]. For example, birds are able to modify their wing geometries with variations in anhedral, dihedral, planform, camber, aspect ratio, and sweep Pines and Bohorquez [2006], Rayner [1988], Shyy et al. [1999, 2013], Thomas [1993], Tobalske [2007], Wu et al. [2010] in addition to wing warping. This is possible because avian morphology elegantly combines lightweight structure, exceptional control, energy density, and distribution of power-dense actuators Shyy et al. [2013], Tobalske [2007]. Similar feats of aerodynamic force control through actuation can been seen in mammalian flight Muijres et al. [2008]. Duplicating these feats in engineered systems proves to be difficult because direct force measurements on flying animals is difficult to perform and analyze Hubel and Tropea [2009], Song et al. [2008], Usherwood et al. [2003]. Current aerodynamic models do not yet provide accurate predictions of behavior at low Reynolds numbers ($<10^5$) Evans et al. [2002], Mancini et al. [2015a], Shyy et al. [1999], Viieru et al. [2006]. Current actuator technologies impose limitations due to design challenges and system integration Gerdes et al. [2015].

The energy requirements for bird-inspired flapping wing flight are higher than for other forms of locomotion such as swimming, walking or running Schmidt-Nielsen [1972]. Furthermore, power is important for bird-inspired flight because work must be delivered at

a rate that generates enough lift and thrust force simultaneously during the flapping motion Tobalske [2007]. For example, a high energy density power source may not be able to provide energy at a fast enough rate to achieve flight, resulting in an inadequately low-power density. Actuator design and performance have also been a limitation for flapping platforms, primarily because the actuator options for driving the wing through the flapping motion must provide mechanical work while also being light. Actuation options tend to be localized and heavy, if they are designed to meet the mechanical power demands for flight. On the other hand, if they are designed to meet the weight requirements, then they may be unable to meet the mechanical power requirements. While many actuation options can provide adequate torque, they are unable to do so quickly enough (i.e., they are underpowered) to attain the flapping frequencies that are necessary for a given wing size to generate the lift and thrust forces necessary to achieve flight. Conventional actuators that meet the power requirements are often heavy, which restricts number and placement of actuators used to generate a desired wing motion. This often precludes the ability to mimic the biological kinematics of bird wings, which require flapping motion and gaits consisting of multiple degrees of freedom Park et al. [2012], Tarascio et al. [2005]. As a means of reducing system complexity and weight, many successful flapping wing platforms have relied on a single actuator De Clercq et al. [2009], De Croon et al. [2009], Doman et al. [2011], Gerdes et al. [2012], Shkarayev et al. [2010] to drive one degree of freedom while other degrees of freedom are generated passivelyBejgerowski et al. [2010], Gerdes [2010], Gerdes et al. [2012], Madangopal et al. [2004], Platzer et al. [2008], Swartz et al. [2012], Teoh et al. [2012], Wu et al. [2010]. One such approach is the usage of flexible membranes which provides performance with passive deformation (with benefits not limited to flapping flight only) Ifju et al. [2002], Mancini et al. [2015b], Platzer et al. [2008], Shyy et al. [2005]. Additionally, it was noted

that usage of a single actuator to drive both wings saves weight, but limits the flapping gait. This is because only fixed amplitudes can be achieved and wing gait characteristics are tied to a single source Bejgerowsk et al. [2009], unless a complex mechanism is designed to overcome it Park et al. [2012].

With recent developments in servo motor technology, independent control of passively deforming wings has been achieved in a flapping wing air vehicle (FWAV) known as *Robo Raven* Gerdes et al. [2014]. Robo Raven I, the original design, is shown in Fig. 4.1(a). The hallmark of Robo Raven is the ability to program the servos to independently control the wings with both high torque and high speed. There have been different versions of Robo Raven for various research pursuits: platform wing sizing and motor performance (II) Gerdes et al. [2013b, 2015], harvesting solar energy (III) Perez-Rosado et al. [2014, 2015a,b], and autonomous flight control (IV) Roberts et al. [2014, 2015, 2016]. (An additional version exploring integrated flexible energy storage (VI) is also in development Holness et al. [2016] which post- dates the introduction of the concept for this work Holness et al. [2015], which is designated Robo Raven (V)). In these versions, continuous flapping, outside of brief periods of time, is required to sustain flight because of platform weight. Thus, increasing platform aerodynamic performance would widen capabilities, as well as potentially increase payload capacity. For example, higher aerodynamic performance would allow usage of different flapping profiles for greater maneuverability (such as changing flight path vector and vehicle orientation) which is useful for enhancing stability during adverse flight conditions, such as strong winds. By increasing payload, more sensors can be added for more complex autonomous control, or more power sources can be added to increase flight time.

Due to the present limitations of the wing design and actuators used on FWAVs like Robo Raven, it has been desirable to find alternative approaches to increasing payload

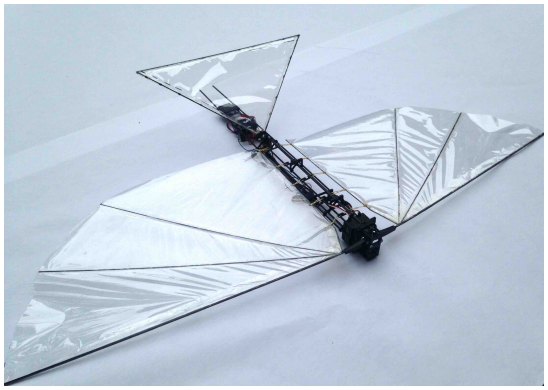

(a) Robo Raven I flapping wing aerial vehicle

(b) Robo Raven V: propeller assisted flapping wing aerial vehicle

FIGURE 4.1: Robo Raven 1 and Robo Raven V platforms

capacity and maneuverability. Thus, the goal of this paper is to explore the viability of adding a propeller propulsion mode to FWAVs, and characterizing how this mode interacts with the flapping mode for thrust and lift generation. Flapping wings and traditional propulsion used with fixed wing aircraft need not be mutually exclusive. Given the thrust provided per unit mass when using propellers (even at scale), it was postulated that a propeller-assisted flight mode might generate more thrust and, in turn, aerodynamic lift, such that the added mass of the actuators and power sources would be offset and the payload capacity would be substantially increased. Furthermore, interactions between the flapping wing and propeller-assisted flight, particularly the placement of the propellers relative to the flapping wings, need to be understood to determine if there are effects that adversely limit the aerodynamic forces that are generated. Therefore, the forces generated by each mode were investigated independently, as well as while operating together. This enabled each mode to be modeled and compared to the mixed mode case to determine interactions between the two flight modes. Viability of using mixed mode propulsion for FWAVs was shown via flight testing of a new platform called *Robo Raven V*.

4.2 System Model of Aerodynamic Force Generation by FWAVs

During flapping flight, aerodynamic thrust and lift forces undergo periodic variations. A common modeling approach is to use a quasi-steady state assumption Madangopal et al. [2004], Shyy et al. [2013]. Quasi steady-state wing theory assumes that the forces on a moving wing are equivalent to the sum of the forces on a fixed wing, over a sequence of attitudes that track the wing motion. This model neglects acceleration forces and unsteady aerodynamic effects" Muijres et al. [2008]. In very small intervals of time, the flight is considered level with no acceleration. This implies that the forces in all directions must be equal during steady state flight, assuming no change in mass. Therefore, in the horizontal direction, thrust must be equal to the drag during steady state flight Anderson [2012].

$$F_T = F_D \tag{4.1}$$

where drag is defined by Anderson [2012]:

$$F_D = \frac{1}{2}\rho V^2 S C_{D,p} \tag{4.2}$$

where V is the freestream velocity, S is the planform area of the wing, and $C_{D,p}$ is the drag coefficient of the wing. Substituting Eq. 4.2 into Eq. 4.1 yields:

$$F_T = \frac{1}{2}\rho V^2 S C_{D,p} \tag{4.3}$$

Because the average thrust is generated using the flapping wings

$$F_T = F_{FT} \tag{4.4}$$

The flapping wing model for the thrust is the following:

$$F_{FT} = k_F f^2 S \Delta\alpha \tag{4.5}$$

where f is the flapping frequency in Hz and $\Delta\alpha$ is the flapping amplitude in radians. This is produced with insight gained from Platzer et al. [2008] which notes that thrust increases with frequency and amplitude of oscillation, work by Shyy et al. [1999, 2013], and a flapping advance ratio as follows Ho et al. [2003]:

$$J = \frac{V}{2\Delta\alpha f b} \tag{4.6}$$

where b is the wingspan.

This model of flapping flight does account for aeroelastic effects. As such, a different model will be proposed for larger wings and cases where performance reductions due to actuator deficiencies couple with wing deformations. Substituting Eq. 4.5 as the thrust term in Eq. 4.3 yields:

$$k_F f^2 S \Delta\alpha = \frac{1}{2}\rho V^2 S C_{D,p} \tag{4.7}$$

For steady flight with no acceleration in the vertical direction, forces must also sum to zero. Assuming no loss of mass or body forces aside form gravity, for steady state flight conditions, average lift forces must offset the weight (mg) Anderson [2012].

$$F_L = mg \tag{4.8}$$

The aerodynamic lift is given by Anderson [2012] as:

$$F_L = \frac{1}{2}\rho S V^2 C_L \tag{4.9}$$

where C_L is the lift coefficient of the wing. Substituting Eq. 4.9 into Eq. 4.8 yields:

$$\frac{1}{2}\rho S V^2 C_L = mg \tag{4.10}$$

It is possible to relate thrust to lift using the velocity. Rearranging Eq. 4.3 and solving for V^2 yields:

$$V^2 = \frac{2F_T}{\rho S C_{D,p}} \tag{4.11}$$

Substituting Eq. 4.11 into Eq. 4.9

$$F_L = \frac{C_L}{C_{D,p}} F_T \tag{4.12}$$

Substituting the thrust generated by flapping (Eq.4.5):

$$F_L = \frac{C_L}{C_{D,p}} k_F f^2 S \Delta\alpha \tag{4.13}$$

Substituting this lift into equation 4.10 yields the maximum flight weight:

$$\frac{C_L}{C_{D,p}} k_F f^2 S \Delta\alpha = mg \tag{4.14}$$

Based on this model it can be seen that thrust governs the offsetting drag force value and subsequently dictates the forward velocity by the relationship given in Eq. 4.3 (if

all else remains constant). An increase in velocity, V, benefits lift generation by way of aerodynamic lift as seen in Eq. 4.9. Given this, thrust and lift can be related as seen in Eq. 4.12. These relationships provide insight into ways to increase performance by increasing thrust.

4.3 Strategies for Increasing Performance

An increase in thrust can be caused by either changing the flapping mechanics or adding another source of thrust production. A discussion of the former will shed light on the choice of the latter strategy employed in this work. Ideally, there are a few means of increasing flapping thrust production by changing the wing design, increasing the wing area S, attaining a higher flapping amplitude, and increasing the flapping frequency based on Eq. 4.5. The difficulty of changing wing design and size is the complex aeroelastic behavior which modifies k_F. Global stiffness and localized stiffness changes the performance of wings Ho et al. [2003], Perez-Rosado et al. [2015c] as well as inertia Percin et al. [2014]. Modeling changes of the mechanical deformation of the wing and tracing aerodynamic performance from it with an explicit model is still a point of research. Iterative design, via trial and error, and evaluation often is required to determine wing performance at specific operating conditions De Clercq et al. [2009]. A lower value k_F at a desired operating point yields lower force production and costs a design iteration. An example of this is a wing design that flutters, where the forcing frequency produces vibrations of the membrane instead of achieving deformations that generate useful aerodynamic forces.

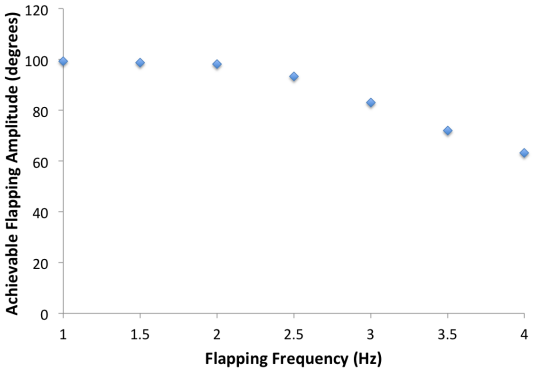

FIGURE 4.2: Loss of achievable flapping angle amplitude as flapping frequency increases due to torque limitations of servo motors

Given difficulties describing aeroelatic effects, it is desirable to maintain a proven, functional wing design. If the wing design is to be unchanged, modifying the flapping amplitude and frequency can be considered based on the model, however, actuator deficiencies prevail which limit both the flapping amplitude and frequencies.

4.3.1 Flapping Frequency Dependence on Actuator Performance

Given the dependence on flapping frequency, it should be possible to increase thrust by increasing flapping frequency and range. Work by Gerdes exploring motor performance, deformable wing sizing, and flapping frequencies shows that actuator limitations restrict the effects of increasing flapping frequency for thrust production Gerdes et al. [2015]. As flapping angle increases, thrust and lift also increase as shown in Eq. 4.3. At low flapping frequencies, the servos driving the wings are able to maintain the flapping angle and develop the required wing deformation to move air. At higher frequencies, the achievable angle tends to decrease as seen in Fig. 4.2 because the servos are constantly trying to follow the commanded flapping signal. Given that there is a reduction in the flapping angle and subsequent wing deformation at high speeds, the rate of thrust and lift production falls below the quadratic increase with flapping frequency predicted by

Eq. 4.5 for constant flapping amplitude. The decrease in additional thrust production is evident in Fig. 4.3 as tapering off of the thrust above 2.5 Hz. Using the amplitude results from Fig. 4.2 in Eq. 4.5, it can be seen that the model follows the loss of additional thrust production at higher flapping frequencies in Fig. 4.3. The model assumes that the value of k_F is constant, based on experimental data at a known amplitude and frequency. Thus, it does not account for any aeroelastic effects of the wing itself, apart from changes in flapping amplitude. The departure of the measured data from the model at 4 Hz seen in Fig. 4.3 is an indication that there may be additional dependencies of the model parameters on aeroeslatic behavior, beyond flapping amplitude. The results shown in Fig. 4.2 and Fig. 4.3 were obtained using the same force transducer; brand and model of encoder; and measurement setup that will be explained in the methodology section. For further elaboration refer to Gerdes et al. [2015].

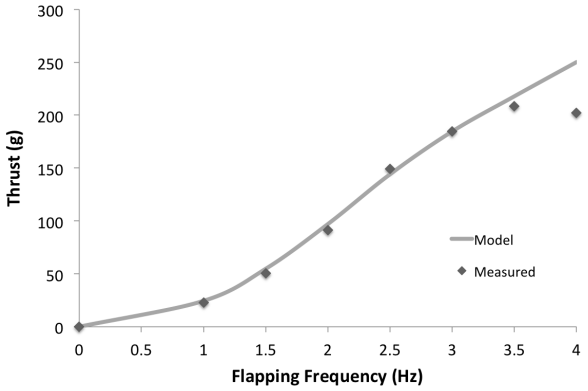

FIGURE 4.3: Average measured and modeled thrust vs flapping frequency showing tapering of thrust production due to loss of flapping amplitude at frequencies above 2.5 Hz

A means of attempting to surpass the angle limitation as flapping frequency increases would be the use of higher torque and higher speed motors which are often heavier. In the case of Robo Raven particularly, this change would result in larger servos that localize more mass at the front of the vehicle. This would make it difficult to achieve an angle of attack as well as the necessary lift to achieve flight. Details regarding system

design issues, such as the actuator and wing coupling, have been investigated in other work Gerdes et al. [2017]. Therefore, new approaches are needed to augment thrust production in FWAVs.

4.3.2 Enhancing Thrust Production in FWAVs Using Propellers

As an alternate means to changing the main servo motors for the flapping wings to augment thrust production in FWAVs, propeller assistance was investigated in Robo Raven V. The addition of propeller-motor assemblies will change the steady state thrust in Eq. 4.4 to the sum of the two modes minus a loss term for anticipated coupling, Ψ (because of preliminary findings Holness et al. [2015]):

$$F_T = F_{FT} + F_{PT} - \Psi \tag{4.15}$$

Where the thrust of the propellers can be modeled by the following expression Anderson [2012], Brandt and Selig [2011], Brezina and Thomas [2013], Deters and Selig [2008], Silvestre et al. [2014]:

$$F_{PT} = C_T \rho \Omega^2 D^4 \tag{4.16}$$

Substituting the flapping model (Eq. 4.5) and the propeller model (Eq. 4.16) into Eq. 4.15 yields:

$$F_T = k_F f^2 S \Delta\alpha + C_T \rho \Omega^2 D^4 - \Psi \tag{4.17}$$

Substituting Eq. 4.17 for the thrust term in Eq. 4.3 yields:

$$k_F f^2 S \Delta\alpha + C_T \rho \Omega^2 D^4 - \Psi = \frac{1}{2} \rho V^2 S C_{D,p} \tag{4.18}$$

Substituting the combined thrust, the lift is given by:

$$F_L = \frac{C_L}{C_{D,p}}(k_F f^2 S\Delta\alpha + C_T\rho\Omega^2 D^4 - \Psi) \tag{4.19}$$

Substituting this lift into equation 4.10 yields:

$$\frac{C_L}{C_{D,p}}(k_F f^2 S\Delta\alpha + C_T\rho\Omega^2 D^4 - \Psi) = mg \tag{4.20}$$

A benefit of adding thrust via a non-flapping mode, if completely decoupled from the flapping, is that the flight velocity can be increased aiding the aerodynamic lift term without altering the flapping mechanics. Based on Eq. 4.20, the implications suggest an increase in payload by the net increase of the lift or a trade-off scenario where an increase in the aerodynamic lift would decrease the demand for continuous flapping, allowing greater utilization of independent wing control to rapidly change the flight path vector and vehicle orientation.

4.4 Overview of Robo Raven V

Robo Raven V (shown in Fig 4.1(b)) modifies Robo Raven I by adding propellers behind the flapping wings, actuators to control the position of the propellers, and electrical connections to support the additional power and control for the propeller assemblies.

4.4.1 Propeller Location

There were numerous configurations for the propeller placement. The propellers could be placed in front or behind the wings and placed above, equal with, or below the body

centerline. Combinations of these configurations are shown in Fig. 4.4. Placing the propellers in the front is difficult because it makes the Robo Raven Platform, which is already nose heavy, even more-so which moves the center of gravity forward, causing a nose dive. In the original Robo Raven I, the battery and micro controller are placed at the rear of the platform (behind the tail assembly) to bring the center of mass behind the center of lift of the wings so the platform pitches upward. This is achieved by making the fuselage longer then necessary to mount the wings and tail assembly. This provides a large moment arm and serves to bring the center of mass behind the center of lift of the wings so that the platform pitches upward. Placing the propellers at the front of the platform magnifies this problem and cannot be easily corrected by adjusting the battery despite the larger battery mass to accommodate the electrical needs (which will be discussed later) and micro controller position. Furthermore, front mounted propellers are difficult because of the complexity of designing a mechanism that would securely attach the propeller assemblies, while leaving the flapping mechanism unaffected and allowing electrical access to each motor. More importantly, it is unclear how a localized change in air velocity before the wings would affect both the wind deformation and the airflow phenomena, particularly the formation of LEVs which are of key interest in flapping flight De Clercq et al. [2009], Jones and Babinsky [2010], Muijres et al. [2008]. In contrast, placing the propellers at the rear of the FWAV moves the center of gravity backward. With this configuration, it is possible to move the battery and micro controller to adjust the center of gravity in an appreciable way while allowing electrical access from the center of the platform clear of moving parts. As noted previously, the propellers could be placed above, equal with, or below the body centerline. Placing the propellers above the center line pitches the nose downward because of the net moment generated by the thrust of the propellers at a distance away from the centerline. With

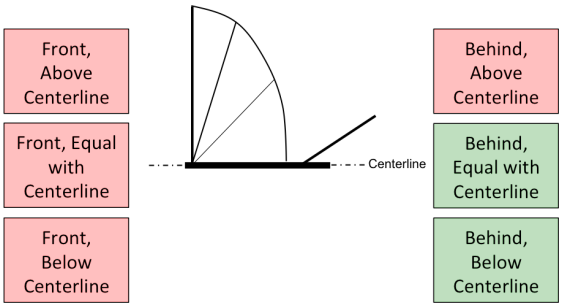

FIGURE 4.4: Considered propeller configurations

the propellers level with the centerline creates no net moment. The fear was that this is directly behind the flapping wings which might increase coupling. Finally, placing the propellers below the centerline can be favorable because of the net moment that is generated by the thrust of the propellers counteracts the downward pitching moment from the forward mounted flapping motors. Additionally, the propellers are not directly behind the mid stroke of the wings. Ultimately, the position of the propellers was chosen to be behind the wings and equal or below the centerline. An assembly was made such that the propeller position was adjustable to explore propeller placement and coupling effects. The length of the propeller mounting assembly was dictated by the propeller diameter. They were made just long enough to mount the propeller in order to reduce mass and the bending moment created by the force the propellers at the end of the mounting arm. The distance between the back of the wing and the propeller was kept small to reduce the form factor.

4.4.2 Hardware Overview

As with Robo Raven I, each wing is separately driven by a Futaba S9352HV servo motor. The technical specifications for these Futbab motors are given in Table. 4.1. The tail is operated as a rudder inclined such that it provides a static elevator functionality. In the initial presentation of Robo Raven V Holness et al. [2015], the tail also had elevator

functionality. While it can be accommodated in the platform payload and used as an altitude control, it was removed for characterization simplicity and to increase payload capacity. Two DYS BE1806 brushless motors are used to drive 12.7 cm diameter Gemfan 5030 propellers mounted at the rear of the platform. These motors weighed 9.7 g each as their leads shortened and different screws were utilized. They are rated at 2300 RPM/V. The counter the torque generated my the rotating propellers, following convention, the left motor is rotated clockwise and the right is rotated counter clock wise such that the tops of the propellers rotate towards each other. For the exploration of position in this work, adjustable arm mounts were created to vary the propeller locations. This would allow measurements at various distances below the centerline without having to modify the platform. The mounting scheme is on a pivot as seen in Figs. 4.5(b) and 4.5(c) which modifies the horizontal spacing slightly. The extreme downward position is shown in Fig. 4.5(c). The result is that the horizontal position changes when the vertical position is adjusted. Given the cosine relationship, the horizontal position would be changed 30 % at 45 degrees. Consistent with Robo Raven I, the primary microcontroller for initial development was an Arduino Nano. Recently, an implementation has been created using ArduPilot 2.6 Roberts et al. [2015] because it has onboard sensors and is easier to interface with GPS. The remote control inputs are provided by a Spektrum six channel RX/TX pair. The system is powered by a 2 cell lithium polymer battery, with a nominal voltage of 7.4 V, 8.4 V when fully charged. Details about the battery capacity are noted later.

TABLE 4.1: Servo specifications

Voltage	Torque
6.6 V	19.6 kg cm (272 oz-in)
7.4 V	22.0 kg cm (305 oz-in)

Voltage	Speed
6.6 V	0.07 sec/60 deg
7.4 V	0.06 sec/60 deg

4.5 Testing Methodology

In order to assess mixed mode performance, two Robo Raven V platforms were created. The first platform was a flight testing platform used to verify flight feasibility and payload. Flights were calm days in a shielded flight space to ensure similar fly paths and headings. The platform was hand launched and allowed to reach steady flight (rudder control was only utilized during the launch period). The second platform was statically mounted to a test stand equipped with an American Digital optical encoder (# E5-500-118-IE-S-H-D-3) to record the wing flapping amplitude and ATI Mini40 six-axis force/torque transducer. Thrust measurements were recorded in 5 m/s (as measured by a pitot tube) of airflow generated by fan in a wind tunnel Gerdes et al. [2014]. The force transducer is capable of independently measuring all six components of force and torque using a Cartesian coordinate system and was calibrated by ATI to measure up to 40 N in the X and Y directions with a resolution of 1/100 N (1.02 g) of resolution and 120 N in the Z direction with a resolution of 1/50 N (2.04 g). The resonant frequency for Fx, Fy, and Fz measurements are 3200 Hz, which is far beyond the operating frequency. This test stand design was developed and utilized in previous flapping flight work Mueller et al. [2010] and has characterized Robo Raven in previous work Gerdes et al. [2014], Perez-Rosado et al. [2014, 2015a,b]. Similar approaches with load cells have

been used in other flapping research work Rose and Fearing [2014]. A modification was made to accommodate Robo Raven V, given that all previous iterations of Robo Raven did not have propellers. This setup can be seen in Figs. 4.5.This test stand allows for flapping at various frequencies, propeller positioning, and propeller speeds. In this work propellers were operated at various motor input signals from 20 % to 100 % in increments of 20 % while in 5 m/s airflow similar to Gerdes et al. [2013b]. The corresponding angular speed, Ω, in revolutions per minute was related to the motor input signals using a Extech 461920 tachometer. Three trials were conducted for each force measurement including the baseline modes (flapping only and propellers only) and for each measured mixed mode condition. The data was recorded using a LabView VI interfaced with a National Instruments data acquisition system after the static platform was mounted on the load cell. During operation, the data was gathered for 5 seconds at 1,000 samples per second. The flapping, propellers or both were started and stopped before and after each capture window, respectively, to ensure well developed operation free of initial and final transients. These 5,000 samples were then averaged to provide the net thrust. The test was then repeated two more times. The average of three trials was then averaged to produce the final figure for the thrust provided. To prevent issues with motor heating which could skew the results, time was allowed between tests, particularly for the wing servos.

4.5.1 Investigation of Coupling And Vertical Position Sensitivity

To determine coupling and sensitivity to the vertical placement of the propeller assemblies, thrust measurements were taken using the load cell described above.

4.5.1.1 Coupling Determination

In order to determine if there is coupling between the propulsion modes, baselines values for each mode were measured (i.e., only while flapping and only while the propellers were being driven). Assuming no coupling occurs (detrimental or beneficial) the expected performance would be the superposition (i.e., the sum) of the baseline measurements. Given the likelihood of negatively coupling, a loss term, Ψ, was added to Eq. 4.15. To assess this, the computed sum was compared against a combined measurement of thrust for both modes used together in the mixed mode case. A significant departure would indicate high degree of coupling between the flapping wings and the propellers.

4.5.1.2 Vertical Position Sensitivity

In order to determine if there was sensitivity to the vertical position of the propeller assemblies, tests were also conducted while flapping with the propellers located at various positions below the centerline. Specifically, at the maximum distance allowable, 53 mm (Fig. 4.5(c)), and at incremented multiples of 10 mm below that (i.e., 50 mm, 40 mm, 30 mm, 20 mm, 10 mm, and 0 mm) where 0 mm is aligned with the body Fig. 4.5(b)).

4.5.2 Flight Performance and Model Evaluation

To verify flight feasibility using mixed mode propulsion, flight tests were conducted. While load cell measurements provide insights into aerodynamic force production they fail to be fully representative of in flight performance because the platform is fixed. Furthermore, given that this particular design is unprecedented, models do not exist to predict flight performance. For this reason flight testing was critical to determine basic flight feasibility, payload, climb rate, and other capabilities provided dual modality

(various combinations of flapping frequency, fixed wing positions and propeller usage). Flight tests where experimental data was collected were conducted on days with wind speeds below 1 knot (0.5 m/s). Given the substantial increase in thrust and lift achieved with Robo Raven V, flight tests were conducted outside, unlike Robo Raven I which can be tested in an indoor facility.

To determine the maximum takeoff mass and payload capacity, mass was added to the craft until it was no longer able to climb and maintained a level flight path, meaning that the lift is offset by weight. To verify, additional mass was added to ensure it was exceeded, demonstrated by steady descent after launch. Given the dependence on mass location, mass was distributed accordingly. This value was then compared to the model in order to evaluate the usefulness of the model. A single point (representing an average of 3 trials) of the measured data from the individual thrust modes was used to establish the coefficients for the thrust models for flapping and the propeller assemblies. Using those coefficients, trends were then established to determine the predicted mixed mode thrust and lift, which indicates the maximum takeoff mass. The predicted values for the maximum takeoff mass were then compared to experimentally determine values at various operating conditions during the flight performance determination. This is of particular importance because the quasi-steady assumption for aerodynamic models can be inadequate in determining lift generation in some applications which provides false estimations of maximum takeoff mass and, consequently, payload Shyy et al. [2013].

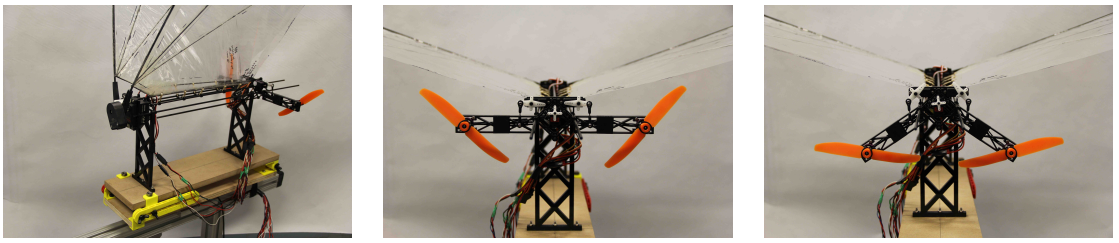

(a) Side view (b) Rear view (Propellers up) (c) Rear view (Propellers down)

FIGURE 4.5: Robo Raven V test stand

4.6 Results

4.6.1 Investigation of Coupling And Vertical Position Sensitivity

For a flapping only baseline, the thrust generated by the wings was measured when operated at 4 Hz with the wing motors powered at the voltage of a slightly depleted two cell LiPo pack, 8.2 V. Given the testing duration, 20 flapping cycles were captured. The results are shown in Table 4.2.

TABLE 4.2: Test Results: Flapping Only

Flapping Frequency	4 Hz
Trail 1 (g)	202.2
Trail 2 (g)	201.9
Trail 3 (g)	202.1
Avg. Thrust (g)	202.0
Std. Dev.	0.13

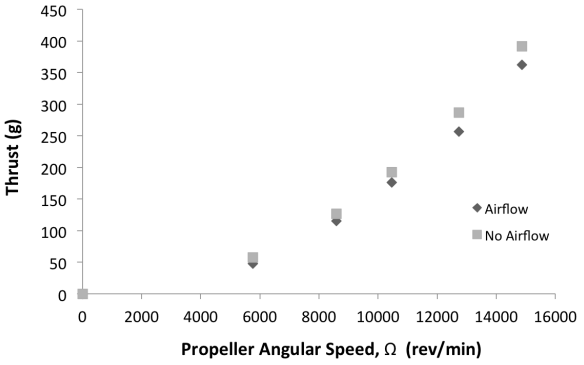

FIGURE 4.6: Propeller thrust with and without airflow vs angular speed, Ω

Thrust measurements using only the propellers were conducted as described in the methodology section. To consider the impact of airflow on the propellers, tests were also conducted without airflow. Both results are shown in Fig. 4.6 as well as the model given by Eq. 4.16. Details about the accuracy of the model will be described in the following section. The presence of airflow only slightly lowers the thrust. This is a positive result, since it implies that a change in freestream velocity should have low impact on thrust production of the propellers, thereby reducing the potential for coupling due to airflow behind the wings. Details of the thrust measurement in airflow, including data for three different trials, are provided in Table. 4.3.

TABLE 4.3: Test Results: Propellers Only with intake airflow of 5 M/S

Motor Input	20 %	40 %	60 %	80 %	100 %
Ω (rev/min)	5759	8583	10469	12734	14873
Trial 1 (g)	49.0	115.8	177.8	256.9	360.5
Trail 2 (g)	46.9	114.7	173.3	255.7	361.5
Trail 3 (g)	46.1	114.7	176.4	256.5	364.0
Avg. Thrust (g)	47.3	115.1	175.8	256.3	362.0
Std. Dev.	1.51	0.65	2.32	0.63	1.79

As noted previously, the expected mixed mode flight performance is the superposition of the thrust generated while flapping only (Table. 4.2) and the thrust generated using the propellers only at various operating conditions of the propellers (Table. 4.3). To compare the measured performance to predictions, the thrust was measured with the wings flapping at a frequency of 4 Hz, while the operating input for the motors was varied from a minimum of 20 % to a maximum of 100 %. 4 Hz flapping frequency was selected as it is the operating frequency for the original platform that produces the most thrust. Given that the flapping wings modify the airflow conditions into the propellers most significantly at a higher frequency, it was postulated that this flapping frequency would generate the maximum amount of coupling, and would therefore be of greatest

interest to investigate. Also, given the possibility that coupling would vary as a function of the vertical position of the propeller, measurements were made with the location of the propellers below the centerline of the platform positioned from 0 mm to 50 mm in increments of 10 mm, as well as at the lowest position, 53 mm. A surface plot of the results can be seen in Fig 4.7.

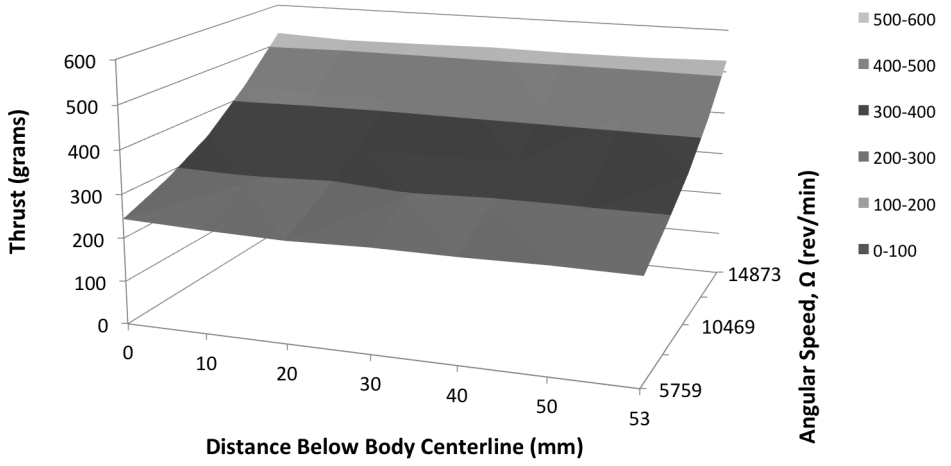

FIGURE 4.7: Average measured mixed mode thrust surface for multiple propeller locations and speeds with 4 Hz flapping frequency

The data in Fig 4.7 indicates the thrust maintains consistent magnitudes for each position for fixed values of propeller angular speed, Ω. Therefore, the thrust appears to be insensitive to position of the propeller assembly. In particular, the shape of the thrust trend is consistent across the surface. The implication of this is the thrust trend observed at any fixed position will be generally descriptive of the trends over the entirety of the operating positions. Therefore, the lowest position of 53 mm was chosen for further characterization, and was also later used in flight testing. The details for the results for this position are shown in Table 4.4.

The lack of variation in the values indicates that coupling is minimal, inducing at most

an 8 % difference. Therefore, these results indicate that the loss term in Eq. 4.15 can be neglected without loss of fidelity in the thrust predictions. The findings of the propeller thrust with no airflow and in airflow (Fig. 4.6) show that there is little variation in thrust despite the change in input airflow. These findings are consistent with the static thrust coefficient measurements conduced by Deters and Selig [2008] with similarly sized scale propellers across numerous Reynolds numbers.

The measurement results indicate that the interaction between the unsteady wake of the flapping on the performance of the propellers is minimal. The mixed mode results are largely consistent with the sum of the thrust predicted by the calculated sum of the individual propulsion modes. Additionally, the trust is insensitive to distance below the centerline given that the thrust trend, increasing with the propeller angular speed, remains consistent despite the operating positions. The implication is that the motor position can be altered without fear that the magnitude of thrust would diminish.

TABLE 4.4: Measured mixed mode thrust (4 Hz flapping)

Motor Input	20 %	40 %	60 %	80 %	100 %
Ω (rev/min)	5759	8583	10469	12734	14873
Baseline Mode Sum (g)	249.3	317.1	377.8	458.4	564.0
Trail 1* (g)	235.8	284.7	352.6	431.5	528.4
Trail 2* (g)	240.3	293.3	350.3	426.7	524.0
Trail 3* (g)	238.1	291.4	345.0	425.6	529.1
Avg. Measured Thrust* (g)	238.1	290.8	349.3	428.0	527.2
Std. Dev.	2.24	4.54	3.90	3.15	2.80

*Measured with propellers located 53 mm below centerline

4.6.2 Model Evaluation

The models for flapping thrust (Eq. 4.5) and propeller generated thrust (Eq. 4.16) were compared to the measured results. These comparisons are shown in Fig. 4.3 and Fig. 4.8, respectively. In order to determine coefficients for the models, the thrust measurement from 3 Hz was used for the flapping because of the saturation of the

trend (the reduction of the value ascent) beyond 3 Hz which is attributed to aeroelastic effects, the mechanical properties of the wings and their ability deform to displace air. As indicated previously, the notable departure in the thrust response at 4 Hz in Fig. 4.3, where the model predictions exceeds the measured data, indicates the aeroelastic effects of the wing itself go beyond the change in flapping amplitude. The models are in good agreement with the measured data gathered for the flapping and propeller performance as there is, at most, 9 % difference between the measured value and that of the model for flapping and 15 % for the propeller data (the remainder of the propeller values are all less than 5 %). Using the sum of the two thrust models, a surface plot was created to predict the thrust for various operating conditions. These results are shown in Fig. 4.9. The results across 4 Hz flapping frequency are shown in Fig. 4.10 for the measured mixed mode thrust, the sum calculated from the measured thrusts for each mode, and the sum from the models of thrust for each mode. The modeled thrust response also over predicts the experimental measurements in Fig. 4.10, but is consistent with Fig. 4.3, since the flapping model is summed with the propeller model. For the motor model, 100 % motor input or a propeller angular speed, Ω, of 14873 rev/min was used.

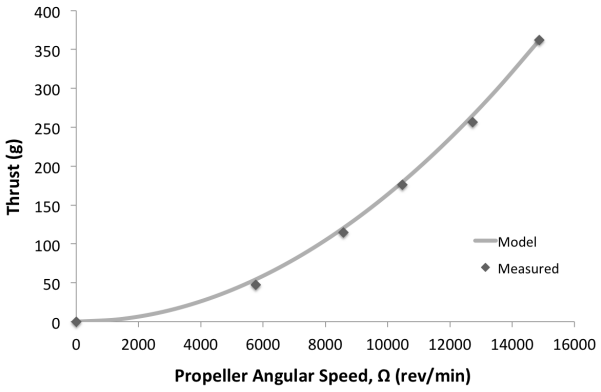

FIGURE 4.8: Average measured and modeled propeller thrust vs angular speed

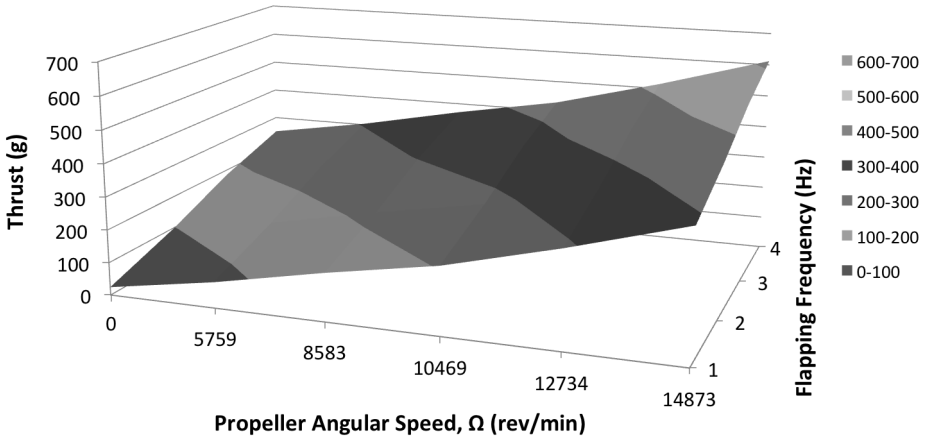

FIGURE 4.9: Modeled mixed mode thrust

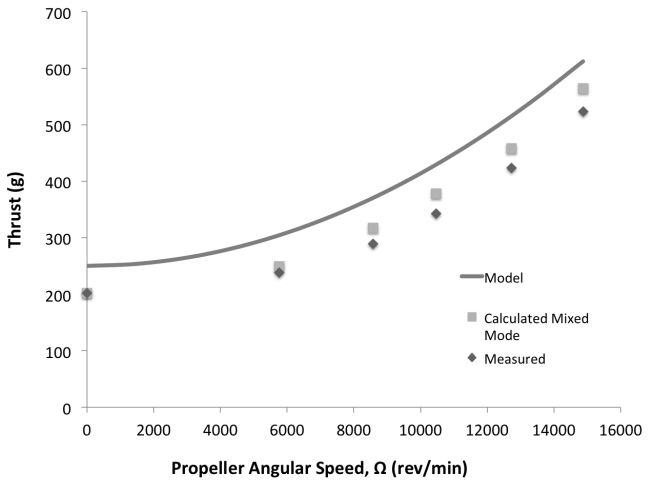

FIGURE 4.10: Average mixed mode measurements, superposed mode measurements, and modeled mixed node thrusts vs propeller angular speed, Ω (4 Hz flapping)

4.6.3 Thrust Generating Efficiency

While higher thrust is valuable, the trade off is both the weight added and power required to produce that thrust. In this regard the efficiency of thrust generation per unit mass (as given in Eq. 4.21) and thrust generation per unit of actuator power, P, (as given in Eq 4.22) are useful for comparison. As actuator mass is fixed, efficiency of thrust per mass is the highest value at the highest thrust available.

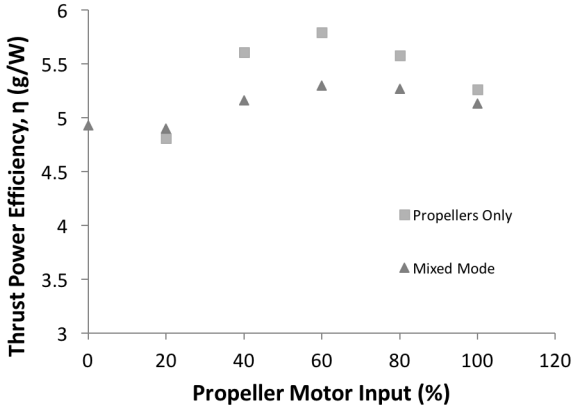

FIGURE 4.11: Thrust power efficiencies

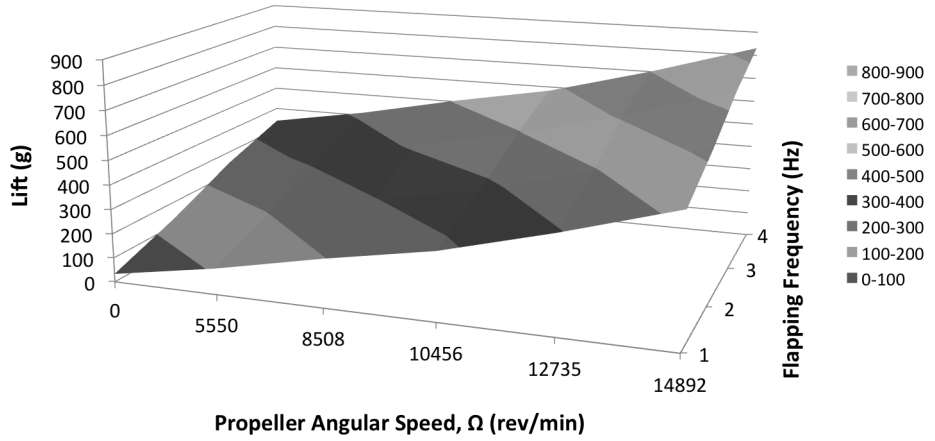

FIGURE 4.12: Modeled mixed mode lift

$$\Gamma = \frac{Thrust}{M} \tag{4.21}$$

The wings generate 202 grams of thrust. The Futaba servos weigh 72 grams, 144 grams for the pair. The flapping generates has a mass efficiency, Γ, of 1.4, grams of thrust per gram of actuator mass. As noted previously, the major challenge of creating a flapping with platform is actuator performance and weight. The propellers generate 362 grams of thrust when operating at 100 % motor input. The total weight of the propeller assembly pair weighs 97.2 grams. This yields a mass efficiency Γ, of 3.7. The propeller assemblies

are more efficient at generating thrust per unit mass. For the mixed mode case, the mass efficiency of the two is 2.2, where the total thrust is 527.2 grams (the average of the experimental trails) and the mass is 241.2 grams. The addition of the propellers increases the thrust efficiency per unit mass compared to pure flapping (Γ of 1.4).

$$\eta = \frac{Thrust}{P} \tag{4.22}$$

While the mass of the actuators is fixed, the power input for each mode is not. The efficiency for the thrust produced per unit of power, η, where power is the product of the operating voltage and current, is another useful metric. Since the flapping was set to 4 Hz for all the mixed mode results in this work, only the power required for 4 Hz flapping is worth considering. The voltage used in each calculation is 8.2 V; the value of a slightly depleted lithium polymer battery. The efficiency, η, of the flapping is 4.93 g/W. This is the series shown at zero for the percentage of motor input in Fig. 4.11. The efficiency of the propellers operating at different operational points operating along and in the mixed mode case are are shown in Fig. 4.11. Aside from the condition of 20 %, each of the efficiencies for the remaining motor inputs are more efficient than the flapping case. In the mixed mode operation the efficiencies are higher for each motor operational point aside from 20 % motor input. The highest efficiencies in the propeller only case and the mixed mode operation both occur at 60 % motor input as shown in Fig 4.11.

4.6.4 Mixed Mode Flight Performance

4.6.4.1 Flight Validation

Flight tests confirmed that Robo Raven V is capable of mixed mode flight using flapping and propellers. They also revealed that the platform is capable of other styles of flight: flight using the propellers as the sole propulsion mode after reaching a critical velocity (either by a launch or by use of both modes initially), intermittent flapping, and gliding. The propeller only and gliding is possible because the wings passively balloon into a suitable airfoil shape in flight. (Using flexible wings with propeller propulsion has been studied in other work Ifju et al. [2002], Shyy et al. [2005]). Notably, gliding via the use of gravity to generate velocity is viable. At altitude, the propellers and flapping can be halted so that the wings can be held still at shallow dihedrals to achieve gliding. The gliding profiles can be altered into diving profiles by increasing thecom dihedral of the wings. Additionally, the back loop capability demonstrated with Robo Raven I was maintained. For flight footage of Robo Raven I please visit: https://www.youtube./watch?v=mjOWpwbnmTw. For flight footage of Robo Raven V please visit: https://www.youtube.com/watch?v=Yryz8PSAwmA.

4.6.4.2 Determination of Payload Capacity

Increasing payload capacity was a principal goal in the development of Robo Raven V. The trade off in the approach is that the operating empty mass increases with the addition of the propeller assemblies and supporting hardware. The increase in operating empty mass must be offset and exceeded to increase the payload. A true improvement to payload maintains higher payload while maintaining comparable flight time across the entire operating range.

In order to ascertain the payload, two masses are recorded during flight tests. The operating empty mass, which is the total mass of essential components (with the exception of the power source as it can be varied), and the flight mass which is the sum of operating empty mass and the mass of the payload as follows:

$$M_{Flight} = M_{FWAV} + M_{Pay} \tag{4.23}$$

Rearranging Eq. 4.23, the payload is simply the difference between the flight mass and the operating empty mass:

$$M_{Pay} = M_{Flight} - M_{FWAV} \tag{4.24}$$

The maximum payload is the maximum takeoff mass, which occurs when the weight offsets the total lift, minus the operating empty mass.

$$M_{Pay,Max} = M_{Flight,Max} - M_{FWAV} \tag{4.25}$$

As described in section 4.2, lift should be equal to the weight (Eq. 4.8). Furthermore, based on Eq. 4.12, the lift should be equal to the product of the thrust and ratio of the coefficient of lift, C_L, and the coefficient of drag, $C_{D,p}$. Using the modeled thrust for flapping alone, Eq. 4.5, and the sum of the modes given in Eq. 4.19, the expected lift was determined and plotted in Fig. 4.12. In order to determine the ratio of the drag and the lift, the maximum payload (described in more detail in the Payload Determination subsection) and the maximum thrust at 4 Hz flapping and 100 % motor input (Ω = 14873 rev/min) were used. The ratio of coefficient of lift to coefficient of drag is 1.36. Flight tests were conducted outdoors to attain maximum takeoff mass and payload.

The final takeoff mass of Robo Raven I after payload testing was 328.8 g. Given the operating empty mass of 285.0 g, the maximum payload available was 43.8 g using Eq. 4.25. The maximum takeoff mass of Robo Raven V was achieved performing payload tests outside on a calm day with the adjustable arms at their maximum distance below the centerline, 53 mm, the propellers running at 100 % full speed and the wings flapping at 4 Hz. The operating empty mass for Robo Raven V was 438.1 g. The maximum takeoff mass was 711 g, which was approximately 14 % less than the predicted takeoff mass of 831 g in Fig. 4.12, which is attributed to the overpredicted thrust in Fig. 4.10 at the 4 Hz flapping frequency. Subtracting the operating empty mass of 438.1 g, the payload is 272.9 g (Eq. 4.25). While the payload capacity increased by 229.1 g for take off, a true improvement also requires accounting for the effects of the power draw on the portion of the payload capacity that will be taken up by the battery mass required for a desired flight time.

4.6.4.3 Flight Time Estimation

The payload that is available is divided between the energy source required to power the platform and the operational payload which can be used to carry sensors (Eq. 4.26).

$$M_{Pay} = M_{Bat} + M_{Op} \tag{4.26}$$

There is a minimum battery mass required to power the platform, after this basic amount, operational mass can be traded to increase flight time. The minimum battery mass is the the mass required to provide the operating current. The continuous current, I, is the product of capacity and the lower value of the C rating, the rate at which the battery can discharge current. If the continuous current and C rating are

given, the capacity can be found working backwards. The battery capacity divided by the battery mass, ξ (Eq. 4.27) can then relate capacity and mass.

$$\xi = \frac{Q}{M_{bat}} \tag{4.27}$$

After finding the minimum battery size, the upper bound is based on mass because of payload availability. The product of voltage and the capacity of the battery, Q, is the energy available. If power consumption is known, an aggregate estimation of flight time is given in Eq. 4.28.

$$t_f = \frac{QV}{P} \tag{4.28}$$

In order to make fair comparisons of performance, the value of ξ must be held constant. Robo Raven I is powered by a 27 g Turnigy 370 mAh, 25 C nano-tech battery where ξ is 13.7 mAh/g. This value of ξ used to compare payload benefits. In practice, the general trend is that ξ, the ratio of the battery capacity to battery mass, increases in a favorable manner because battery capacity, which is a function of volume, scales differently than packaging mass, which is a function of surface area.

Robo Raven I draws 41 W of power between the main wing motors and a nominal power demand of the tail servo. The minimum battery that can be used safely is a 200 mAh LiPo battery given a C rating of 25 which yields a flight time of 2 min and 24 s and weights 14.6 g maintaining ξ of 13.7 mAh/g. The final flight mass of Robo Raven I after payload testing was 328.8 g. Given the operating empty mass of 285.0 g, the maximum payload available 43.8 g using Eq. 4.25. Given the minimum battery mass, the operation payload remaining is 29.2 g which represents 10.2 % of the operating empty mass. If the

entire payload is occupied with a battery (maintaining the same value of ξ) the largest battery capacity, Q_{max}, is 600 mAh which provides a flight time of 7 minutes and 12 seconds.

Robo Raven V, operating at 100 % propeller speed and 4 Hz flapping, Robo Raven V draws 113.16 W. Given the higher current demand, at minimum, a 552 mAh 25 C LiPo must be be used for continuous safe operation. Maintaining the ξ value of 13.7 mAh/g, the minimum mass of a 552 mAh battery is 40.3 g and yields a flight time of 2 minutes 24 seconds.

The operating empty mass for Robo Raven V was 438.1 g. The maximum takeoff mass was 711.0 g. Subtracting the operating empty mass of 438.1 g, the payload is 272.9 g. In order to carry the minimum required battery with a mass of 40.3 g, the operational payload available would be 232.6 g which represents 53.1 % of the Robo Raven V operating empty mass. If the entire payload is occupied with a battery (maintaining the same value of ξ) the largest battery capacity is 3,740 mAh which yields a flight time of 16 minutes and 16 seconds.

As noted previously, a 27 g 370 mAh, 25 C battery is typically used for Robo Raven I. Subtracting the battery mass from the payload, the operational payload is 16.8 g by Eq. 4.26 which represents 5.89 % of the operating empty mass of Robo Raven I. Based on usage, the flight time using 370 mAh battery is 4 minutes 26 seconds. The closest available commercial battery to provide similar flight time for Robo Raven V is a Turnigy nano-tech 950 mAh battery ($\xi = 20.6$ mAh/g) which provides a flight time of 4 minutes 8 seconds. With a 950 mAh battery, the remaining operational payload for Robo Raven V is 226.9 g which is 51.8 % of the Robo Raven V operating empty mass.

Comparison of the physical parameters and electrical specifications for Robo Raven I and V can be seen in Table. 4.5.

TABLE 4.5: Comparison of Robo Raven I and Robo Raven V Platforms For Similar Flight Times

Parameter	Robo Raven I	Robo Raven V
Operating Empty Mass (g)	285.0	438.1
Maximum Takeoff Mass (g)	328.8	711.0
Maximum Payload (g)	43.8	272.9
Battery Mass (g)	27	46
Operational Payload (g)	16.8	226.9
Operational Payload/Operating Empty Mass (%)	5.89	51.8
Battery Capacity (mAh)	370	950
Battery C Rating	25	25
Battery Safe Continuous Current (A)	9.25	23.75
Platform Operating Current Draw (A)	5	13.4
Flight Time	4 min 26 s	4 min 8 s

Taking the minimum and maximum values for flight time and percentage of operational payload and graphing increments in between them, Fig. 4.13 was generated. What is notable is that across the entire range of flight times, the ratio of operational payload relative to operating empty mass remains higher for Robo Raven V than Robo Raven I. While the slope is steeper for Robo Raven V, the initial value is much higher given the available payload. The lines never intersect. The implication is that for the same flight time (going up vertically) the payload is higher. Additionally, the right endpoint indicates that the ultimate flight time, made available by the payload, is improved despite using a poor estimate of ξ, capacity to mass ratio.

As noted previously, increasing the battery capacity tends to come with a disproportionately smaller increase in mass. This means that the value of ξ increases in a favorable manner with larger battery capacities if the electrical connector remains the same (the fixed mass with a heavier connector skews the scaling). For example, a 950 mAh battery of the same brand, has a mass of only 46 g which yields a ξ value of 20.6 mAh/g. This

difference works to shift the right endpoint in Fig 4.13 and lower the slope of the line in a favorable manner. The result is more payload capacity, as well as flight time.

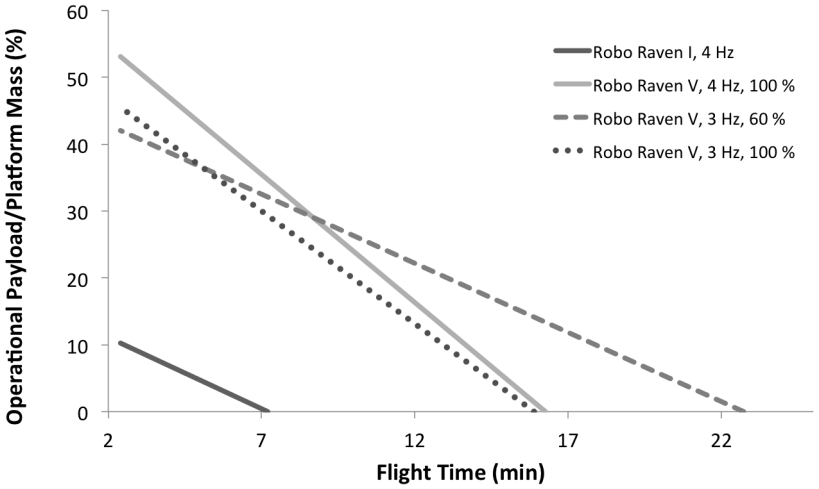

FIGURE 4.13: Operational payload/operating empty mass (%) vs flight time (minutes)

What is interesting is to consider the effects of changing the operating conditions. Specifically, the operating conditions for the mixed mode cases of 3 Hz flapping with 60 % motor input and 3 Hz 100 % motor input, which are also shown in 4.13. The wattage consumed was adjusted accordingly based on the change in power consumption associated with 3 Hz flapping and 60% versus 100% motor input. Despite a lower ultimate payload, 3 Hz flapping with 60 % motor yields a longer flight time. The efficiency of the thrust generation is highest for this condition, as shown in Fig. 4.11. The most interesting result is the comparisons of 3 Hz flapping and 4 Hz flapping with 100 % motors. The 4 Hz case produces a higher payload and higher consumption. In contrast the 3 Hz has lower consumption but has a lower starting payload. Therefore, it is clear a trade-off scenario exists between the operational payload and the propulsion efficiency for the flapping frequency and motor input conditions, which we have been able to characterize.

4.7 Discussion

Research findings from flapping wings have focused primarily on LEVs, and have indicated that unsteady effects are integral to force generation for flapping wings regardless of if they are flexible or are rigid airfoils which pitch and surge Mancini et al. [2015b], Muijres et al. [2008]. Research considering membrane wings such as mammalian flight, though largely focused on insect scale for micro air vehicles, indicates that LEVs are important mechanisms for force production Jones and Babinsky [2010], Muijres et al. [2008], Wu and Sun [2005] and that trailing airflow effects are generally secondary but still important (particularly for micro air vehicles) Platzer et al. [2008], Wu and Sun [2005]. Research by Ho et al. [2003] exploring membrane wing design indicates that the lift generating section of the wing for this type of wing design is toward the wingtip, which is positive for payload carrying capability in this application, while thrust generating section is closer to the body which would have more interaction with the propellers given their location. Unfortunately, models addressing outflow conditions and the implications of disruptions to the outflow conditions on flapping wing performance are still forthcoming as research into this area is developing Jones and Babinsky [2010], Platzer et al. [2008].

Experimental studies have also been conducted to visualize the flow at the leading edge of waving and flapping wings Ho et al. [2003], Jones and Babinsky [2010], Jones et al. [2011], Muijres et al. [2008], Platzer et al. [2008], Wu and Sun [2005]. The most notable findings have been the development of LEVs lead to the formation of unsteady flow structures, which tend to increase towards the tips of wings or flags. The three dimensional nature of these structures is well-visualized in Jones et al. [2011] and Muijres et al. [2008]. In light of these findings, we wanted to investigate mounting propellers to the rear of

flapping wings to minimize the effects of the propeller outflow on the formation of LEVs, aside from an expected increase of freestream velocity from the added thrust from the propellers. It is also noted by Beals and Jones [2015], Song et al. [2008], Zhao et al. [2009] that, given their aeroelastic behavior, compliant wings are likely better at adapting to unsteady conditions as the wing deforms differently depending on the flow present. This change in deformation in response to flow conditions likely explains the limited performance reductions we observed. An example of adaption of the deformation in the presence of varying flow, albeit closer to freestream variations, was clearly observable during fight tests when the wings balloon into a cambered shape when in a gliding motion.

By mounting the propellers at the rear, it also became of interest to understand if the unsteady flow produced from the trailing edge of flapping wings would be extremely damaging to thrust generation for propellers. While there has been some work on non-uniform inflow conditions to propellers for rotorcraft (such as ground effect) Chen [1989], the characterization of scale propellers (compounded by the plethora of available designs) in oblique flow (i.e., flow where there is a non-zero angle between the plane of the propeller and the freestream wind velocity) or unsteady flows, is a newer area of research being driven by increasing demands in performance for unmanned aerial vehicles Powers et al. [2013], Theys et al. [2016]. In these studies, force measurements have been conducted for thrust generated from propellers in oblique flow. Specifically, an experimental and numerical study of scale propeller performance in oblique flow was conducted as a preliminary step in the design and development of a Vertical Take off and Landing (VTOL) platform Theys et al. [2016]. The thrust findings indicate that the thrust values and trend are consistent across numerous angles between 0 and 90 degrees. The largest fluctuation occurred when the freestream was 90 degrees, perpendicular to

the tip plane of the propellers. However, the trend and average values were found to be similar, within the range of the expected measurement error. A similar inquiry was conducted by Powers et al. [2013], where the propeller performance in a quadrotor was considered in forward flight for ground and ceiling effects. To access forward flight in oblique flow, five angles of attack and four wind speeds at each angle were considered. The findings showed that the total thrust produced by the rotor decreases as wind speed in a given direction increases. As the angle of attack increases, the thrust variation due to wind speed decreases, as the component of wind velocity perpendicular to the rotor increases more slowly. These findings are consistent with the finding in Fig. 4.6. In the presence of no freestream, the thrust produced is higher than in the freestream flow. The promising results from all of these investigations indicate the sensitivity of the thrust to inflow, albeit steady, at an angle is generally low. Additionally, the findings of Powers et al. [2013] indicate as the overall thrust decreases, the sensitivity of the thrust to an increasing freestream velocity will decrease. This is particularly true when the angle of inflow is low. Thus, these findings support those from our current study, which indicate inflow conditions to a scale propeller may not be as damaging to thrust performance when it is located behind the trailing edge of a flapping wing.

In the Robo Raven V platform, the flexible flapping wings are much larger relative to the size of the propellers. The duration of time that the wings are in front of the propellers is limited given the periodic motion of the wing (as a function of the flapping frequency). The propellers are also located close to the attachment point of the wings to the body, away from the wing mid span. Given the flow visualization in the studies noted above (Ho et al. [2003], Jones and Babinsky [2010], Jones et al. [2011], Muijres et al. [2008], Platzer et al. [2008], Wu and Sun [2005], unsteady flow structures likely tend to form from the mid span towards the wing tips. It is noted by Ho et al. [2003]

that the linear speed of the wings is higher towards the tips and leads to stronger vorticity. Keeping the propellers away from these areas can limit interactions. As a result, the airflow velocities are likely closer to the freestream velocity. Regardless, given the consistency of the thrust coefficient measurements conducted by Deters and Selig [2008] with similarly sized scale propellers across numerous Reynolds numbers, and the findings of Powers et al. [2013], Theys et al. [2016] in oblique flows, it is unlikely a change in inflow velocity would greatly change propeller performance, although there has been conjecture it should be lower Powers et al. [2013]. Therefore, by (a) locating the propeller along the flapping wing away from unsteady vortex structures and (b) limiting the area available for interaction between the wing and propeller, we have been able to effectively eliminate wing-propeller interactions. It is also important to note that for the flapping wings at a typical freestream velocity of 10 m/s for Robo Raven V with a 1.168 m wingspan and a $\Delta\alpha$ f of 2.09 rad/s, the advance ratio is 6.42, while the advance ratio of the propeller is 0.318 at maximum power. Therefore, the relative advance of the propeller is nearly 20X that of the flapping wing, which further limits the time of interaction between the two to minimize effects.

Flight testing has also indicated that the addition of the propeller is valuable, because it allows higher performance with regard to total lift, and ultimately the payload capacity. At lower flapping frequencies, the measured payload outperforms the lift predicted from the quasi-steady state model prediction using the sum of the individual modes. However, the modeled lift over predicted the payload at 4 Hz flapping due to the aforementioned aeroelastic effects. Using both propulsion modes, Robo Raven V significantly outperforms the original Robo Raven I platform, which utilized flapping only. Across the entire operating range the payload was higher for similar flight times. Furthermore, the maximum flight time was significantly higher. If batteries with higher specific energy

capacity are utilized, the performance will continue to improve. In flight, the bi-modality provides interesting opportunities, specifically the ability to switch flight conditions. As demonstrated in the flight footage mentioned in Section 4.6.4.1 for Robo Raven V, the propellers can be used to rapidly increase forward velocity and climb rate, while flapping can be used to maintain flight at lower forward velocities. The propellers can also be used to impulsively load the wings at angles above their stall angle to increase the lift coefficient. In addition, the propellers and flapping can both be halted, allowing for execution of various aerobatic maneuvers, such as gliding, diving, or loops, that can be controlled simply through the static adjustment of each wing's position.

4.8 Conclusions

In this work, a FWAV with independent wing control and a wake positioned propeller assembly is presented as a means of increasing aerodynamic force generation to increase payload capacity in a mixed mode propulsion condition. The findings show that, first, there is no notable cross-linking/coupling between the two propulsion modes (i.e., flapping wings and propellers). Second, thrust generated by the propellers is not sensitive to the propeller assembly position in the wake of the wings as there were consistent thrust trends at various motor operating points across multiple vertical positions of the propellers. Finally, adding propeller propulsion to FWAV is a viable means of increasing aerodynamic performance specifically thrust production and, subsequently, aerodynamic lift to increase payload capacity.

Results indicate that using propellers in conjunction with the wings can increase thrust as much as 261 % at full signal. The resulting increase in thrust increases the available payload from 43.8 g to 272.9 g. While it was determined that the propeller assembly

increases current draw by 176 % when operating at 100 % operational power, if all of the additional payload is occupied by batteries to power the platform, flight time can increase 341 % over the initial design. Thus, despite the increased power requirements, the lift benefits provide a significant enhancement of operational performance through increases in payload or flight time. The measured enhancements also conformed to predictions from models of the aerodynamic forces generated by the mixed mode propulsion. In addition, the effect of varying the amount of operational payload on flight time for different mixed mode operating conditions was predicted, and the tradeoff between the operational payload and the propulsion efficiency for the flapping frequency and motor input conditions was characterized. The bi-modality can be leveraged to perform aerobatic maneuvers, such as gliding, diving or loops, that can be controlled through adjustment of the static position of each wing.

This current work focused on using thin membrane wings that are very flexible and amenable to generating sufficient aerodynamic force to achieve flight through the flapping mode only. Conventional fixed wings tend to be much stiffer and heavier in order to maintain a more aerodynamic shape, hence they require signification power to flap. Future directions for this work include: examining new styles of morphing wings with more aerodynamic shapes conducive to generating aerodynamic lift through fixed wing flight, while also being light enough to flap. Another direction for future work is the automatic selection of the two modalities to fit various weather conditions and missions.

Chapter 5

Deceleration via Inertial Control on a Propeller Assisted Flapping Wing Air Vehicle

5.1 Introduction

Biological systems demonstrate marvelous feats of maneuverability and fluidity of movement. Reproducing such behavior is challenging despite being having actuators that can be precise and accurate in position control. Based on examples in nature, rigorous position control of an end effector, while generally favorable for manufacturing, may be more valuable as a parallel task with interaction force, or leveraging changes in center of mass and inertia. Lizard species right themselves and control aerial motion using the mass and inertia of their tails Chang-Siu et al. [2013], Libby et al. [2012], Cheetahs that use their tails to provide turning stability and break when running Briggs et al. [2012], Patel and Braae [2014], and people leverage their arm mass while jumping Hayashi and

Tsujio [2001]. Birds demonstrate abilities such as perching, rapid turning, and grasping tasks Doyle [2011], Thomas et al. [2014] leveraging adaptive morphology to manipulate mass Mintchev and Floreano [2016] and airflow mechanisms. Given the growing interest in increasing capabilities unmanned aircraft systems (UAS) and unmanned aerial vehicles (UAV), achieving similar feats to natural flyers with man made aerial systems is compelling. For example, maneuverability is useful for obstacle avoidance in cluttered environments. Additionally, perch and stare capabilities are appealing as they allow for imaging and station keeping with low energy cost or may even allow for recharging if used in conjunction with photovoltaics Doyle [2011].

The richness of the feature set demonstrated by natural systems has prompted a number of robotic platforms as a result of bio-inspiration. A cheetah-inspired robot capable of running and jumping over a robot that controls reaction forces with the ground has been developed Wensing et al. [2017]. The system model for jumping but, more importantly, landing is simplified enough to be done on board but powerful given repeated demonstrations of jumping and landing. Usage of an inertial tail was proposed to provide stability to that robot Briggs et al. [2012]. The body was presented as one element and the tail another, with corresponding reaction forces and torques between them. Even with a simplified model, the addition of the tail proved valuable in simulation and testing. In work by Rone et al. [2018], continuous deformations of biological tails were mimicked using a serpentine robotic capable of exerting forces on its base with future applications such as integration with a bipedal robot to provide control. In addition to biological strategies, there are other means of generating forces and moments including reaction wheels, reaction masses, and propellers which are of note given their usage on robotics aerial platforms. A useful table summarizing properties of force and moment application technologies is provided by Briggs et al. [2012] and a short summary of the concepts is

provided by Rone et al. [2018].

A spinning mass was used for inertial control for a small legged terrestrial robot in Casarez et al. [2013]. A limited tail was used for turning for a terrestrial legged robot Kohut et al. [2013a]. In related work to Kohut et al. [2013a], aerodynamic steering of a terrestrial robot was considered. It was found that the sail could be dynamically actuated to cause a rapid change in body orientation through inertial effects alone Kohut et al. [2013b]. Specifically, a mechanism was actuated without the drag inducing sail. It was found to create a change in position without the sail due to motion of the mass.

In addition to planar motion on the ground, inertial control has been utilized in jumping and aerial cases. In Iida et al. [2002] swinging pendulums were used to induce bipedal hopping gaits. Human inspired jumping using winging pendulum arms was studied by Hayashi and Tsujio [2001]. A rolling robot with the ability to jump to clear obstacles uses a 1 DOF tail to control position during the jump Zhao et al. [2013, 2015]. Inspired by lizards, an active tail was used to self right on a wheeled terrestrial robot Chang-Siu et al. [2011], Li et al. [2015]. Also following the biological example of lizards, control of a tail was used for self righting of a 2 DOF robot Chang-Siu et al. [2013]. A strictly jumping robot, which uses a series elastic actuator in conjunction with a variable mechanical advantage to store energy and jump, used an inertial tail to stabilize while in air Haldane et al. [2016]. Continuing from that work, thrusters (propellers) were used to stabilize midair in addition to inertial tail Haldane et al. [2017]. Battery mass was used to augment control of a quadrotor in Bouabdallah et al. [2006]. Specifically, the battery was actuated in order to move the center of mass relative to the thrust vectors produced by the propellers. The mass and inertia of the manipulator mounted to a quadrotor was utilized in order to stabilize quadrotor as a secondary task when not gripping Santamaria-Navarro et al. [2014], making the gripper multifunctional. In

a flapping wing case, an inertial tail was used to provide control on a nano air vehicle Penskiy et al. [2012].

5.2 Goal

The goal of this work is to use inertial control to provide rapid deceleration of an aerial vehicle. Specifically, a reaction mass mechanism, using the platforms own battery in addition to an actuator, is presented as a means of modifying angle of attack to apply breaking. If successful, applications include obstacle avoidance, improving imaging (as more time is provided over a target area due to lower flight velocities), and flight features which may be promising for perching.

5.3 Center of Mass Modifying Angle of Attack

5.3.1 Flat Plate Model Equations of Motion

During flapping flight, aerodynamic thrust and lift forces undergo periodic variations. A common modeling approach is to use a quasi-steady state assumption Madangopal et al. [2004], Shyy et al. [2013]. Quasi steady-state wing theory assumes that the forces on a moving wing are equivalent to the sum of the forces on a fixed wing over a sequence of attitudes that track the wing motion. This model neglects acceleration forces and unsteady aerodynamic effects" Muijres et al. [2008]. The wings and tail modeled as plates where the wings are modeled together as an ellipse. It is assumed that the sum of forces acting on the wing can be replaced by an average value of the aggregated values of the various positions achieved by the wings. Each force is assumed to act on the center of area of its respective plate.

We define the rotation matrix about the pitch axis by Eq. 5.1: Pitch rotation

$$R_y = \begin{bmatrix} \cos\theta & 0 & \sin\theta \\ 0 & 1 & 0 \\ -\sin\theta & 0 & \cos\theta \end{bmatrix} \tag{5.1}$$

where θ is the current pitch. It is assumed that forces along the direction of plate are negligible. The force vector acting perpendicular to each plate is defined using the standard drag equation:

$$\vec{F}_{plate(i)} = \frac{1}{2}\rho_{air} C_D A_{plate(i)} (\vec{V}_{(i)} \cdot \vec{n}_{plate(i)})^2 \vec{n}_{plate(i)} \tag{5.2}$$

where ρ_{air}, and C_D are the air density and drag coefficient, $\vec{n}_{plate(i)}$ is the normal vector to the plate in the direction of the drag force, and $\vec{V}_{(i)}$ is the velocity of the center of area of the ith plate. Note that $\vec{V}_{(i)} = \vec{V}_{CG} + \vec{\omega} \times \vec{p}_{plate(i)}$, where $\vec{\omega}$ and $\vec{V}_{CG}$ are the platform's angular velocity and the velocity of the center of gravity, respectively. $\vec{p}_{plate(i)} = Rot(\theta_P)\vec{p}^{\,0}_{plate(i)}$ are the coordinates of the centroid of the plate area from the center of gravity at a particular moment in time. Note that $\vec{p}^{\,0}_{plate(i)}$ is the position of the center of area of the ith plate with no rotation. $\vec{n}_{plate(i)}$ is calculated using the rotation matrix and the normal plate vector $\vec{n}^{\,0}_{plate(i)}$ when $\theta_P = 0°$ using Eq. 5.3:

$$\vec{n}_{plate(i)} = Ry(\theta)\vec{n}^{\,0}_{plate(i)} \tag{5.3}$$

For flight with a consistent velocity and angle of attack there must be equilibrium both forces and moments with respect to the center of mass Anderson [2012]. If both the moments and forces are summed to zero the motion will be a state of equilibrium.

In the vertical direction the force balance is the following:

$$\sum \vec{F}_{plate(i),z} + \vec{T}sin\theta - mg = 0 \tag{5.4}$$

In the horizontal direction the force balance is as follows:

$$\vec{F}_T cos\theta - \sum \vec{F}_{plate(i),x} = 0 \tag{5.5}$$

If the center of pressure is behind the center of mass then a compensating moment needs to be present, such as a moment provided by a tail. We calculate the moments caused by the airflow acting on each plate by Eq. 5.6:

$$\vec{M}_{plate(i)} = \vec{p}_{plate(i)} \times \vec{F}_{plate(i)} \tag{5.6}$$

$$\vec{p}_{plate(Tail)} \times \vec{F}_{plate(Tail)} - \vec{p}_{plate(Wings)} \times \vec{F}_{plate(Wings)} = 0 \tag{5.7}$$

When the center of mass changes the value of the components of $\vec{p}^{0}_{plate(i)}$ change affecting the moments in Eq. 5.6 and the sum of moments 5.7.

When the center of mass moves the distances of contributing forces to the center of mass will change, resulting in an imbalance of moments. A rearward move of the center of mass would result in a larger angle of attack as shown in Fig 5.1. Alternatively, a forward center of mass would result in a shallower angle of attack. To predict the change in distance, a mass model is used.

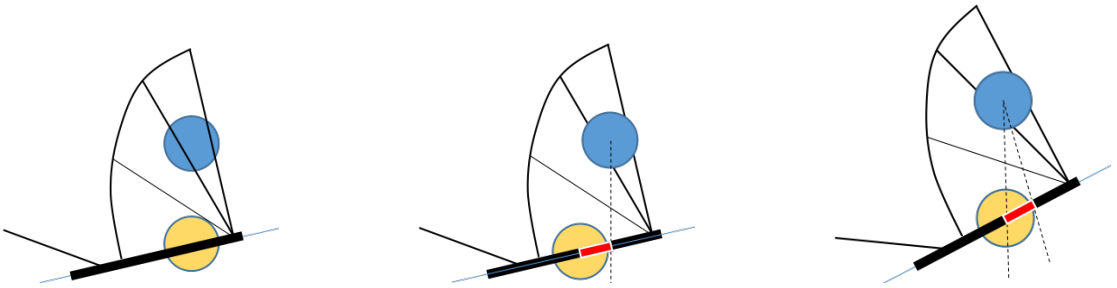

(a) Normal Configuration (b) CG Moved Backward (c) New Angle of Attack

FIGURE 5.1: CG Effect on angle of attack with lift acting behind the center of mass

5.3.2 Center of Mass Model

In the case of two masses, the expressions for the center of mass, $\bar{x_1}$, is the following:

$$\bar{x_1} = \frac{x_1 M_1 + x_2 M_2}{M_1 + M_2} \tag{5.8}$$

Changing location of the center of mass by a distance, c, from $\bar{x_1}$ to $\bar{x_2}$ is the following:

$$\Delta\bar{x} = \bar{x_2} - \bar{x_1} = c \tag{5.9}$$

If we define the original center of mass as the origin, then $\bar{x_1} = 0$:

$$\bar{x_1} = \frac{x_1 M_1 + x_2 M_2}{M_1 + M_2} = 0 \tag{5.10}$$

Then

$$\Delta\bar{x} = \bar{x_2} = c \tag{5.11}$$

One means of changing the center of mass is to increase mass of one of the two mass relative to the other. Assume the second mass, M_2, is increased by an amount, m.

$$M_2' = M_2 + m \tag{5.12}$$

$$\frac{x_1 M_1 + x_2 M_2'}{M_1 + M_2'} = c \tag{5.13}$$

The center of mass will tend toward the larger one. Note that the magnitudes of x_1 and x_1 must be larger than c to achieve a change of c. Another means is by modifying distance. If the change of center of mass is accomplished moving the second mass, M_2, by a distance, a, then:

$$\bar{x_2} = \frac{x_1 M_1 + (x_2 + a) M_2}{M_1 + M_2} \tag{5.14}$$

Substituting into Eq. 5.11 becomes:

$$\frac{x_1 M_1 + (x_2 + a) M_2}{M_1 + M_2} = c \tag{5.15}$$

Simplifying:

$$\frac{x_1 M_1 + x_2 M_2}{M_1 + M_2} + \frac{a M_2}{M_1 + M_2} = c \tag{5.16}$$

Note that the term $\frac{x_1 M_1 + x_2 M_2}{M_1 + M_2}$ is the original center of mass, $\bar{x_1}$ which was defined as 0 in Eq. 5.10. In light of this, Eq. 5.16 becomes

$$0 + \frac{aM_2}{M_1 + M_2} = c \tag{5.17}$$

Thus

$$\frac{aM_2}{M_1 + M_2} = c \tag{5.18}$$

5.3.3 Inertial Effects Explored on Robotic Flapping Wing Platforms via Passive Mass Location

5.3.3.1 Passive Mass Effect on Flapping Wing Flight

Robo Raven, Fig. 5.2, is a flapping wing unmanned air vehicle (FWUAV) which features independent control of flexible, passively deforming carbon fiber reinforced Mylar wings. The wing control can be leveraged to do a back flip, dive and other aerobatics. A description is provided by Gerdes et al. [2014] and many of these capabilities are demonstrated in flight footage available at `https://www.youtube.com/watch?v=mjOWpwbnmTw`. Robo Raven has subsequently been adapted for research pursuits including: platform wing sizing and motor performance (II) Gerdes et al. [2013b, 2015], harvesting solar energy (III) Perez-Rosado et al. [2014, 2015a,b], autonomous flight control for loitering and dihedral based diving (IV) Roberts et al. [2014, 2015, 2016], increasing payload capacity and maneuverability (V) Holness et al. [2015, 2018a], and integrated flexible energy storage (VI) Holness et al. [2016].

In order for the Robo Raven to fly, the battery and electronics would have to be placed aft to move the center of mass rearward to offset the contribution from the front servos which are the largest mass contributors. Without aft placed electronics and battery working in conjunction with a raised tail, the platform is too nose heavy and tends to fly

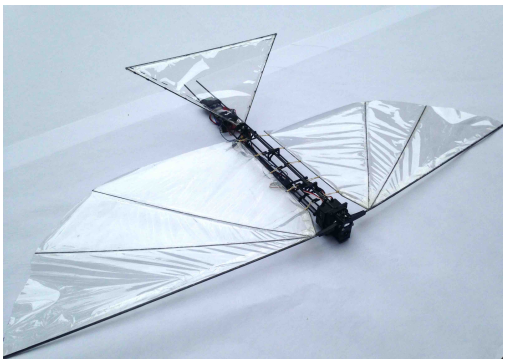

FIGURE 5.2: Robo Raven I Flapping Wing Vehicle

very flat or nose dive during flight. This remains true of all the purely flapping versions of Robo Raven and becomes more true when mass is added at the nose as is the case with integrated solar cells and batteries.

5.3.3.2 Passive Mass Effect on Propeller Assisted Flapping Wing Flight

Robo Raven V, came about as a means of increasing payload capacity and maneuverability via a propeller augmentation Holness et al. [2015]. Additional thrust via propellers allows for higher flight velocity which increases the payload via aerodynamic lift and platform agility by decreasing the demand for continuous flapping, allowing for greater utilization of independent wing control to rapidly change the flight vector and vehicle orientation. The findings of an investigative study Holness et al. [2018a] were that the coupling, most notably the wing wash going into the propellers, has minimal effects on performance. Flight tests proved viability of multi-modal flight including flapping with propellers, and fixed wing position airplane style flight. The flexibility of the wings allows them to passively balloon into an airfoil shape. Diving using dihedral to control dive rate is possible Roberts et al. [2015]. There are a number of advantages of flexible

membranes which provides performance with passive deformation with benefits not limited to flapping flight only Ifju et al. [2002], Mancini et al. [2015b], Platzer et al. [2008], Shyy et al. [2005].

The platform design of Robo Raven V builds on from Robo Raven I. Each wing is separately driven by a Futaba servo motor. The tail is operated as a rudder inclined such that it provides a static elevator functionality although an active elevator can be included Holness et al. [2015]. Two DYS BE1806 brushless motors rated at 2300 RPM/V are used to drive 12.7 cm diameter Gemfan propellers mounted at the rear of the platform. The left motor is rotated clockwise and the right is rotated counter clockwise to minimize torques created by the propellers. For the exploration of position effects and to prevent crash damage adjustable arm mounts are available to vary the propeller locations. Each propeller mounting arm is able to be actuated independently as are the propellers which provide maneuverability options. The system is powered by a 2 cell lithium polymer battery, with a nominal voltage of 7.4 V, 8.4 V when fully charged, however electrical requirements dictate usage of a larger volume and mass battery.

The inclusion of the propellers, mounting assemblies, and larger battery change the center of mass. During initial flight testing of Robo Raven V, in attempts to determine center of mass that would provide forward flight with reasonable trims of the controls, a battery was placed aft, following the precedent of the original Robo Raven platform. The result was a double back-flip into a sustained glide with RC input from a human operator into the open loop system. This maneuver can be seen in video at `https://youtu.be/Yryz8PSAwmA?t=1m26s` and is shown via frame captures of sequential (non consecutive) video frames in Fig. 5.3 with a schematic shown in Fig. 5.4. With an aft center of mass repeated back-flips having been demonstrated while flapping continuously as well as a high angle of attack gliding.

(a) 1- Start of back-flip

(b) 2- Approach of back-flip apex

(c) 3- Exit from apex

(d) 4- Exit from back-flip trajectory

(e) 5- Held hover after completing back-flip

(f) 6- Sustained held hover

FIGURE 5.3: Frame captures of sequential, non consecutive, video frames of propeller assisted flapping wing aerial vehicle performing a back-flip into a sustained hover

5.4 Design for Active Inertial Adjustment

As noted previously, movement of the battery has been used to modify the center of mass of a quadrotor Bouabdallah et al. [2006]. In similar fashion, the concept employed is to change the location of the battery to modify the location of the center of mass– multifunctionalizing the energy storage. The effectiveness of a translating reaction mass would be limited by the stroke of its linear guide Briggs et al. [2012]. The aim is to move the location of the battery as much as possible and use the mass of the actuator

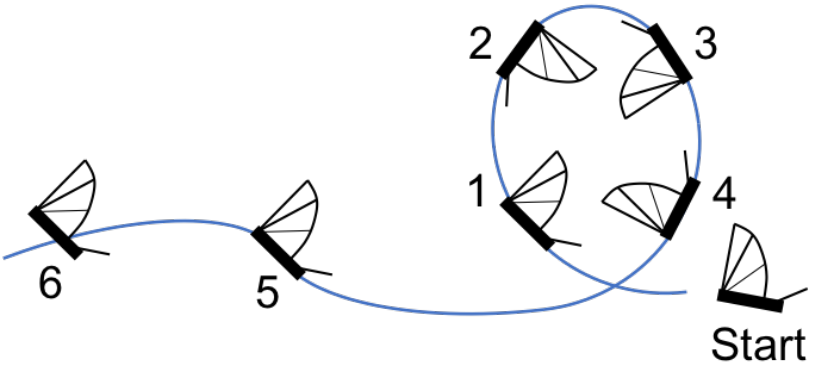

FIGURE 5.4: Pilot controlled flight trajectory of Robo Raven V with rearward center of mass (starting from position 1 going to position 10). A loop was completed starting with flapping (positions 1-2) and ending with fixed wing position and propeller control to complete the loop into a slow forward velocity, high angle of attack gliding style flight utilizing the propellers

in conjunction with the battery mass.

5.4.1 Platform Design

The core Robo Raven V, described in chapter 4, is maintained with minor updates. Each wing is separately driven by a 72 g Futaba S9353HV servo motor which is comparable to the Futaba S9352HV motor but has a full metal casing. The tail is operated as a rudder inclined such that it provides a static elevator functionality though an active elevator can be included Holness et al. [2015]. Two DYS BE1806 brushless motors rated at 2300 RPM/V are used to drive 12.7 cm diameter Gemfan propellers mounted at the rear of the platform. The propellers were changed to higher pitch propellers from Gemfan 5030 propellers to 5040 propellers. This change consumes additional power, however, it improves the thrust generation. The left motor is rotated clockwise and the right is rotated counter clockwise to minimize torques created by the propellers. The system is powered by a 2 cell lithium polymer battery, with a nominal voltage of 7.4 V, 8.4 V when fully charged. The control is provided by a Arduino Nano micro controller which processes control inputs provided by a Spektrum six channel receiver

TABLE 5.1: Linear actuator specifications

	Value	Unit
Mass	74	g
Max Speed (No Load)	32	mm/s
Stroke	100	mm
Max Force	50	N

FIGURE 5.5: 100 mm stroke RC compatible linear actuator

and sends independent signals to each actuator. To provide the movement of battery mass a 100 mm stroke, 74 gram Actunoix linear actuator for RC use was added, Fig. 5.5[1]. The actuator was mounted directly below the battery such that the pair can act as one reaction mass. The existing carbon fiber of the body was used as a linear slide guide. The actuator mounting can be seen in Fig. 5.6. Specifications for the actuator are shown in Tab. 5.1. The mass of the linear actuator is comparable to the main servos. As a result, the addition of the linear actuator changes the center of mass along the z-axis. To compensate, the propeller locations were lowered, taking advantage of the articulated propeller mounts. The propeller mounts were lowered to 2.4 cm below the platform center line. Based on previous findings Holness et al. [2018a], this change should not affect thrust generation.

Addition of the actuator will change the center of mass due to the additional mass it adds. As opposed to adjusting this position, bearing in mind that we will be able to tune the position, we can redefine the origin as follows:

[1]https://www.actuonix.com/L16-R-Miniature-Linear-Servo-For-RC-p/l16-r.htm

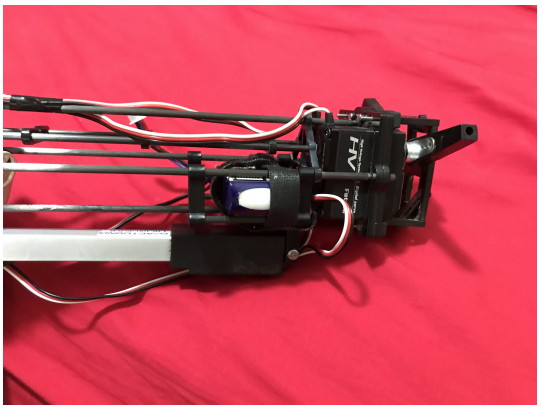

FIGURE 5.6: 100 mm stroke linear actuator with battery slider assembly

$$\frac{x_1 M_1 + x_2 M_2'}{M_1 + M_2'} = 0 \tag{5.19}$$

This is acceptable as long as the net change in position still provides a shorter distance relative to the lift. The mass can be moved by a unit, a, as before. The final result is the following:

$$\frac{a(M_2')}{M_1 + (M_2')} = c \tag{5.20}$$

Explicitly:

$$\frac{a(M_2 + m)}{M_1 + (M_2 + m)} = c \tag{5.21}$$

5.5 Thrust Generation Models

A flapping thrust model (Eq. 5.22) was developed and was shown to have good agreement with measured results (using the same testing methodology for this work) in previous work Holness et al. [2018a] as described in chapter 4. Fig. 5.7 shows experimental

data and the model. The model has to be corrected for losses of amplitude that result from the actuator loading using discretely measured amplitude values. The largest disagreement occurs at 4 Hz. In light of this, the experimental value will be used as all testing was conducted assuming 4 Hz flapping.

The flapping wing model for the thrust is the following:

$$F_{FT} = k_F f^2 S \Delta\alpha \tag{5.22}$$

where f is the flapping frequency in Hz and $\Delta\alpha$ is the flapping amplitude in radians. This is produced with insight gained from Platzer et al. [2008] which notes that thrust increases with frequency and amplitude of oscillation, work by Shyy et al. [1999, 2013], and a flapping advance ratio as follows Ho et al. [2003]:

$$J = \frac{V}{2\Delta\alpha f b} \tag{5.23}$$

where b is the wingspan.

The thrust from the propellers can be modeled by the following expression Anderson [2012], Brandt and Selig [2011], Brezina and Thomas [2013], Deters and Selig [2008], Silvestre et al. [2014]:

$$F_{PT} = C_T \rho \Omega^2 D^4 \tag{5.24}$$

Noting that the total thrust is the superposition of the two modes, the total thrust is:

$$F_T = k_F f^2 S \Delta\alpha + C_T \rho \Omega^2 D^4 \tag{5.25}$$

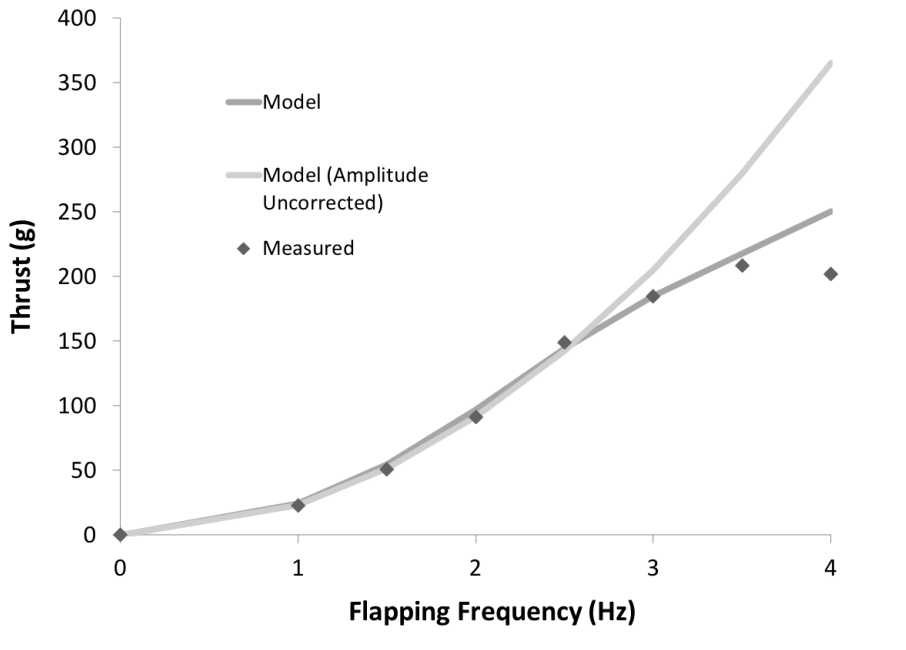

FIGURE 5.7: Average Measured And Modeled Thrust vs Flapping Frequency Showing Tapering of Thrust Production Due To Loss of Flapping Amplitude At Frequencies Above 2.5 Hz

Given the change in propellers, the model will be reevaluated against new experimental data for the new propellers.

5.6 Testing Methodology

In order to assess performance two Robo Raven V platforms were used. The first version was statically mounted to a test stand to determine the thrust due to the use of higher pitch propellers. The test stand is equipped with a American Digital optical encoder to record the wing flapping amplitude and ATI Mini40 six-axis force/torque transducer. Thrust measurements were recorded in 5 m/s (as measured by a pitot tube in previous work) of airflow generated by fan in a wind tunnel Gerdes et al. [2014]. The force transducer is capable of independently measuring all six components of force and torque using a Cartesian coordinate system and calibrated by ATI to measure up to 40 N in the

X and Y directions with a resolution of 1/100 N (1.02 g) of resolution and 120 N in the Z direction with a resolution of 1/50 N (2.04 g). The resonant frequency for Fx, Fy, and Fz measurements are 3200 Hz, which is far beyond the operating frequency. This test stand design was developed and utilized in previous flapping flight work Mueller et al. [2010] and has characterized Robo Raven in previous work Gerdes et al. [2014], Perez-Rosado et al. [2014, 2015a,b]. Similar approaches with load cells have been used in other flapping research work Rose and Fearing [2014]. It was adapted to test a propeller assisted Robo Raven V in previous work Holness et al. [2018a]. This setup can be seen in Fig. 5.8. This test stand allows for flapping at various frequencies, propeller positioning, and propeller speeds. In this work propellers were operated at various motor input signals from 20 % to 100 % in increments of 20 % while in 5 m/s airflow similar to Gerdes et al. [2013b]. The corresponding angular speed, Ω, in revolutions per minute per motor input signals was determined using a Extech 461920 laser tachometer. At least three trials were conducted for each force measurement including the baseline modes (flapping only and propellers only) and for each measured mixed mode condition. Six trials were conducted with the new propellers. The data was recorded using a LabView VI interfaced with a National Instruments data acquisition system after the static platform was mounted on the load cell. During operation, the data was gathered for 5 seconds at 1,000 samples per second. The actuators were started and stopped outside of each capture window to ensure well developed operation free of initial and final transients. These 5,000 samples were then averaged to provide the net thrust per trail. Tests were then repeated two more times. The average of three trials was then averaged to produce the final figure for thrust provided. To prevent skewed results due to motor heating, time for cooling was allowed between tests, particularly for the wing servos.

While load cell measurements provide insights into aerodynamic force production they

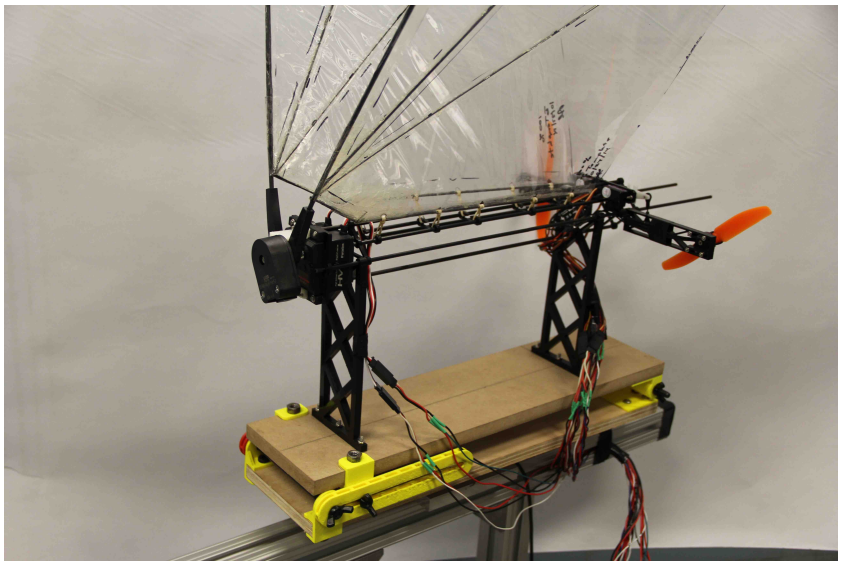

FIGURE 5.8: Test Stand

fail to be fully representative of in flight performance because the platform is unable to move. For this reason flight testing was critical to determine basic flight feasibility and payload. In addition to this statically mounted platform, a flight testing platform was created for this purpose. To verify flight feasibility, flight tests were conducted inside of the University of Maryland Fearless Flight Facility (F3), a netting enclosed flight outdoor space. Flights tests were conducted on days where the wind speed was below 2 knot (1.03 m/s) using a mAh LiPo battery for power. The platform was hand launched and allowed to reach steady flight using a flapping frequency of 4 Hz which pilot controllable propeller speeds. Rudder control was only utilized during the launch period and/ or to avoid obstacles. Sustainable flight was possible. In flight data was recorded and logged using a Razor inertial measurement unit (IMU) available from SparkFun electronics and logged onto a micro SD card using an Openlog data logger also from SparkFun electronics. The IMU provides data at 20 Hz. The logger recorded pitch, roll and yaw data in addition to three axis accelerometer. Video frames of the flight footage are shown in Fig. 5.11 with successive (non consecutive) frames going from top to bottom from left to right.

5.7 Results

5.7.1 Propeller Characterization

The propeller used in this work was changed to a 5040 Gemfan propeller which has a higher thrust output and pitch compared to the previously used 5030 propeller. The propeller performance was characterized. The highest thrust generated was 419 g. The thrust produced versus angular speed is shown in Fig. 5.9 as well as the previously characterized 5030 propellers with the model applied to the corresponding data series.

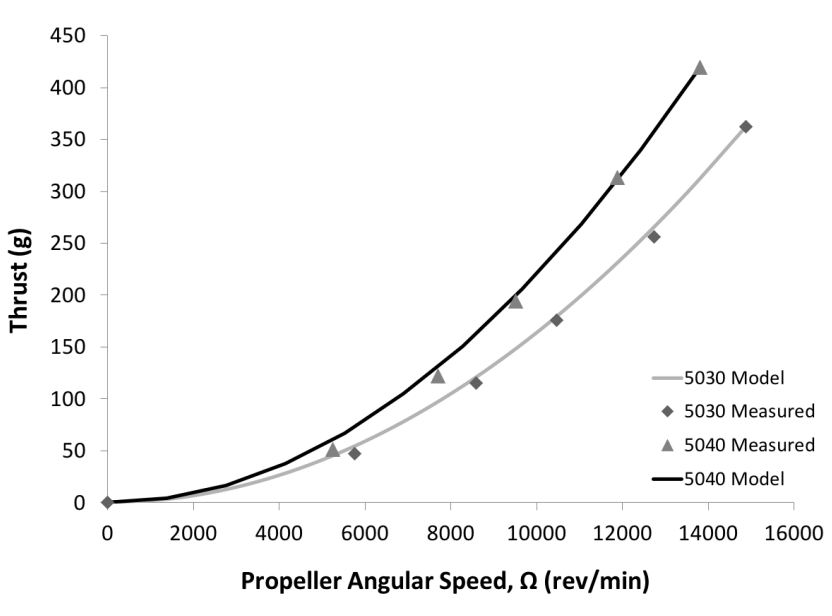

FIGURE 5.9: Thrust generated using 5040 and 5030 propellers with corresponding models

Similar to the work shown in chapter 4 this motor performance in the mixed mode case is assumed to be the superposition of the individual modes as shown in Eq. 5.26. The tested values were summed. The superposition has agreement with the measured data of the mixed mode performance as described in detail in chapter 4. The superposition of measured flapping and the measured propeller values for both 5030 and 5040 propellers

is shown in Fig. 5.10 Additionally, the measured mixed mode (both modes used together and measured together) thrust using 5030 propellers is also shown in Fig 5.10

$$k_F f^2 S\Delta\alpha + C_T \rho \Omega^2 D^4 - \Psi = \frac{1}{2}\rho V^2 S C_{D,p} \tag{5.26}$$

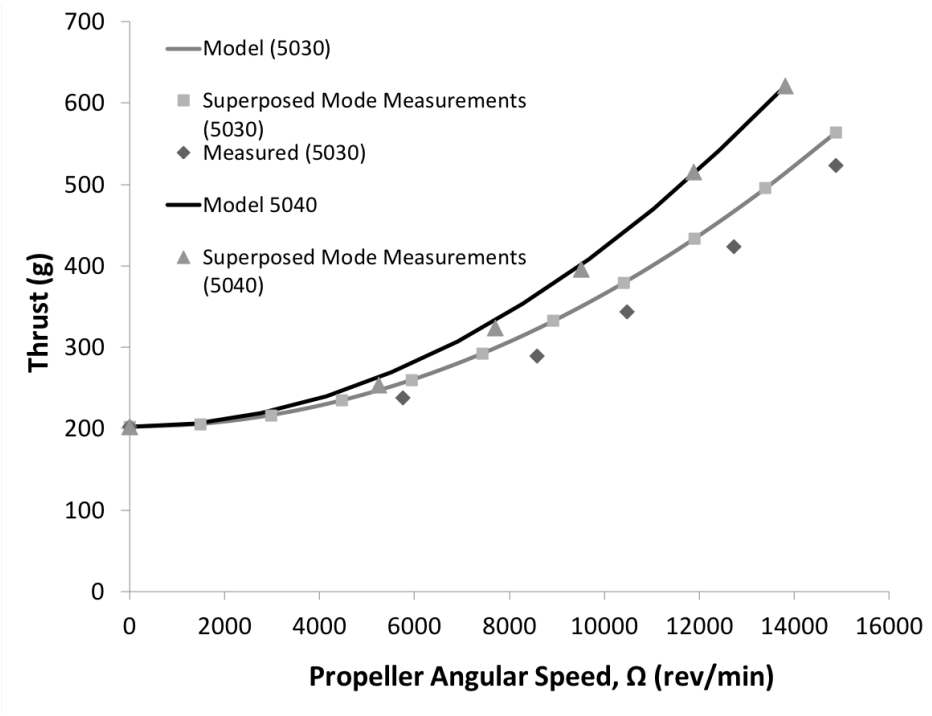

FIGURE 5.10: Mixed mode performance via superposition of 5040 and 5030 propeller thrust with 4 Ha flapping thrust in addition to measured mixed mode performance for 5030 propellers and flapping wings

5.7.2 Center of Mass Change

The entire platform mass was 625 grams. The linear actuator, the slider, and 850 mAh lipo battery assembly have a combined mass of 135 g. It is assumed that the entirety of this mass moves as a point mass and will function as the reaction mass. With the slider in the forward position, the leading edge of the wings was determined to be 17 cm from the center of mass. Based on the predictive model (Eq. 5.21) the center of mass should be able to move 2.1 cm. If this is the case, the leading edge of the wing should

be 19.1 cm from the center of mass when the reaction mass is in the rearward position. With the slider assembly in the rearward position, the measured length from the center of mass to the leading edge of the wings was determined to be 18.7 cm, 0.4 cm lower than the predicted value.

5.7.3 Flight Testing

Flight testing was conducted. The platform was hand launched and allowed to reach steady state flight. After steadying, the inertial control via the reaction mass was then used. In addition IMU data, video was captured. The pitch, roll and yaw were recorded. Additionally, acceleration along each axis relative to the body frame was recorded. Frame captures of the video footage are show in Fig 5.11. In order to assess the change horizontal acceleration rotation relative to the world frame, the following rotations were utilized using the data for roll Eq. 5.27 and pitch Eq. 5.1. The yaw rotation was not necessary as the interest is the acceleration relative to the flight path.

Roll rotation

$$R_x = \begin{bmatrix} 1 & 0 & 0 \\ 0 & \cos\phi & -\sin\phi \\ 0 & \sin\phi & \cos\phi \end{bmatrix} \tag{5.27}$$

In order to attain velocity, the acceleration data was numerically integrated. The IMU data shows multiple stages of the flight as shown in Fig. 5.12 and Fig. 5.13. First the platform is flapped while being held starting at roughly 5 sec. At 10 sec, it is thrown at high pitch to start the flight, which is indicated by large spikes in both forward and upward velocities in Figs. 5.12 5.13). After the initial launch the platform stalled and recovered from 10 sec to 13 seconds as shown by the high pitch peak and

(a) Steady flight

(b) Begin of inertial transition

(c) Held pitch

(d) Held pitch

FIGURE 5.11: Frame captures of sequential, non consecutive, video frames of propeller assisted flapping wing aerial vehicle using inertial control

decline in conjunction with the lower forward velocity and recovery of flight velocity (Fig. 5.12). After stall recover, normal flight can be seen between 13 and 16 seconds, gaining velocity. An image of the steady flight is shown in Fig. 5.11(a). Starting at 16 seconds the inertial control is implemented. The forward flight velocity starts to decline Fig. 5.12. Additionally, the pitch starts to increase as shown in the flight video frame shown in Fig. 5.11(a) and by the data shown in Fig. 5.12. The pitch eventually plateaus starting at 19 sec as the pitch is relatively fixed and as can be seen in the flight footage in Figs. 5.11(c) and 5.11(d). The highest pitch achieved in this region was 56.9 degrees. The platform then descends at 22 sec noted by a large increase in the forward velocity as seen in Fig. 5.12.

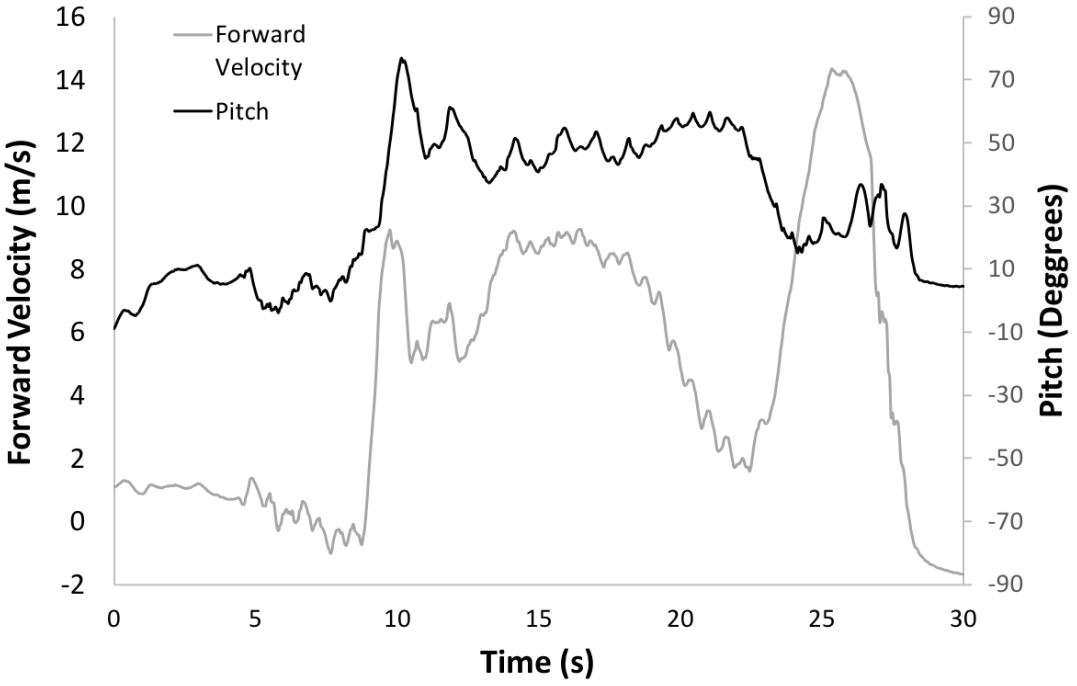

FIGURE 5.12: Pitch and forward flight velocity relative to heading

5.8 Discussion

Throughout the majority of the flight, the angle of attack is high $>25°$, using the data for airfoil lift coefficients provided by Anderson [2012] for context. At low angles of attack the relationship between angle of attack and lift is similar to a fixed wing airfoils and flapping wings, however at higher angles of attack the lift drops precipitously for fixed wings but this is not the case of flapping wings. Wing flexibility and flapping are favorable in such a way that higher angles of attack are possible. Stable leading edge vorticity persists through the flapping stroke and enhances mean aerodynamic forces Mancini et al. [2015b], Zhao et al. [2009]. Additionally, thrust vectoring allows for support of platform mass which has a high contribution in this case given a thrust to mass ratio of 0.99.

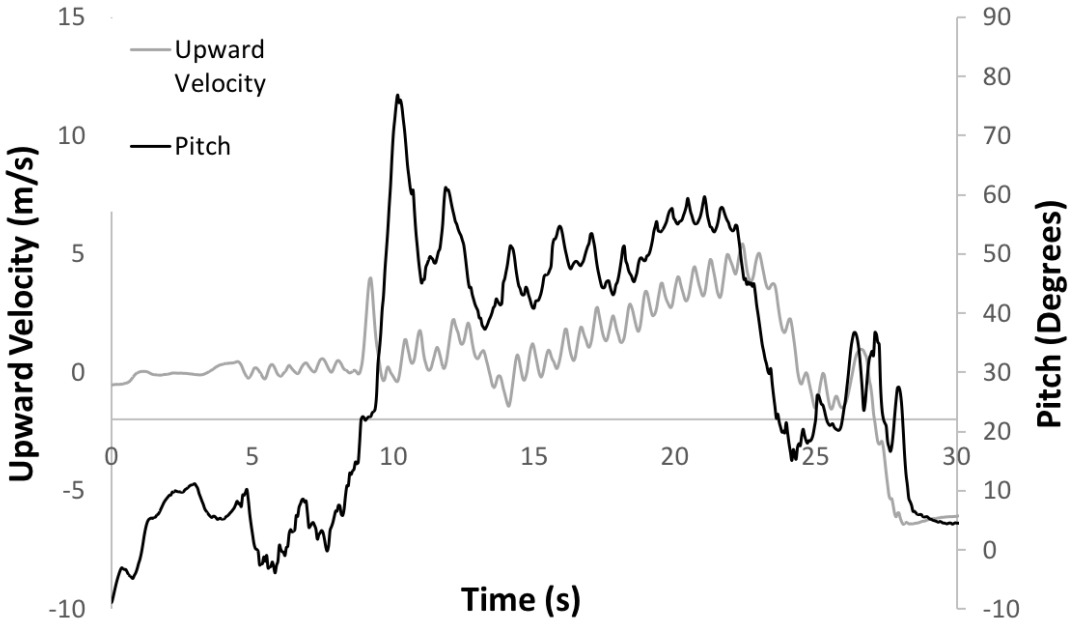

FIGURE 5.13: Pitch and upward flight velocity

5.9 Conclusion

In this work inertial control was demonstrated using a flapping wing aerial vehicle. A reaction mass system using a linear actuator in conjunction with the battery mass was used. An inertial measurement unit and video footage were used to verify that a reaction mass is able to change the center of mass such that angle of attack is increased and a rapid deceleration occurs. A basic modeling approach was presented to estimate the change in center of mass and a model was developed to describe the aerodynamic forces acting on the wing surfaces.

Chapter 6

Endurance Improvements via Multifunctional Wings with Energy Storage Media

6.1 Introduction

In Perez-Rosado et al. [2015a] flexible low efficiency solar cells were integrated into the wings in order to harvest solar energy to add additional energy to the system. This was done in order to increase flight endurance and provide the ability to charge batteries in field. Wing material, which is necessary for flight, was replaced with solar cells to provide both energy harvesting and structural functionality, which in turn provided mass economy by making it multifunctional. In order to do this, sections of the wings and tail membranes were cut out and replaced with solar cells. This integration paradigm is not the same as simply laminating the solar cells on top of the wings, as it is more economical in terms of weight by replacing wing mass with the solar cell material. The technical

challenge and contribution of the work was to work towards understanding how the integration of solar cells into the wings, tail, and body affects flight performance. It was demonstrated through the various versions of the solar cell integrated platform, Robo Raven III, that it is possible to integrate structures into the wings of a flapping wing vehicle while allowing flight despite changes in motor loading and wing deformation. The progression of research currently available in published literature develops integration of solar cells in the wings, tail and over the body (See Perez-Rosado et al. [2014, 2015a,b] for details). In order to provide additional area to accommodate solar cells and increase the payload, the wing sizing results from the Robo Raven II Gerdes et al. [2015] were used in this most recent work. Wings that are 66% larger in area were used. Given the low efficiency of the solar cells it was not feasible to provide the entirety of the power required to fly, meaning a battery is still necessary. Additionally, a batter is still needed in order to fly at night or under low light conditions.

6.1.1 Integrated Batteries to Increase Flight Time

In similar fashion to the solar cell work described by Perez-Rosado et al. [2014, 2015a,b], batteries can be integrated into the wings of the vehicle as a means of increasing flight endurance. Flexible thin film batteries have gained attention because they make it possible to electronically power a compliant or moving system. An additional advantage is the smaller form factor. A thin film battery generally consists of an anode and a cathode, separated by a separator film. In order to accomplish a transfer for the ions, the separator gets moisturized with an electrolyte. Different battery fabrication methods are known from research, including variations of evaporation, chemical vapor deposition, physical vapor deposition, microwave plasma enhanced chemical vapor deposition, sputtering, spray coating, plasma spraying, or vacuum depositing metals Kucherovsky

et al. [2002]. There has been a lot of attention on lithium ion batteries in research, due to their high energy density. Lithium polymer (LiPo) batteries are commonly used in the remote control (RC) community. In order to generate aerodynamic forces the wings should be able to deform. The issue with LiPos are the packaging mass and stiffness of the battery when complete. For a purely flapping vehicle wing deformation is important for aerodynamic force generation.

Flight time is a function of energy available and energy usage. The limitation to energy availability is the mass that can be accommodated. To predict the mass that can be accommodated, the quasi steady state assumption is used. Quasi steady-state wing theory assumes that the forces on a moving wing are equivalent to the sum of the forces on a fixed wing over a sequence of attitudes that track the wing motion. This model neglects acceleration forces and unsteady aerodynamic effects" Muijres et al. [2008]. Though the quasi steady state assumption is simplistic and does not always predict flapping flight performance, it is a helpful first order approximation and it is a common approach to use it Madangopal et al. [2004], Shyy et al. [2013]. Using the quasi-steady state assumption, for level flight where the acceleration is equal to zero, the maximum flight mass, M_{max}, must be equal to the total lift that can be generated.

The maximum flight mass, M_{Max}, occurs at the maximum total lift that can be generated.

$$F_{L,Max} = M_{Max}g \tag{6.1}$$

The payload, M_{pl}, is the difference between the base platform mass, M_{FWAV}, and the maximum flight mass, M_{Max}, as follows:

$$M_{pl} = M_{Max} - M_{FWAV} \tag{6.2}$$

The payload is the upper limit of the on board energy storage mass.

$$M_b \leq M_{pl} \tag{6.3}$$

Energy available, E_a, is a function of the battery mass, M_b, and its energy density, ξ, as follows:

$$E_a = \xi \cdot M_b \tag{6.4}$$

The flight time, t_f, assuming an averaged power draw, is the following:

$$t_f = \frac{E_a}{P} \tag{6.5}$$

where, P, is the average power

If the entirety of the payload is occupied with battery mass, $M_b = M_{pl}$. The flight time before landing then becomes:

$$t_f = \frac{((F_L/g) - M_{FWAV}) \cdot \xi}{P} \tag{6.6}$$

The upper limit of the on board energy source mass is limited by the amount of mass that can be carried (i.e., the payload capacity).

Means of increasing flight endurance increase the payload which increases the mass that can be carried or increases the energy density such that there is more energy without increasing mass proportionally.

6.2 Increasing Endurance By Increasing Battery Mass Alone

The challenge of flapping wing flight is the lift limited mass. The development of a multi-modal, propeller assisted flapping wing vehicle is one means of increasing lift such that the wing size does not need to change Holness et al. [2018a]. The trade-off is that the platform complexity increases as does the power requirements to power the platform, though it can be favorable. Another strategy is to scale up the wings to increase the payload Gerdes et al. [2015] as was used low efficiency solar cells implementation Perez-Rosado et al. [2015a]. In similar fashion, integration batteries in the wings are being explored to multifunctionalize the wings and reduce parasitic mass. A 30 g 550 mAh flexible LiPo battery was identified. This battery is semi flexible as it should only be flexed in one direction. Designed for prosthesis, its price is prohibitive as they are more than 32 times the cost as the current batteries used (seen in Fig. 6.1[1]) and it has over current preventing safety circuitry. The advantage of using a LiPo chemistry is that the power availability of the battery is high, assuming there are no current limiting safeguards in place, and well known in the use case as it is currently the battery chemistry used. A notable mode of failure for lithium polymer (LiPo) batteries is that fact that it is a fire risk if the cell is damaged. A higher energy density battery is more favorable assuming that it is able to deliver the required power requirements.

[1] http://www.hobbyking.com/hobbyking/store/catalog/N370-2S-25(1).jpg

FIGURE 6.1: Currently used LiPo battery

6.3 Increasing Endurance By Varying Energy Density

While increasing payload to increase battery mass without changing battery chemistry is one means of increasing endurance, a potentially better alternative is to use high energy density batteries. In this case both more mass can be carried and the energy available per unit mass will be higher. To this end, a flexible, high density, ultrathin galvanic cell design was identified Peckerar et al. [2011a]. This technology is appealing given the specific charge capacity, the ability to recharge the battery, and lower safety risk because it is non toxic and environmentally friendly. During a flapping cycle, the deformation is very high and occurs rapidly. If a cell is damaged, the risks of injury are low. As noted previously, a mode of failure for lithium polymer (LiPo) batteries is igniting, if the cells are damaged. This is not the case with this Galvanic cell chemistry. A Galvanic cell can provide specific charge capacity 84.4 mAh per cm^2 depending on the composition and electrode thicknesses Peckerar et al. [2011a]. Cells of this type are anode-material limited in their performance. That is, the total charge delivered to the load depends on the number of atoms present in the anode material, in this case, Zinc. A 1 cm^2 square of zinc 0.01 cm thick contains 6.58 x 10^{20} atoms. As each atom in the reaction given in Eqn. 6.8 supplies 2 electrons, this converts to 213 Coulombs of deliverable charge. If this is delivered in an hour, the capacity of the cell would be close to 60 mAh/cm^2. The

FIGURE 6.2: Battery Cathode

FIGURE 6.3: Battery Schematic

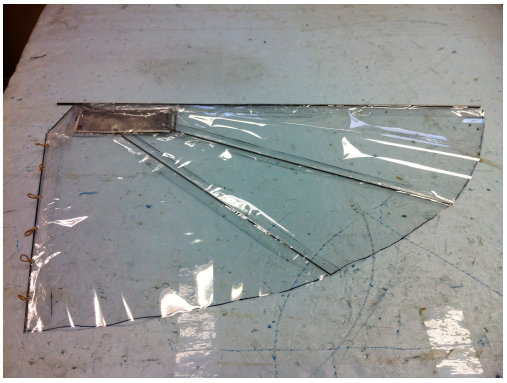

FIGURE 6.4: Wing With Battery Integrated

zinc foil of this thickness would weigh 0.07 g/cm^2. If more capacity is needed, we can easily thicken the foil and still be within the weight requirements of the Robo Raven. As shown in Peckerar et al. [2011b], thinner foils have provided about 10 mAh/cm^2 of capacity.

The reactions are the following:

FIGURE 6.5: Battery Mechanical Sample

Anode:

$$\mathrm{Zn} \rightarrow \mathrm{Zn}^{2+} + 2\mathrm{e}^{-} \tag{6.7}$$

Cathode:

$$2\mathrm{MnO}_2 + 2\mathrm{H}_2\mathrm{O} + 2\mathrm{e}^{-} \rightarrow 2\mathrm{MnO(OH)} + 2\mathrm{OH}^{-} \tag{6.8}$$

Several fabrication steps are required in order to make this battery. First, the cathode is made my mixing carbon black powder, a binder, and MnO_2 to create a dough mixture (Fig. 6.2). The initial mixing ratios were based on the details provided in Kucherovsky et al. [2002]. This mixture is then pressed flat on to a layer of high purity, Nickle foil. Next, a separator, which is wet with electrolyte solution with a pH of 6.0, is laid on top of the cathode. After this a sheet of Zinc is placed on top of the separator. This is as a cathode and Zinc as an anode. From the bottom up, the stack is Nickle, cathode, whetted separator, and, finally, Zinc as seen in the schematic in Fig. 6.3. This entire assembled stack is then pressed together. The pressed stack is then sealed. The size of the batteries is 14.25 cm by 5.2 cm and was selected based on the size of candidate solar cells for continuing research of the Robo Raven III goals. For fully functional electrical samples, the sealed cells have tabs from the current collector and the anode to allow electrical connections to be made. For purely mechanical samples, the entire stack was sealed.

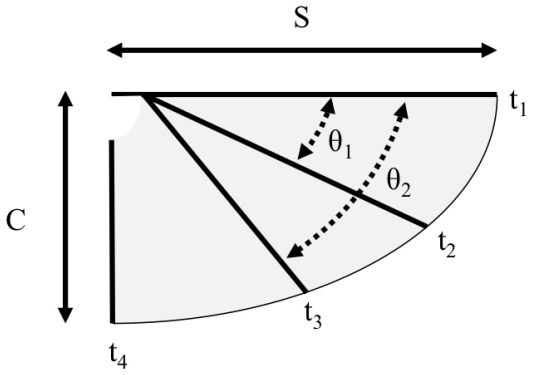

FIGURE 6.6: Robo Raven Wing Template

In order to compare the performance of different anode metals for flexible thin film batteries, specifically the relationship between the bending stiffness and electrical performance, the following multifunctional performance index energy density, U/A, is utilized:

$$\frac{U}{A} \cdot (\frac{M}{\kappa})^{-1/3} = \frac{nN_A V \rho e^-}{2 \cdot A_W \cdot E^{1/3}} \tag{6.9}$$

where n is the number of electrons that are released in the reaction, E is the stiffness of the anode, ρ is the anode density, e^- is the charge of a single electron, V is the voltage, $\frac{M}{\kappa}$ is the bending stiffness, N_A is Avogadro's number, and A_W is the atomic weight of the anode metal. This figure of merit is developed using the Euler-Bernoulli beam equation for a constant bending moment.

A comparison of Li and Zn anode metals can be seen in Tab. 6.1. It can be seen that Li is about 2.3 times greater energy storage for the same mass and bending stiffness. However, Zn is more stable to work with for these applications, and does not require the same type of packaging that compromises the stiffness benefits of Li. This is evident later on when the LiPo and the ultrathin galvanic cell battery are compared in Tab. 6.3

TABLE 6.1: Anode metal comparison

	Li	Zn	Ti
Voltage (V)	3.7	1.5	2.5
Number of Valence Electrons	1	2	4
Density, ρ (g/cm^3)	0.53	7.41	4.43
Stiffness, E (GPa)	4.9	108	110
Atomic Weight, A_W (g/mol)	6.9	65.4	47.9
Performance Index (MJ/N$^{1/3}$ m$^{7/3}$)	8.07	3.44	9.31

6.4 Design Process and Considerations for Battery Integrated Wings

6.4.1 Mass Analog Batteries

The difficulties of doing a design iteration is that it is cost prohibitive. As a means of testing designs and validating results, an mass analog of the battery was created. This battery was created with means compatible with layer jamming. Layer jamming allows the stiffness of a material to be increased if pulled under vacuum. Using a layer jamming assembly process allows for tune-able stiffness which can allow for simulation of numerous materials, though it is beyond the scope of this work. Using mass analog allows information into the mass effects on the motors including amplitude changes and power draw. A wing with a paper jamming structure was created (shown in Fig. 6.7) using the same multifunctional fabrication process that will be described later. Given the larger mass of the flexible LiPo battery, it was selected to be the mass used for the analog.

FIGURE 6.7: Wing with analog battery mass compatible with layer jamming Lothar

6.4.2 Battery Integration Location

This particular membrane wing design requires deformation in order to produce produce aerodynamic forces via a blow-back of air. Visual inspection of high speed video footage reveals the large deformations achieved, specifically on the trailing edge of the wing between spars t_3 and t_4 in the wing schematic (Fig. 6.6). Studies that were conducted in the development of the solar cell integrated version of Robo Raven, Robo Raven III, show that replacing the thin Mylar film with a stiffer media in this area decreases the deformation which in turn adversely affects aerodynamic force generation (See Perez-Rosado et al. [2014, 2015a,b] for details). The deformation change was quantified through force measurements and digital image correlation of the flapping wings. In light of these findings, the batteries, which are stiffer than the Mylar film were integrated close to the leading edge of the wing. Secondly, the mass of the batteries influenced battery placement. It is favorable to integrate the batteries as close to the motor to reduce moment arm. If the batteries were mounted far away from the axis of rotation for the motor, the loading of the motor would be significantly higher given the moment of

inertia. In addition the structure loading on the carbon fiber supporting the wing would be higher.

If moment of inertia is modeled as a point mass the moment of inertia is the following:

$$I = M_B l^2 \tag{6.10}$$

If the batteries are placed far away from the motor, it is expected that the amount of power required to flapping would increase. The trend should increase with both flapping frequency and location away from the motor.

6.4.2.1 Multifunctional Wing Fabrication Process

A lamination process is employed to make the multifunctional wing. Notably, this process is the the lamination of cut layers, meaning that internal layers in terms of the stacked structure, are exposed. The final, outermost, surface is formed from an inner layer, the batteries, and another layer composed of Mylar, the regular wing material. As noted previously, this is in sharp contrast to simply gluing the batteries on top of the surface of the wing. The batteries are load bearing and integral to generating aerodynamic forces.

Layers are cut and stacked on top of each other in order to a create fully completed wing. First, the template of the wings is draw on mylar (Fig 6.8(a)). Then, the dimensions of the batteries are measured. These dimensions are reduced on all sides by two centimeters. This results in an area slightly smaller than the area of the battery of the same geometry. This area is then drawn on the Mylar (Fig 6.8(b)). This area is then cut out of a thin membrane of Mylar as shown in Fig. 6.8(c). This process creates a boarder overlapping

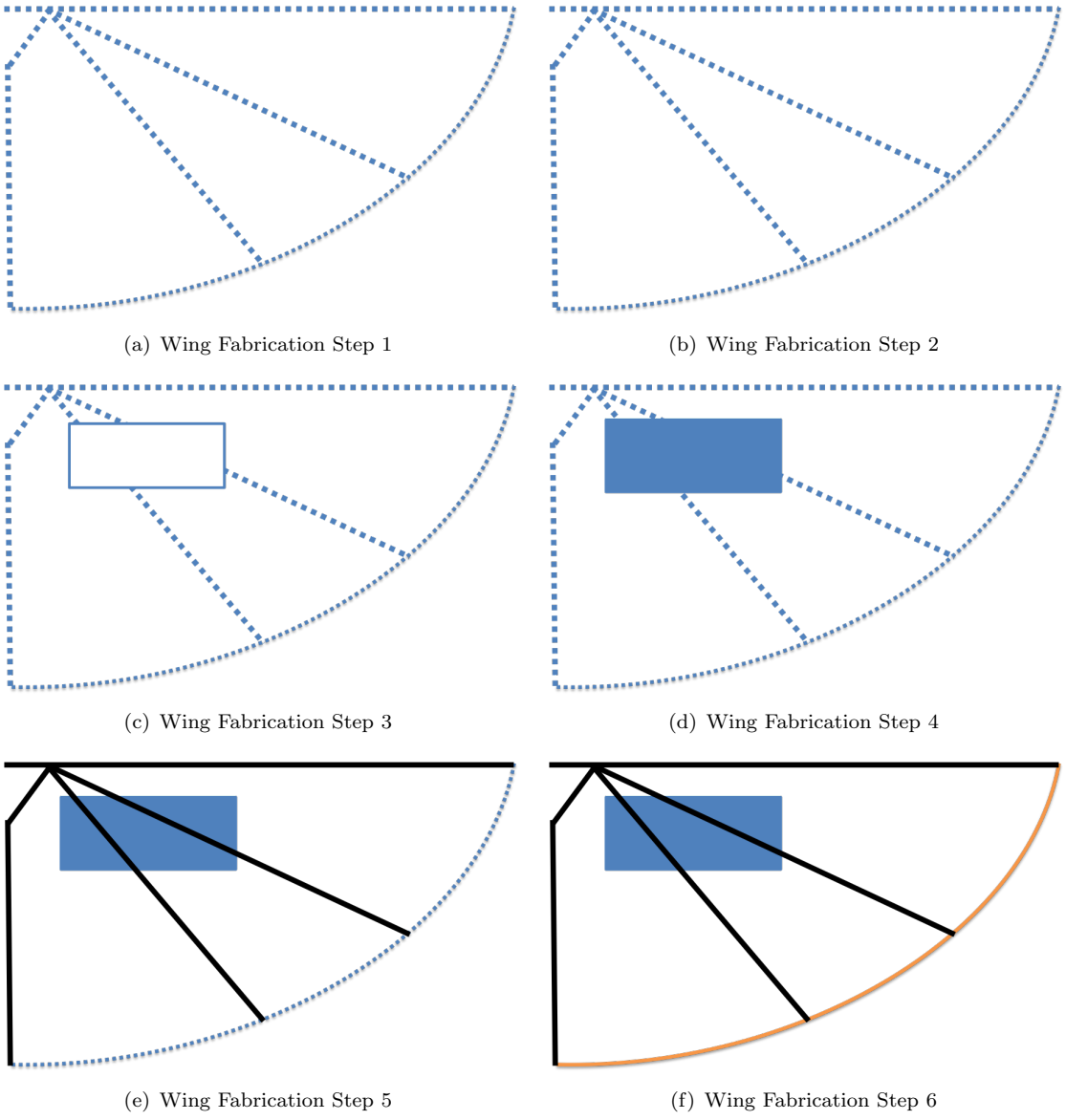

(a) Wing Fabrication Step 1

(b) Wing Fabrication Step 2

(c) Wing Fabrication Step 3

(d) Wing Fabrication Step 4

(e) Wing Fabrication Step 5

(f) Wing Fabrication Step 6

FIGURE 6.8: Multifunctional Wing Fabrication Steps

material to adhere the batteries to. In the next step, the batteries are adhered to the wing surface. In order to do this, adhesive is applied to coat the boarder of the Mylar film. The batteries, which are slightly larger than the hole, are then placed such that the 1 cm overlap is allowed on all sides as denoted by the blue section in Fig. 6.8(d). After this integration, the top portion of the wing will be composed of largely Mylar and the surface of the battery. In the fifth step, the spars are placed and encapsulated as shown in 6.8(e) (the spars are shown in black). Finally, in the sixth step, the back edge of the wing is cut free, which is shown with the orange line in Fig. 6.8(f). A completed

wing is shown in Fig. 6.4 The final platform is shown in Fig. 6.11

6.5 Testing Methodology

To assess the effects of battery position prior to scaling the wing, analog batteries were placed along the leading edge but at three different distances from the axis of rotation. These locations are given in Tab. 6.2. The wings tested would be the original Robo Raven wings. If successful, they would be tested on the larger scale wings.

TABLE 6.2: Battery positions measured from the axis of rotation

	M_B (g)	Distance (cm)
Bat. Pos 1	30	13.5
Bat. Pos 2	30	30.5
Bat. Pos 3	30	47.5

The wings were mounted to a test stand equipped with an American Digital E5 optical encoder to record the wing flapping amplitude and an ATI Mini40 six-axis transducer to record forces and moments. Measurements were recorded at 5 m/s air speed (as measured by a pitot tube) in a wind tunnel, which is similar to the air speed experienced during flight Gerdes et al. [2014]. The force transducer is capable of independently measuring all six components of force and torque using a Cartesian coordinate system and was calibrated by ATI to measure up to 40 N in the X and Y directions with a resolution of 1/100 N (1.02 g) of resolution and 120 N in the Z direction with a resolution of 1/50 N (2.04 g). The test stand also records the current draw of a servo via an NI 9227 current measurement car, as well ase the voltage such that the power draw can be determined. This test stand design was developed and utilized in previous flapping flight work Mueller et al. [2010], and has been used to characterize Robo Raven in previous

work Gerdes et al. [2014], Perez-Rosado et al. [2014, 2015a,b]. Similar approaches with load cells have been used in other flapping research work Rose and Fearing [2014].

To verify flight feasibility, flight tests were conducted on days where the wind speed was below 2 knot (1.03 m/s) using a mAh LiPo battery for power. The platform was hand launched and allowed to reach steady flight. Rudder control was only utilized during the launch period and/or to avoid obstacles.

6.6 Results

6.6.1 Location Effects on Power and Flapping Amplitude using Mass Analog

To asses the effect of location on power draw and flapping amplitude the mass analog batteries were located at the locations away from the axis of rotation. Flapping testing was conducted using the test stand described previously. The wings tested were the original Robo Raven wing design prior to scaling. The power to flap increases as the distance increases as shown by the increase in power in the series from positions 1, with distances shown in Tab. 6.2, to position 3 as shown in Fig. 6.9. The power also increases as a function of flapping frequency, consistent with previously reported findings. The amplitude of flapping also reduces as the distance from the axis of rotation increases as shown in Fig. 6.10. What is notable is that the carbon fiber spar of the wing broke when flapping at 3 Hz due to the additional mass of the battery analog. Given this evidence it is important to integrate the batteries close to the axis of rotation.

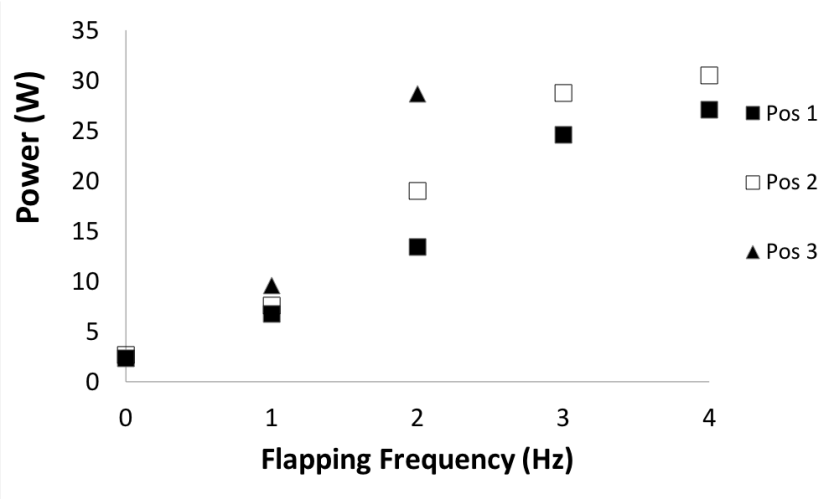

FIGURE 6.9: Power to flap at different flapping frequencies for different battery positions. Note: the carbon fiber spar broke during test of battery position 3 when flapped at 3 Hz

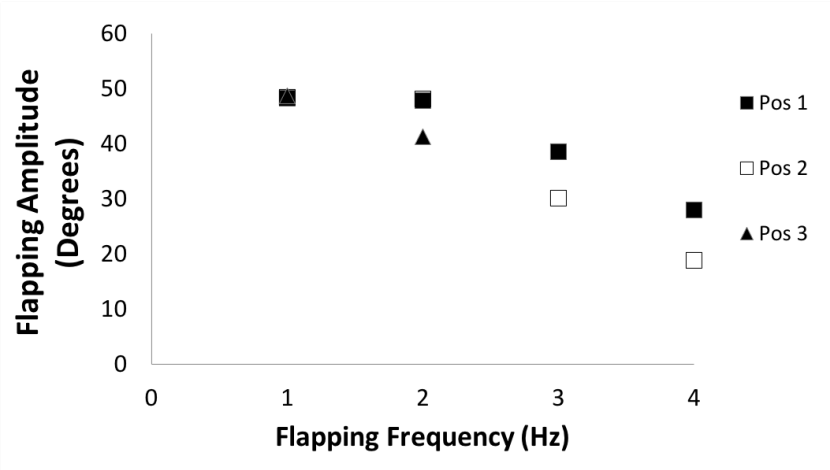

FIGURE 6.10: Flapping amplitudes at different flapping frequencies for different battery positions. Note: the carbon fiber spar broke during test of battery position 3 when flapped at 3 Hz

6.6.2 Thin Film Galvanic Battery Results

In light of the battery location discussion and findings, the batteries were located close to the center of the platform and close to the leading edge as seen schematically in Fig. 6.8(f) and the fabricated wing shown in Fig. 6.4.

In order to determine if it was worthwhile change, the energy density of the existing 370

FIGURE 6.11: Robo Raven VI

mAh LiPo battery was compared to that of the theoretical thin film battery. The performance values expected from zinc anodes were used to calculate the energy available. The value was then divided by the mass of fabricated batteries. As expected, the thin film battery offers a higher amount of energy per unit mass compared to the lithium polymer chemistry. The fabricated batteries produced 1.24 V each before they were fully enclosed for mechanical testing. Subsequent electrical samples produce voltages of 1.5 as our fabrication process was refined. Comparisons of the new batteries, the previously used NanoTech 370 mAh lithium polymer (Fig. 6.1) and the ultrathin galvanic cell batteries (6.5), are presented in Tab. 6.3.

TABLE 6.3: Battery comparison

Electrical Specification	370 mAh LiPo	Ultrathin Galvanic Cell Battery*
Energy (KJ)	11.18	20.64
Weight (g)	27	12
Voltage (V)	8.4	1.5
β (J/g)	414	1720

*12.25 cm by 5.2 cm area

6.6.3 Flight Tests

Flight tests were conducted to assess if the platform with battery integrated wings would be flight capable despite the inclusions of batteries. In order to do so, mechanical samples were integrated into the wings and flown. In order to quantify the mechanical changes of wings only the platform was powered from a lithium polymer battery as it is traditionally. If there was a large, detrimental, change in performance as a result of modified deformation, flight would not be possible. Despite the inclusion of the thin battery, flight was still possible, the flight weights were similar, and, qualitatively, the flights were similar based on visual inspection. Total flight weight results measured from the flight tests can be seen in Tab. 6.4.

TABLE 6.4: Flight test results

Wing Type	Platform Weight (g)	Measured Total Flight Weight (g)
Regular Wing	305.0	379.5
Battery Wing	316.8	384.5

6.6.4 Flight Time Improvement

The flight time given Eq. 6.6 is a function of the payload, which is the difference between the maximum lift, platform weight, and the energy density. The higher density batteries should improve the flight time because they have a higher value of β (as shown in Tab. 6.3). Using the flight test results in Tab. 6.4, it was possible to predict the change in flight time if the payload capacity is used to integrate batteries into the wings. Given that the platform mass with regular wings was 305 g, the subsequent payload capacity using the multifunctional battery wings would be 79.5 g. Now, assuming the power

consumption remains to be 36 Watts and that adding the additional weight to the wings continues not to affect the total flight weight, the subsequent flight time is 63.3 min.

In the case of the lithium polymer battery with the scaled mylar wings, the payload is 74.5 grams. For the wing area of this platform, which is approximately 5250 cm^2, the resulting battery coverage would be only 7.5%. Based on the energy density of the lithium polymer battery, if the entire payload is occupied with this type of battery, the flight time is 14.3 min.

While it is unlikely the performance will not degrade with additional batteries integrated into the wings, the large difference between the two indicates that even an intermediate condition for the multifunctional battery wings will yield substantially better performance than using a lithium polymer battery alone.

6.7 Conclusions

As a means of trying to improve flight endurance, the wings of Robo Raven, an independent wing controlled flapping wing air vehicle, were modified. High energy density, flexible, thin film batteries were fabricated and integrated into the wings. Calculations show that these batteries are in fact higher capacity per unit mass, thus improving available energy and flight time as a result. Functional batteries were fabricated and tested yielding the expected electrical performance. In order to access performance impact, mechanically, flight tests were performed. Despite the inclusions of the thin film batteries, the aerodynamic forces were not significantly affected and the vehicle was able to maintain flight upon flight testing. From the experimental results and battery models, the flight time is expected to improve by a factor of 3.4 when all of the payload capacity is used to integrate the ultrathin galvanic cell batteries into the wings of Robo Raven.

TABLE 6.5: Servo specifications

Voltage	Torque
6.6V	19.6 kg cm (272 oz-in)
7.4V	22.0 kg cm (305 oz-in)

Voltage	Speed
6.6V	0.07sec/60 deg
7.4V	0.06sec/60 deg

*Power Supply: 6.0-7.4V

In the immediate future, the goal is to be able to completely power the platform using thin film batteries alone while being able to characterize the performance changes for force generation and flight endurance. The voltage of the thin film batteries is lower than the lithium polymer chemistry currently employed. As a result, the integrated batteries are not yet powering the platform. While it is appealing for remote charging applications, it is a problem for operation of the platform because the performance of the main drive servos is a function of the voltage. Both the torque and speed improve at higher voltages which is why it is favorable to operate at higher voltage (See Tab. 6.5). A lower voltage would yield different performance from the main drive motors. Future work will address these difficulties. In light of this, a flexible LiPo alternative is a more straightforward replacement, however they do not provide similar performance gains. Regardless, these findings do inform inclusion of flexible materials whether it be batteries, solar cells, film super capacitors or sensors.

Chapter 7

Integrating High Efficiency Solar Cells in Flapping Wing Air Vehicles

7.1 Introduction

Avian systems can generate and control airflow mechanics Jones and Babinsky [2010], Muijres et al. [2008], Shyy et al. [2013], Zhao et al. [2009] to achieve impressive aerodynamic performance though various wing motions (variations in anhedral, dihedral, planform, camber, aspect ratio) and body motions Jones and Babinsky [2010], Pines and Bohorquez [2006], Rayner [1988], Shyy et al. [1999, 2013], Thomas [1996, 1993], Tobalske [2007], Usherwood et al. [2003], Wu et al. [2010]. There are also numerous examples of mammalian flight Muijres et al. [2008], Swartz et al. [2012], and at smaller scales with insect flight Ellington [1984a,b,c], Tarascio et al. [2005]. A number of bio-inspired flapping wing air vehicles (FWAVs) have been developed in pursuit of desirable

flight characteristics, including research platforms exploring warping wing flight and University of Maryland's Robo Raven series De Clercq et al. [2009], Festo [2016], Gerdes et al. [2013b, 2014, 2015], Hamamoto et al. [2010], Park et al. [2012], Perez-Rosado et al. [2014, 2015b], Roberts et al. [2014, 2015, 2016], Solutions [2016], Teoh et al. [2012], Wu et al. [2010]. As a means of reducing system complexity and weight, many successful flapping wing platforms rely on a single actuator Doman et al. [2011], Rosen et al. [2016], Shkarayev et al. [2010] to drive one degree of freedom while other degrees of freedom are generated using passive means to achieve complex kinematics Bejgerowski et al. [2010], Gerdes [2010], Gerdes et al. [2012], Madangopal et al. [2004], Platzer et al. [2008], Ramezani et al. [2017], Rosen et al. [2016], Swartz et al. [2012], Teoh et al. [2012], Wu et al. [2010]. One such approach is the usage of flexible membranes mylar, latex, or fabric which passively deform and are lightweight Mancini et al. [2015b], Platzer et al. [2008], Ramezani et al. [2017]. Usage and benefits of flexible membranes are not limited to just flapping wing flight Ifju et al. [2002], Shyy et al. [2005].

A key constraint with FWAVs is their lift-limited weight, which is dependent on coupling between the actuators and deformations of the wings. Due to these limitations, the energy source used to power the vehicle–often a battery for electrical systems–must remain low mass which limits energy availability and provides shorter flight times as a result. Shorter flights restrict the overall mission capabilities for any unmanned air system (UAS) and is highly undesirable for pursuing autonomous applications in particular.

If UAS platforms can harvest energy while in flight, such as capturing energy via vibrations Anton and Inman [2008], they can potentially have longer flight times. Extending this concept, energy sources outside of the platforms, such as solar power, have been explored to harvest energy while in flight, as well as on the ground in order to recharge batteries Perez-Rosado et al. [2015c]. If power requirements for flight are either met

or exceeded, then endless flight time should be possible, assuming there are no other hardware restrictions. There are already a number of examples of the usage of energy harvesting and storage in fixed wing aircraft systems in the research community Anton and Inman [2008], D'Sa et al. [2016], Scheiman et al. [2016], Shiau et al. [2009], Thomas et al. [2002], Thomas and Qidwai [2005], including harvesting of vibrational energy, harvesting solar energy and integration of battery systems into the wing designs of unmanned systems. There are a number of commercial and government agency platforms which use solar cells to gather solar energy and company initiatives to utilize solar energy to provide longer flight times. These include but are not limited to Solar Impulse I and II, Facebook's UAS based Internet platform, National Aeronautics and Space Administration's (NASA) Pathfinder and AeroVironments Helios aircraft, and Boeings SolarEagle Bronz et al. [2009], DeGarmo [2004], Engblom [2012], Noth et al. [2008]. The advantages of these systems is to provide station keeping Engblom [2012] and to reduce environmental impact DeGarmo [2004].

Gathering solar energy via photovoltaics can be more efficient then other energy harvesting technologies, if they are used in conjunction with optimized energy transfer techniques, such as maximum power point tracking (MPPT) Shiau et al. [2009], Hohm and Ropp [2003]. For example, it has been noted in Shiau et al. [2009] that using incremental conductance algorithm, as reported by Hohm and Ropp [2003], enable MMPT technologies to exceed 97% efficiency. Additionally, flight endurance can also be increased by using energy consumption reducing techniques, such as utilizing thermal updrafts in flight, which is the aim of the Navel Research Lab's ALOFT glider algorithm Edwards [2015] or AutoSoar Depenbusch et al. [2018]. Notably, amongst the research work considering solar cell integration, Zhang and Hu [2016] considers integration of solar cells into flapping wing platforms, specifically the effects of scaling on the performance of the

platforms. The scaling effects were studied using a power generation model for flapping wings where the incident solar flux was assumed to be perpendicular to the surface of the wing.

In this project, a general framework is developed to design and assess using solars to realize multifunctional wings for FWAVS that can harvest energy from nonplanar body poses where the wings are not perpendicular to the incident flux, which is inherent to flapping and to the desired flight path. A design case is presented using the University of Maryland's *Robo Raven* platform considering integration of high efficiency (HE) Gallium Arsenide (GaAs) solar cells into the wings, body, and tail. The effects of the solar cell integration on the aerodynamic performance of the FWAV are characterized on a test stand in a wind tunnel and in flight, while models are developed and used to understand the effects on the potential payload capacity and subsequent flight time. The electrical performance is also characterized to confirm the energy harvesting capabilities. Taking into consideration the potential powertrain effects on the power requirements for flight, the framework is used to predict the ability to achieve flight using batteries to provide energy only for power spikes and for additional time to achieve a safe landing when the sun sets.

7.2 Multifunctional Wing Design Framework

7.2.1 Overview

Fulfilling the power requirements of an aerial vehicle is important, because if inadequate power is provided (be it a power loss or fluctuation), a resulting loss of control risks harm to both the vehicle and anything below it. A vehicle that is dependent on harvesting

energy for flight should be designed to tolerate power fluctuations due to changes in the amount of incident solar flux received or due to surges in the electrical system. Aerial vehicles will also execute various headings and altitude changes relative to the sun to achieve a desired flight path, which affects power generation. For example, a high pitch may be required to climb to altitude, or a roll maneuver is executed in order to turn. These maneuvers will subsequently affect the energy harvesting performance of solar cells integrated into flapping wings, because the solar cells move relative to the body while the body itself changes relative to the incident solar flux. From a platform design perspective, determining the number solar cells required to provide system power is of utmost importance, so all of these factors need to be taken into account in designing components with integrated solar cells.

Flapping wing flight is also unique for UAS platforms in that control, lift and thrust force generation are coupled to the deformation of the wings, which are in turn coupled together or individually to an actuator. Given system weight, actuator restrictions, and current understanding of how to design for flapping wing flight aerodynamics, identifying a functional wing design, particularly with integrated solar cells, can be difficult. While successful airflow characteristics may be identified, achieving these characteristics is less straightforward. In light of this, identifying a functional wing design is often a trial and error process. Consequently, when a successful wing is identified it is often favorable to make small variations in order to maintain performance. Given the reliance on deformation, stiffness and location of stiffness must be considered (though many modeling approaches for flapping wings assume homogeneous properties in the wings because of the high complexity of modeling aeroelastic effects). Thicker solar cell materials which have a higher bending stiffness, potentially reduce deformation and the subsequent lift and thrust generation. Higher mass solar cell materials will also affect

the weight contribution of the wings to the total mass and the loading on the actuators, which potentially alters wing velocities and the subsequent lift and thrust generation as well.

As part of the design process for integrating solar cells into FWAV wings, the following topics are considered.

1. The solar energy harvesting is modeled to predict the energy generation considering various attitudes achievable by a flapping wing aerial vehicle, as well as the effects of flapping on orientation relative to the incident solar flux.

2. The number of solar cells required to meet operational power requirements is determined by considering candidate solar cell technologies and accounting for sensitives to the orientation of the solar cells relative to the solar flux.

3. Determining appropriate location of solar cells in components, such as the wings, to accommodate the desired number of solar cells.

7.2.2 Solar Energy Harvesting Model

The incident solar flux on the solar cells varies as a function of the position of the solar cell area and the suns azimuth, which is the angle along the horizon, and altitude, the angle from zenith. The altitude and azimuth angles vary with location, time of day, and time of year. The position of the solar cells area is dependent on the platform heading, pitch, yaw, roll and angle of solar cells relative to the platform body. To approach this problem, a generic case is considered.

An area, A_1, in the world frame with an efficiency of η, with a unit normal, $\hat{n}_{1\{W\}}$, is exposed to solar flux, Φ, with unit vector $\hat{n}_{\{W\}}$ which is defined in the world frame.

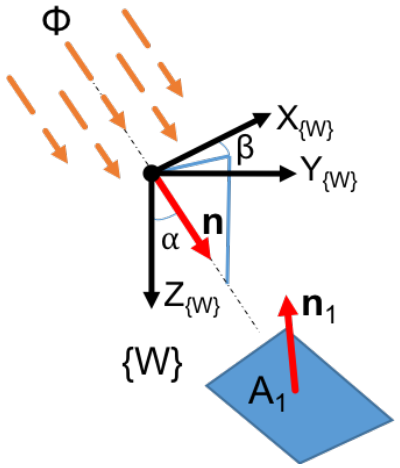

FIGURE 7.1: Incident solar flux shown in the world reference frame.

$$\Phi \hat{n}_{\{W\}} \cdot \eta_1 A_1 \hat{n}_{1\{W\}} \tag{7.1}$$

The unit vector $\hat{n}_{\{W\}}$ is defined in the world frame as:

$$\hat{n}_{\{W\}} = \begin{bmatrix} \sin\alpha\cos\beta \\ \sin\alpha\sin\beta \\ \cos\alpha \end{bmatrix} \tag{7.2}$$

Where α and β are shown in Fig 7.1.

To be generic, bearing in mind that various solar cell technologies could cover multiple areas, the total power generated would then be a sum of the product of the solar cell efficiencies and portion of solar flux incident on multiple areas.

$$P_{gen} = \Phi \hat{n}_{\{W\}} \cdot \eta_1 A_1 \hat{n}_{1\{W\}} + \Phi \hat{n}_{\{W\}} \cdot \eta_2 A_2 \hat{n}_{2\{W\}} + \Phi \hat{n}_{\{W\}} \cdot \eta_3 A_3 \hat{n}_{3\{W\}} \ldots \tag{7.3}$$

If the efficiencies of solar cells are the same ($\eta_i = \eta$) this simplifies as follows:

$$P_{gen} = \eta(\Phi\hat{n}_{\{W\}} \cdot A_1\hat{n}_{1\{W\}} + \Phi\hat{n}_{\{W\}} \cdot A_2\hat{n}_{2\{W\}} + \Phi\hat{n}_{\{W\}} \cdot A_3\hat{n}_{3\{W\}}...) \tag{7.4}$$

The maximum power available would occur when all of the solar cells are perpendicular to the solar flux such that the dot product of the unit vectors is equal to one.

$$P_{gen,max} = \eta(\Phi A_1 + \Phi A_2 + \Phi A_3...) \tag{7.5}$$

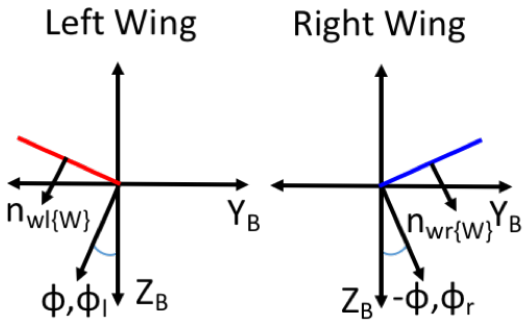

FIGURE 7.2: Flapping Wing Normal Vectors (platform nose coming out of the page)

To apply this to the flapping wing aerial vehicle case there are two areas of primary interest: the left and right wing areas occupied with solar cells. At a given body attitude, a wing position relative to the body (by an angle, ϕ_i) and the incident angle of the sun defined in the world frame:

$$P_{gen} = \eta\Phi(\hat{n}_{\{W\}} \cdot A_l\hat{n}_{wl\{W\}} + \hat{n}_{\{W\}} \cdot A_r\hat{n}_{wr\{W\}}) \tag{7.6}$$

If the left wing and the right wing are the same size and account for half the total solar cell area, A, then:

$$P_{gen} = \eta\Phi\frac{A}{2}(\hat{n}_{\{W\}} \cdot \hat{n}_{wl\{W\}} + \hat{n}_{\{W\}} \cdot \hat{n}_{wr\{W\}}) \tag{7.7}$$

Where outside of the efficiency, η, and area, A, the key to determine the power is the sum of the flux on the left and right wing described by each respective dot product.

$$\eta_f = Flux_l + Flux_r \tag{7.8}$$

Where

$$Flux_l = \hat{n}_{\{W\}} \cdot n_{wl\{W\}} \tag{7.9}$$

$$Flux_r = \hat{n}_{\{W\}} \cdot n_{wr\{W\}} \tag{7.10}$$

Rewriting equation 7.7:

$$P_{gen} = \eta\eta_f\Phi\frac{A}{2} \tag{7.11}$$

When each dot product is equal to one, (such that the sum, η_f, is equal to two), the solar flux and the area are aligned and the resulting maximum power is the following:

$$P_{max} = \eta A\Phi \tag{7.12}$$

It is assumed that the wings' surface go through a sinusoidal flapping cycle $\Delta\phi\sin(2\pi ft)$ as a function of time where, f, is the flapping frequency. The wing position normal

vectors and angle from the z axis (ϕ) are shown in Fig. 7.2. The unit vectors of the left and right wings, respectively, in the body frame are given by the following:

$$\hat{n}_{wl\{B\}} = \begin{bmatrix} 0 \\ -\sin\phi_l \\ \cos\phi_l \end{bmatrix} \tag{7.13}$$

$$\hat{n}_{wr\{B\}} = \begin{bmatrix} 0 \\ -\sin\phi_r \\ \cos\phi_r \end{bmatrix} \tag{7.14}$$

During symmetric flapping ϕ_l is equal to $-\phi_r$ such that they have equal amplitudes and opposite directions as shown in Fig. 7.2.

In order to compute the dot product the unit vectors must be rotated into the world frame from the body frame. In order to do so rotations matrices are employed as follows:

$$\hat{n}_{wl\{W\}} = R_z R_y R_x \hat{n}_{wl\{B\}} \tag{7.15}$$

$$\hat{n}_{wr\{W\}} = R_z R_y R_x \hat{n}_{wr\{B\}} \tag{7.16}$$

Where the rotation matrices are the following:

Yaw rotation

$$R_z = \begin{pmatrix} \cos\Psi & -\sin\Psi & 0 \\ \sin\Psi & \cos\Psi & 0 \\ 0 & 0 & 1 \end{pmatrix} \tag{7.17}$$

Pitch rotation

$$R_y = \begin{pmatrix} \cos\theta & 0 & \sin\theta \\ 0 & 1 & 0 \\ -\sin\theta & 0 & \cos\theta \end{pmatrix} \tag{7.18}$$

Roll rotation

$$R_x = \begin{pmatrix} 1 & 0 & 0 \\ 0 & \cos\phi & -\sin\phi \\ 0 & \sin\phi & \cos\phi \end{pmatrix} \tag{7.19}$$

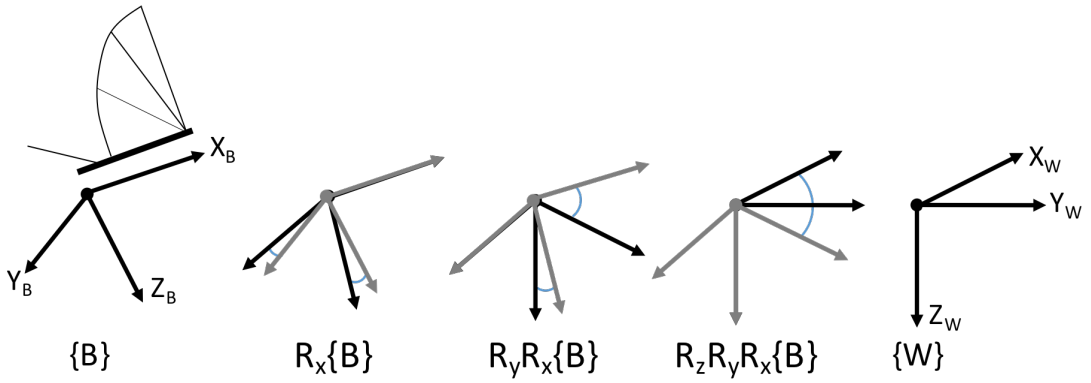

FIGURE 7.3: Rotations from the bird body reference frame to the world reference frame.

The fraction of solar flux incident on the wings varies as a function of the azimuth, which is the angle along the horizon, and altitude, which, in this case, is the degree from the vertical axis (not distance from the surface of the earth). These angles, which are converted into the world axis provided, are used for the calculation vary with location,

time of day, and time of year. A resources for such information is provided by the US Navy (http://aa.usno.navy.mil/data/docs/AltAz.php#Notes).

An assumption in the calculation is that the wings are rigid and do not balloon outwardly during the flapping cycle. Without a priori knowledge of the wing deformation, which is a function of flapping speed, force, and wing stiffness, it is difficult to assess what the camber achieved while flapping. In future iterations, it would be possible to add an additional rotation (or rotations) if there is a model for the wing deformation available. Additionally, this analysis does not consider blocking and shading effects where one wing covers the other. Shading is unlikely to be a large contributing factor as it would only occur when the sun is at low angles relative to the horizon (dusk or dawn). We assumed that only 80 % of the flux be available and therefore we used a factor of safety of 1.25 to address wing deformations, changes in flapping amplitude, and pitch variations. A method to address flapping amplitude and pitch variability sensitivity is discussed in further detail in the next section and results are shown in section 7.4.1.1.

7.2.3 Determination of Number of Solar Cells Required

Given that incident solar flux varies as a function of day of the year, time of day, and location, specifications for these parameters should be identified. Knowledge of trends can be helpful and used at the designers discretion. For example, knowledge the seasons can be helpful for picking favorable times of year.

An aerial vehicle may fly at various body positions (pitch and roll dependent) and may not fly in an ideal heading for power generation. For example, all possible headings are executed as the platform yaws to complete a circular trajectory. In light of this, it is important to do worst case analysis such that the heading with the lowest power

generated is identified because a failure due to loss of power could result in system shutdown which can cause a crash. As a means of doing this, numerous headings can be sampled to span 360 degrees of possible headings by incrementing the yaw value. At each sampled heading, the fraction of solar flux incident on each wing should be evaluated independently, such that the variation during the flapping cycle is captured, and summed to compute the total. Finally, time averaging the fraction of solar flux incident on the wings results will allow comparisons between different headings and conditions to locate the lowest value. While it is possible that an instantaneous value may be lower than required to provide power, it is assumed that power smoothing via the usage of storage devices and changes are shorter than system response time such that flight will be maintained.

Assuming the goal is to provide the entirety of the platform power, P, then the power generated must be greater or equal to that value.

$$\eta_{f,min} \frac{P_{max}}{2} \lambda \geq P \tag{7.20}$$

Where $\eta_{f,min}$ occurs due to the lowest value of the solar flux sum from both wings and λ is a safety factor.

A safety factor, λ, is introduced to consider variations in flapping amplitude, angle of attack, or other factors such as partial shading. Shading is unlikely to be a large contributing factor as it would only occur when the sun is at low angles relative to the horizon (dusk or dawn). To inform the factor of safety, sensitivity analysis considering angle of attack and flapping amplitude (in the case of a flapping wing aerial vehicle) is prescribed.

- **Angle of Attack Sensitivity:** To address potential sensitivity to angle of attack, the angle of attack should be varied across the potential operating range. While a generic safety factor can account for some variations in performance, it is useful to do sensitivity analysis to ensure that the safety factor is adequate and can quantify how much margin it provides. The calculations follow the same procedure as noted previously but are calculated using different angles of attack holding all other variables constant.

- **Flapping Amplitude Sensitivity:** In addition to sensitivity to angle of attack there may also be sensitivity to flapping range. When the flapping amplitude increases, the incident angle between the wings and the solar flux changes. The flapping amplitude should be varied for a constant angle of attack. These results coupled with angle of attack sensitivity should inform the safety factor that is ultimately used.

In this work a factor of safety of 1.25 was applied by assuming only 80 % of the calculated flux ($\lambda = 0.8$) is available. Sensitivity analysis is conducted in section 7.4.1.1 to inform this factor of safety.

Accounting for the directionality of the solar flux and position of the solar cells, the amount of power generated varies as a function of the efficiency of the solar cells, η, and the area, A. For a fixed efficiency, the area dictates the number of solar cells. Thus, the number of cells required is the total area of solar cells in a wing, A, divided by the area of each cell, A_{cell} (rounded up to the next whole number).

$$\lceil N \rceil = \frac{P_{max}}{P_{cell}} = \frac{A}{A_{cell}} \tag{7.21}$$

The number of cells required is the maximum power required for the worst case divided by the power generated by each cell rounded up to the next whole number because they are discrete.

7.2.4 Solar Cell Integration Location

As noted previously, changing wing designs can be difficult which makes using functional wing design favorable. Deformation and wing flexibility are important, thus stiffness and location of stiffness are of importance. Thicker solar cell materials which have a higher bending stiffness can reduce deformation of the multifunctional wings while flapping thus reducing lift and thrust generation. Given research findings Ho et al. [2003], Zhao et al. [2009] it is recommended that solar cells be integrated closer to the leading edge of the wing such that the trailing edge is unaffected. Additionally, the mass also can influence placement. Placing additional mass close to the motor minimizes the moment of inertia on the wing. Solar cells can also be integrated into static components of the platform, such as the body and tail to increase energy harvesting capability. The approach used in this work was to add solar cells by the leading edge close to the body first and work towards the wingtips. A new row was created upon reaching the wingtips. This was repeated until half the chord of the wing (as measured from the semi span) was reached at which point solar cells were integrated into the tail and body.

7.3 Time to Land Predictions using Aerodynamic Performance Modeling

To predict the available time to land for the FWAV, it is necessary to determine the payload capacity available to carry the batteries required to power the bird when the sun

sets. This can be ascertained by modeling the aerodynamic performance of the platform to determine factors influencing the payload capacity that we can characterize through experiments. During flapping flight, aerodynamic thrust and lift forces undergo periodic variations. A common modeling approach is to use a quasi-steady state assumption Madangopal et al. [2004], Shyy et al. [2013]. "Quasi steady-state wing theory assumes that the forces on a moving wing are equivalent to the sum of the forces on a fixed wing over a sequence of attitudes that track the wing motion. This model neglects acceleration forces and unsteady aerodynamic effects" Muijres et al. [2008]. In very small intervals of time, the flight is considered level with no acceleration. This implies that the forces in all directions must be equal during steady state flight, assuming no change in mass. Therefore, in the horizontal direction, thrust must be equal to the drag during steady state flight Anderson [2012]. The average thrust generated using the flapping wings should be equal to drag.

$$F_T = F_D \tag{7.22}$$

where drag is defined by Anderson [2012]:

$$F_D = \frac{1}{2}\rho V^2 S C_{D,p} \tag{7.23}$$

where V is the freestream velocity, A is the wing area, and $C_{D,p}$ is the drag coefficient of the wing. Substituting Eq. 7.23 into Eq. 7.22 yields:

$$F_T = \frac{1}{2}\rho V^2 S C_{D,p} \tag{7.24}$$

Because the average thrust is generated using the flapping wings

$$F_T = F_{FT} \tag{7.25}$$

We previously proposed a flapping wing model for the thrust taking into account the compliance of the wing as follows Mueller et al. [2010]:

$$F_{FT} = \int C_{D,f} \rho v^2 sin(\theta) dA \tag{7.26}$$

where $C_{D,f}$ is the drag coefficent of the wing for flapping, v is the magnitude of velocity at each point along the wing area, A, and θ is the camber angle determined by the shape of the wing during flapping.

Due to the stiffness of the wing, c, the velocity will be reduced by the drag force acting on the wing during flapping, D_f, as follows:

$$v = (1 - [D_f/(c\delta)])v_o \tag{7.27}$$

where δ is the displacement of the mid-chord of the semi-span of the wing if it were infinitely rigid, and v_o would be the subsequent magnitude of velocity.

Substituting Eq. 7.26 as the thrust term in Eq. 7.22 yields:

$$F_{FT} = \int C_{D,f} \rho v^2 sin(\theta) r^2 dA = \frac{1}{2} \rho V^2 S C_{D,p} \tag{7.28}$$

For steady flight with no acceleration in the vertical direction, forces must also sum to zero. Assuming no loss of mass or body forces aside from gravity, for steady state flight

conditions, average lift forces must offset the weight (Mg) Anderson [2012].

$$F_L = Mg \tag{7.29}$$

The aerodynamic lift is given by Anderson [2012] as:

$$F_L = \frac{1}{2}\rho S V^2 C_L \tag{7.30}$$

where C_L is the lift coefficient of the wing. Substituting Eq. 7.30 into Eq. 7.29 yields:

$$\frac{1}{2}\rho S V^2 C_L = Mg \tag{7.31}$$

It is possible to relate thrust to lift using the velocity. Rearranging Eq. 7.24 and solving for V^2 yields:

$$V^2 = \frac{2F_T}{\rho S C_{D,p}} \tag{7.32}$$

Substituting Eq. 7.32 into Eq. 7.30

$$F_L = \frac{C_L}{C_{D,p}} F_T \tag{7.33}$$

Substituting the thrust generated by flapping (Eq.7.26):

$$F_L = \frac{C_L}{C_{D,p}} \int C_{D,f} \rho v^2 sin(\theta) dA \tag{7.34}$$

Substituting this lift into equation 7.31 yields the maximum flight weight:

$$\frac{C_L}{C_{D,p}} \int C_{D,f} \rho v^2 sin(\theta) dA = Mg \tag{7.35}$$

The maximum flight mass, M_{Max}, occurs at the maximum total lift that can be generated.

$$F_{L,Max} = M_{Max} g \tag{7.36}$$

The payload, M_{pl}, is the difference between the base platform mass, M_{FWAV}, and the maximum flight mass, M_{Max}, as follows:

$$M_{pl} = M_{Max} - M_{FWAV} \tag{7.37}$$

The payload is the upper limit the on board energy storage mass.

$$M_b \leq M_{pl} \tag{7.38}$$

Energy available, E_a, is a function of the battery mass, M_b, and its energy density, ξ, as follows:

$$E_a = \xi \cdot M_b \tag{7.39}$$

Considering a complete loss of solar power contribution and a fully charged battery is onboard, the flight time, t_f, assuming an averaged power draw, is the following:

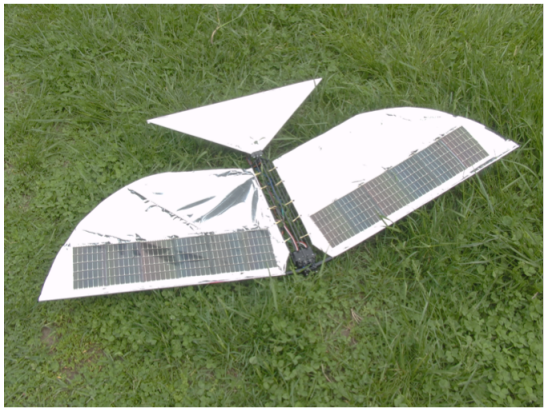

(a) Robo Raven III v1

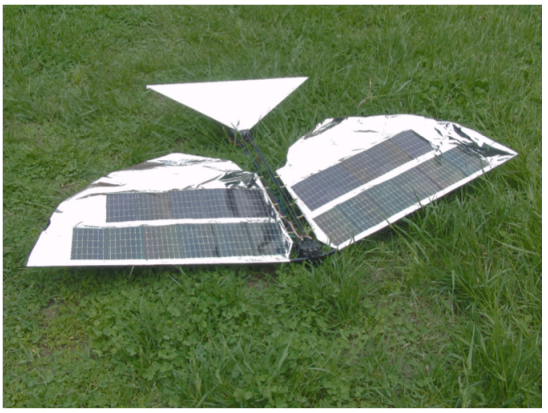

(b) Robo Raven III v2

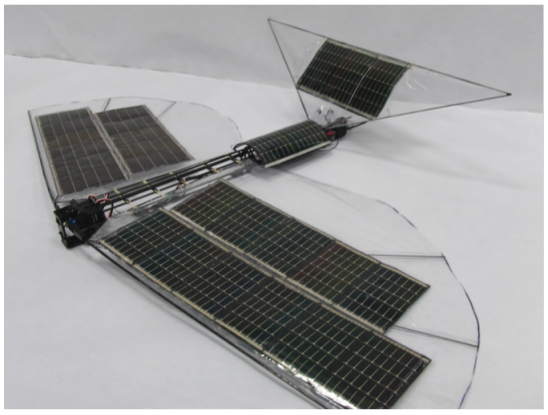

(c) Robo Raven III v3

(d) Robo Raven III v4

FIGURE 7.4: Versions 1-4 of the *Robo Raven III* platform with multifunctional wings using low efficiency Amorphous Silicon (A-Si) integrated solar cells

$$t_f = \frac{E_a}{P} \tag{7.40}$$

where, P, is the average power

If the entirety of the payload is occupied with battery mass, $M_b = M_{pl}$. The flight time before landing then becomes:

$$t_f = \frac{((F_L/g) - M_{FWAV}) \cdot \xi}{P} \tag{7.41}$$

7.4 Results

7.4.1 Design Case Study

In previous work, solar cells were integrated into an independent wing controlled Robo Raven FWAV platform developed at the University of Maryland, College Park where each wing is powered by a commercially available high speed and torque servo. An exploratory study was conducted to consider integration of low efficiency flexible amorphous silicon (A-Si) solar cells into the leading edge of the wings (Fig. 7.4(a)). After successful results and flight viability, the entirety of the wing was occupied with solar cells while maintaining the original wing design. This platform was unable to fly with an unmodified wing, however flight was possible after modification of the wing by increasing the area trailing edge of the wing with the addition of a *'tear drop'* as seen in Fig. 7.4(b). Wing deformation was tracked with digital image correlation to characterize the deformation of the wing, supporting findings via visual inspection of high speed video footage. Findings show that the wings move out of phase with the leading edge of the wing as the wing surface experiences torsion consistent with other findings Gerdes et al. [2017], Truong et al. [2017]. Additionally, both mechanical and electrical testing were performed. It was previously found that the bi-axial strain in the wing as well as the instantaneous thrust profile can be correlated with the percent change in power generated by wing integrated solar cells Perez-Rosado et al. [2015c].

To improve power generation, the *'tear drop'* wings were used in conjunction with solar cells integrated into the rear tail and tail assembly as seen in 7.4(c). Finally, drawing on scaling studies Gerdes et al. [2015], the wing size was increased by 66 % to provide additional payload capacity and area for solar cell integration. The *'tear drop'* was removed and the wing was returned to original wing design but scaled to increased the

area. This platform, Fig. 7.4(d) was successfully flown. There are limits to increasing wing size to integrate solar cells as the added mass has a detrimental effect on the motors as they are moved out of performance regimes both electrically and mechanically. Given limited motor torque, flapping amplitude decreases with wing mass at given speeds resulting in reduced force generation which is a problem unique to servo actuated wings. In a fixed amplitude system the angular rate of the wing movement would decrease. In light of reductions in actuator performance due to mass, increasing the efficiency of system components is a means of surpassing limitations.

7.4.1.1 Estimation of Available Solar Flux

The design goal is to have a Robo Raven III based FWAV platform flown in a unrestricted area around Los Angeles (LA) California, USA for roughly 6 months out of the year. At minimum there should be a 20 minute window of time where flight should be possible with consistent solar flux across 6 months of the year between 11:00 (11 AM) and 15:00 (3 PM) (when it would reasonable for the sun to be available). Given knowledge of the seasons, the best case conditions for 6 months of the year would roughly cover the trailing end of spring, the entirety of the summer, and the beginning of autumn.

Yaw headings were varied in increments of 18 degrees ($\pi/10$ rad) such that there are 20 unique headings considered to sample the 360 degrees of available headings. Along each sampled heading, one representative flapping cycle was considered to capture the variability of the wing position through the full range of motion. The fraction of solar flux incident on each wing was calculated at 50 different points of the flapping cycle. The flux on each wing was computed independently and summed. The 50 values were then time averaged using numerical integration to generate an aggregate number for each heading. Though the angle of attack varies in flight, the angle of attack is fixed at

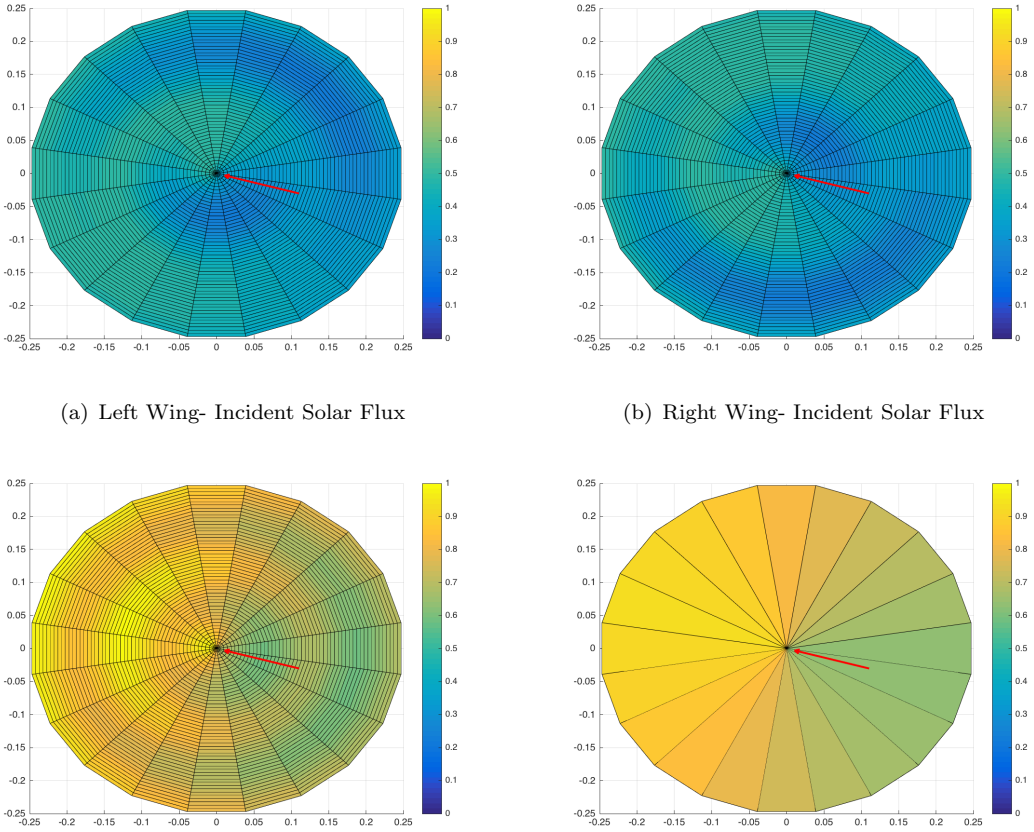

(a) Left Wing- Incident Solar Flux

(b) Right Wing- Incident Solar Flux

(c) Total Incident Solar Flux

(d) Total-Time Averaged Incident Solar Flux

FIGURE 7.5: Solar flux incident on the multifunctional wings calculated using energy harvesting model for June 21, 2017 at 11:00 AM PST

20 degrees with no roll. A flapping range of 60 degrees, 30 degree amplitude, is used in calculations and should be physically feasible based on previous findings.

The results for each wing normalized to half of the maximum and the sum total of both wings were graphed. The results for June 21, 2017 at 11 AM PST are shown in Fig. 7.5. In each graph straight up indicates north, down is south, right is east, and left is west. Each wedge represents a heading. The incident solar flux vector is shown by the red vector in each graph. The wings start straight outward, move upward first, then downward and return to the starting position. The time average of each heading was calculated via numerical integration are shown in Fig 7.5(d).

The results, considering no roll, show that the lowest value of total flux always occurs

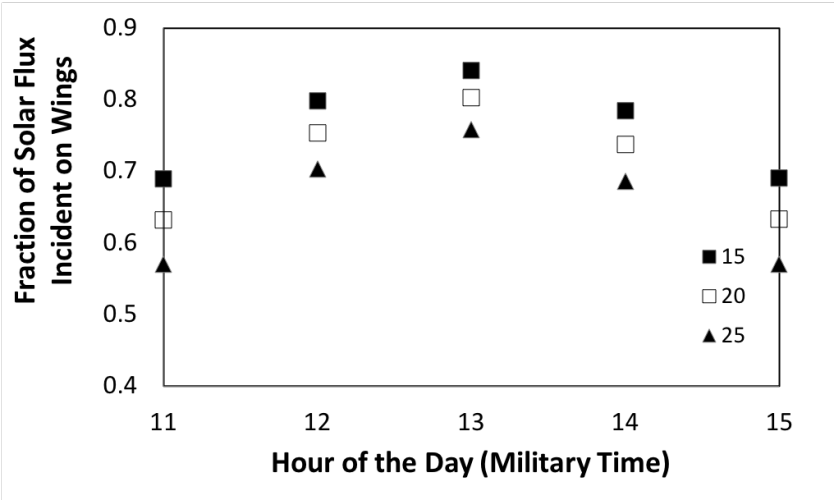

FIGURE 7.6: Sensitivity of the solar flux incident on the multifunctional wing for various angles of attack prior to a safety factor (legend is in degrees).

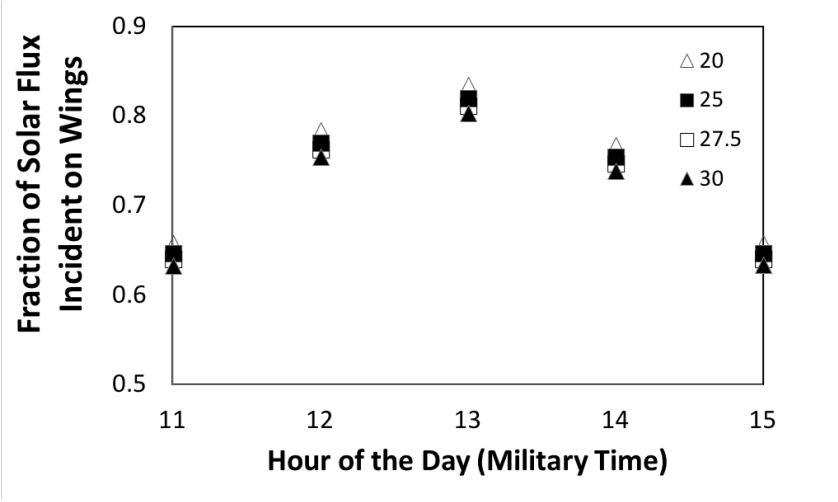

FIGURE 7.7: Sensitivity of solar flux incident on the multifunctional wings at a 20^o angle of attack for various flapping amplitudes prior to a safety factor (legend is in degrees).

when the heading is opposite the incident flux as defined by the azimuth. This occurs when the flux and attitude of the body given the angle of attack are nearly parallel. The best heading occurs when the heading is along the same direction of azimuth because the angle of attack and the solar flux are nearly perpendicular. Given that the worst heading will always be considered and it occurs opposite of the direction defined by azimuth when roll is negligible, the altitude angle is the determining factor for design when searching the data.

On June 21, 2017, the lowest value of 0.6406 occurs at 11 AM. A generic 20% safety factor for variations in angle of attack and flapping range would reduct this value to 0.51. From this value, a minimum the altitude angle of 52.4 degrees was found. Using this value an incremental search was used to find viable days of the year using values generated in 10 minute increments using the US Navy resource indicated above. It was determined that the times of year that provided at least a 20 minute window of time when flying in Los Angeles, CA were between the dates of March 11, 2017 - Sept 30, 2017. Additionally, it was found that June 21, provides a larger span of time for flight beyond the time specified of 11:00 to 15:00, specifically between 10:10 AM and 3:40 PM (15:40). To gain insight into the coverage of the generic safety factor, sensitivity analysis for angle of attack and flapping range were conducted.

To address potential sensitivity to angle of attack, the angle of attack was varied between 15, 20, and 25 degree at multiple times of day. The results of this sensitivity analysis are show in Fig. 7.6. The highest variability, 9.82 % occurred between the baseline data at 20 degrees and 25 degrees at 11 AM, which indicates the safety factor should be adequate if this effect is not compounded upon by another one. There may also be sensitivity to flapping range. For a fixed value of 20 degree angle of attack, the flapping amplitude was varied between 20 degrees, 25 degrees, 27.5 degrees, and 30 degrees. These results are shown in Fig. 7.7. At most, the highest variation from the original value was 3.9 %, which improves as the flapping range is lowered. Combined these findings suggest that a value of 0.51, representative of a 80 % reduction to provide a factor of safety, should be adequate to satisfy the design criteria.

7.4.1.2 Motor Power Estimation

The original Robo Raven was designed to work with low cost servo motors. These low cost motors tend to have poor efficiency. The servos currently used for the Robo Raven platform are Futaba S93572HV sBus servos (specifications are provided in Tab. 7.1). Two servos are employed, one for each wing, in order to obtain independent wing control. Based on electrical consumption and the operating point of the motors, using value of 41 W (5 A at 8.2 V), the efficiency of the motors was determined to be 45 %, meaning the peak power output requirement to flap is 18.5 W, which we have also previously confirmed using dynamometer measurements Gerdes et al. [2015].

Designing wings with integrated solar cells for these motors with such low efficiency will put unnecessary design constraints on the system. Therefore, we want to first estimate realistic efficiency for the powertrain. We have used a single high efficiency DC electric motor and gear train with previous FWAV platforms Gerdes et al. [2013a]. High efficiency motors (>90 %) and high efficiency gear trains are available from vendors, such as Maxon, which use an ironless rotor and stronger NdFe magnets to reduce eddy current losses. Therefore, this drive train can be configured with a motor and gear train combination which are each capable of 90 % efficiency, resulting in a combined efficiency would be 81 % when properly matched. Therefore, this configuration will require only 22.8 W be provided by the solar cells.

Since high efficiency, lightweight motors meeting FWAV requirements are currently very expensive, the possibility of a crash during a flight test or overheating the motor in a wind tunnel makes it cost prohibitive to use them for actual testing purposes. Therefore, all flight tests and wind tunnel characterization, to validate the modeling and performance

of wings with integrated HE solar cells, were only conducted with the Futaba S93572HV sBus servos currently employed on the Robo Raven platform.

TABLE 7.1: Futaba S93572HV sBus servo specifications

Voltage	Torque
6.6 V	20 kg cm (277.8 oz-in)
7.4 V	24.6 kg cm (341.7 oz-in)

Voltage	Speed
6.6V	0.07sec/60 deg
7.4V	0.06sec/60 deg

7.4.1.3 Prediction of Solar Cell Requirements

A flexible high efficiency gallium arsenide (GaAs) solar cell was identified. These flexible HE cells are manufactured using a metalorganic chemical vapor deposition process to grow a thin layer of GaAs. This layer of GaAs is coated with metal which provides electrical contact and light reflection. The combination is removed via an epitaxial lift-off (ELO) process which leaves a thin, flexible, and lightweight solar cell. These thin film flexible solar cells can be up to 30.8% efficient if they are dual junction, and the single junction cell are observed to be 24% efficient. A solar cell configuration capable of delivering 1.5 W of power was chosen.

Through previous investigations, the effects of integrating the A-Si cells is well known; however, integrating other solar cell materials may change their behavior due to differences in mass and stiffness. Comparison of the properties of the A-Si and GaAs solar cell modules can also be seen in Tab. 7.2. The A-Si modules came in encapsulation that needed to be removed to reduce the modules stiffness and mass. In the case of the GaAs modules, they were provided without encapsulation.

Given that a high efficiency motor and gear train combination will require 22.8 W, it is possible to determine the number of solar cells required to provide power under the condition of the sun being at its lowest solar altitude. Using the value for the solar flux incident on the wings during flapping determined from our modeling, which was 0.51, the corresponding power requirement would be 44.7 W. At 1.5 W per high efficiency solar cell, a total of 30 solar cells will meet the power requirements. It is important to note that if cells are placed on the body and tail, the orientation at those positions and their unchanging position means the incident value is increased to 0.76. For Robo Raven IIIv5, up to 6 cells can be integrated into the tail and body, which would add an additional 2.25 W of power generation. This means that only 12 GaAs modules will need to be integrated into each wing for a total of 24.

TABLE 7.2: Comparison of A-Si and high efficiency (HE) GaAs solar cell modules

	A-Si	GaAs
Operational Voltage (V)	3.6	7.4
Power (W)	0.33	1.50
Mass (g)	1.7	1.9
Area (cm^2)	84	71
Areal Density ($\frac{g}{cm^2}$)	0.020	0.026
Areal Power Density ($\frac{W}{cm^2}$)	0.004	0.020
Specific Power ($\frac{W}{g}$)	0.20	0.68

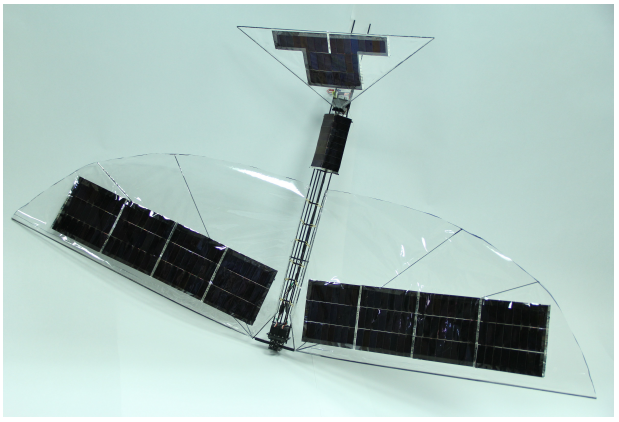

FIGURE 7.8: Robo Raven IIIv5- Flapping wing aerial vehicle with integrated high efficiency GaAs solar cells

7.4.2 Configuration of Solar Cells in Wings and Wind Tunnel Measurements

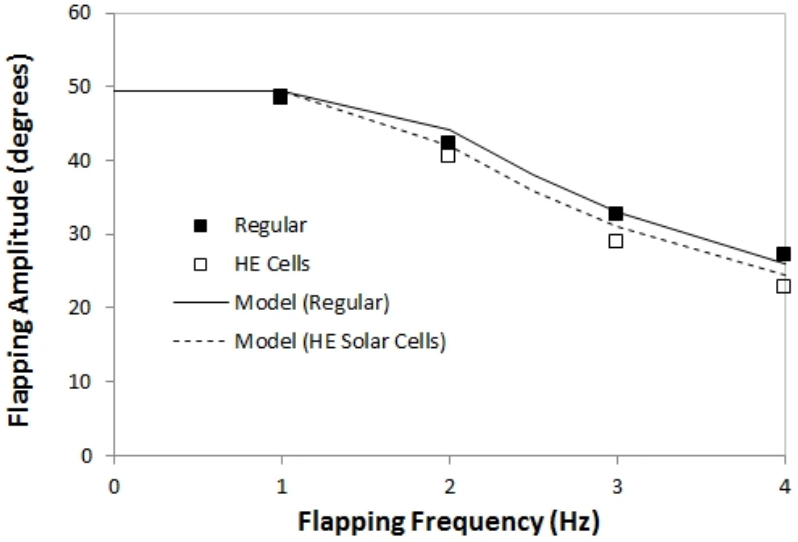

FIGURE 7.9: Comparison of the measured and modeled flapping amplitude versus flapping frequency, which exhibit degradation due to torque limitations of the servo motors, at a 0^o angle of attack for regular mylar wings and wings with high efficiency (HE) solar cells

From Robo Raven IIIv4, it was determined that placing the solar cells in the same location along the front spar would achieve similar coverage as the lower efficiency solar cells. Therefore, a solar cell configuration of 3 rows of high efficiency solar cells oriented lengthwise parallel to the front spar with 4 solar cells in each row was adopted for wind tunnel and flight testing. The wings were mounted to a test stand equipped with an American Digital E5 optical encoder to record the wing flapping amplitude and an ATI Mini40 six-axis transducer to record forces and moments. Measurements were recorded at 5 m/s air speed (as measured by a pitot tube) in a wind tunnel, which is similar to the air speed experienced during flight Gerdes et al. [2014]. The force transducer is capable of independently measuring all six components of force and torque using a Cartesian coordinate system and was calibrated by ATI to measure up to 40 N in the X and Y directions with a resolution of 1/100 N (1.02 g) of resolution and 120 N in the Z direction

with a resolution of 1/50 N (2.04 g). This test stand design was developed and utilized in previous flapping flight work Mueller et al. [2010], and has been used to characterize Robo Raven in previous work Gerdes et al. [2014], Perez-Rosado et al. [2014, 2015a,b]. Similar approaches with load cells have been used in other flapping research work Rose and Fearing [2014].

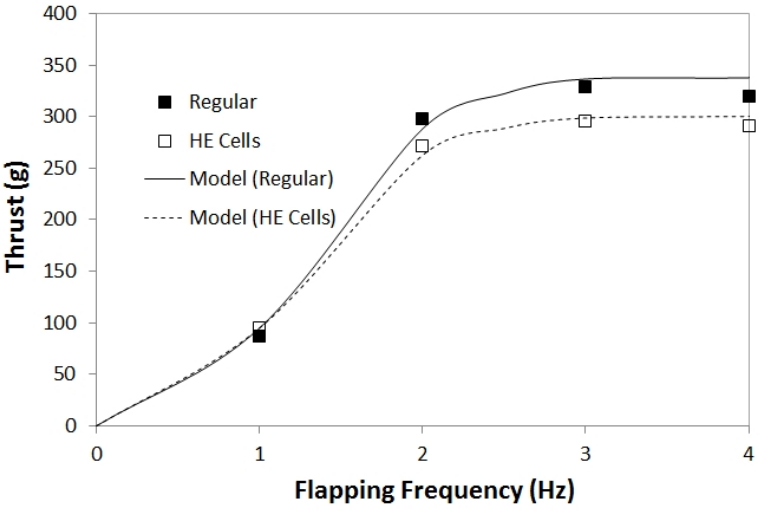

FIGURE 7.10: Comparison of measured and modeled thrust generated at various flapping frequencies between regular wings and wings with high efficiency (HE) solar cells integrated.

All data was recorded using a LabView VI interfaced with a National Instruments data acquisition system. During operation, the data was gathered for 5 seconds at 1,000 samples per second. Flapping was started and stopped before and after each capture window to ensure the data was indicative of steady state operation. Forces were determined by averaging data over multiple flapping cycles. Tests were run multiple times for a total of six trials. The average of the six trials was then calculated. To prevent issues with motor heating which could skew the results, the motors were cooled between trials.

Results for the effect of integrating HE solar cells in the wing can be seen in Fig. 7.9. We previously measured and modeled a significant reduction in flapping amplitude with flapping frequency due to torque limitations of the servo motor Gerdes et al. [2017].

The heavier and stiffer wings and greater forces generated by the wings also end up in a higher reduction in flapping amplitude. This can also be seen in the comparison of the thrust model in Eq.7.26 with the test stand measurements, seen in Fig. 7.10. The integration of HE solar cells decreases thrust by 15% at flapping frequencies of 2 Hz, which corresponds to a wing stiffness increase of approximately 50%, consistent with the measured stiffness, and a drag increase of 60%.

Insight into the parameters in Eq (34) can be obtained by running experiments in the wind tunnel with and without air to determine the lift and thrust forces due to flapping, as well as the aerodynamic characteristics of the platform. From these measurements, we can predict the steady state flight velocity, and the subsequent total lift of the platform. First, we note that the drag force is directly related to the velocity of air in the wind tunnel, V_{wt} and the difference in thrust force with and without air (i.e., the residual thrust), $F_T(V_{wt}) - F_T(0)$, as follows:

$$F_T(0) - F_T(V_{wt}) = \frac{1}{2}\rho V_{wt}^2 S C_{D,p} \tag{7.42}$$

Next, we note that we can also measure the lift force, F_L, in a similar manner:

$$F_L(V_{wt}) - F_L(0) = \frac{1}{2}\rho V_{wt}^2 S C_L \tag{7.43}$$

For symmetric flapping, F_L will be 0. Having determined the coefficients $C_{D,p}$ and C_L, from Eqs. 7.42 and Eq. 7.43 it is possible to determine the steady state velocity, V and subsequent lift as follows:

$$V = \sqrt{\frac{F_T(0)}{F_T(0) - F_T(V_{wt})}} V_{wt} \tag{7.44}$$

$$F_L = \frac{[F_L(V_{wt}) - F_L(0)]}{V_{wt}^2} V^2 = \frac{[F_L(V_{wt}) - F_L(0)]F_T(0)}{F_T(0) - F_T(V_{wt})} \tag{7.45}$$

It is interesting to note that the determination of total lift in Eq. 7.45 is independent of the wind tunnel velocity, and depends only on the test stand measurements. This is one advantage of using the 6 DOF load cell to determine thrust and lift forces simultaneously. Using the measured platform weights of 364.1 g for wings with HE solar cells and 316.3 g for regular wings, it was possible to determine the payload capacity of both platforms, as seen in Fig. 7.11. It is important to note that at a flapping frequency of 1 Hz, there is insufficient lift for the platform to fly, therefore that payload capacity is not reported. Despite the nearly 50 g greater platform weight and another 50 g lower thrust, the predicted payload capacity was nearly the same at higher flapping frequencies for both platforms. An explanation for this can be obtained by comparing the lift coefficients in Fig. 7.12 between wings with integrated HE solar cells versus regular wings. While at lower flapping frequencies the lift coefficients are similar, producing ratios of nearly 100%, at higher frequencies the ratio increases significantly to 150%, which essentially offsets the lower flight velocity due to the reduced thrust resulting in the similar payload capacity for wings with and without HE solar cells.

7.4.3 Flight Test with High Efficiency Solar cells

After characterizing forces on the test stand, the flight platform was taken outdoors to verify flight feasibility. While the load cell measurements provided insight into the

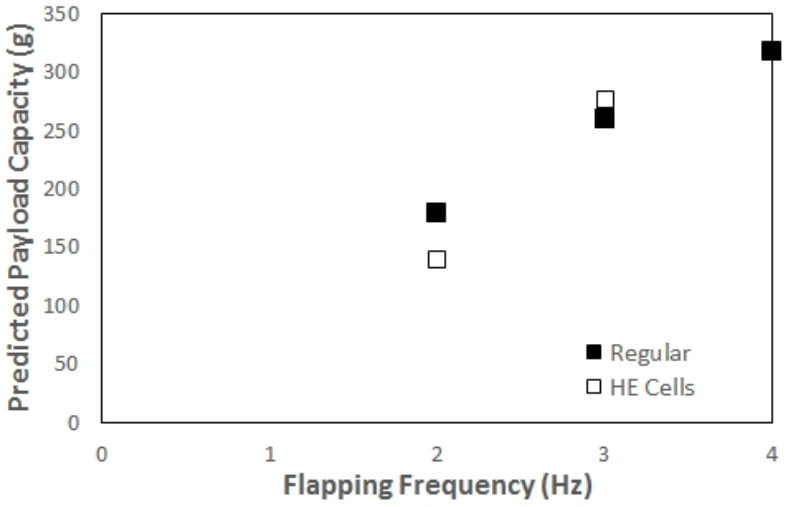

FIGURE 7.11: Predicted payload capacity versus the flapping frequency for regular wings and wings with HE solar cells. At a 1 Hz flapping frequency, there is insufficient lift to fly, therefore those calculations are not reported.

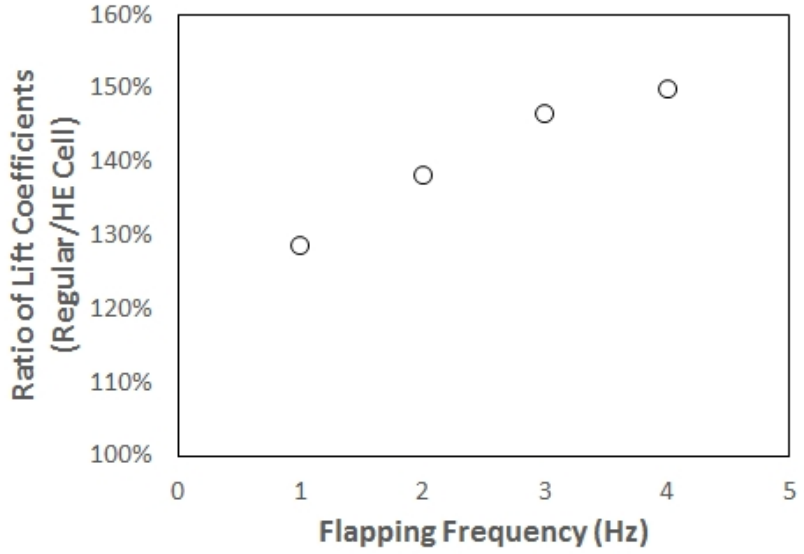

FIGURE 7.12: Ratio of lift coefficients for of wing with integrated HE solar cells versus regular wings indicating better lift from the wings with HE cells due to the greater stiffness, which offsets the reduction in thrust producing a similar payload capacity between the wings.

effects of integrating HE solar cells into the wings on the subsequent aerodynamic force production, they are still not a completely accurate representation of in-flight performance, since the actual AOA varies during flight due to the oscillations in thrust and

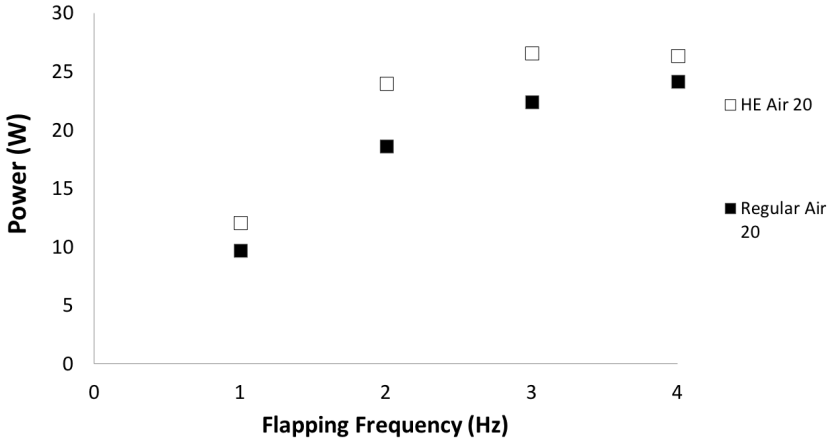

FIGURE 7.13: Comparison of measurements of electrical power required to flap a single wing using high torque servo at 8.2 V between regular mylar wings and wings with high efficiency (HE) solar cells

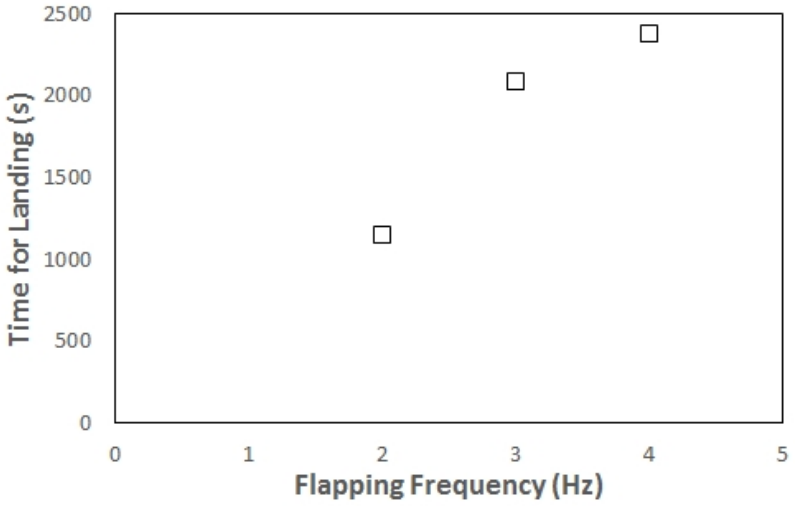

FIGURE 7.14: Predicted time to land for wings with HE solar cells versus frequency based on the predicted payload capacity. Since, as previously stated in Fig. 7.11, the platform is incapable of flight at 1 Hz, those calculations are not reported.

lift forces. For this reason flight testing was critical to determine basic flight feasibility. Flight tests were conducted inside of the University of Maryland Fearless Flight Facility (F3), a netting enclosed outdoor flight space. Flights tests were conducted on days where the wind speed was below 2 knots (1.03 m/s) using a 7.4 V 470 mAh LiPo battery for power. The platform was hand launched and allowed to reach steady flight.

FIGURE 7.15: Video frames from the flight of Robo Raven IIIv5.

Rudder control was only utilized during the launch period and/ or to avoid obstacles. Sustainable flight was possible. Video frames of the flight footage are shown in Fig. 7.15 with successive (non consecutive) frames going from top to bottom from left to right. It can clearly be seen that the results were able to translate into a flight capable platform with sufficient battery capacity to enable the desired landing time.

7.4.4 Electrical Performance

To ascertain that HE solar cells are capable of generating substantially more power than previous versions of Robo Raven III, electrical tests were conducted on actual HE solar cells. Voltage for an array of GaAs solar cells was measured outside under sunlight in College Park, MD. On the day of testing the peak altitude was at 71.2 degrees and 176.9 east of north as provided by the previously noted reference. Solar cells have a characteristic I-V curve between the open circuit voltage and short circuit current where current and voltage are inversely proportional. Since the highest voltage

and highest current do not occur simultaneously, resistors were used to load the solar cells and enable measurement. The average of the six I-V curves models based on this experimental data, and the resulting power, is provided in Fig. 7.16. It is important to note that the solar flux varies with location throughout the globe, so knowing the flux at those locations relative to College Park, MD will enable the results to be scaled accordingly.

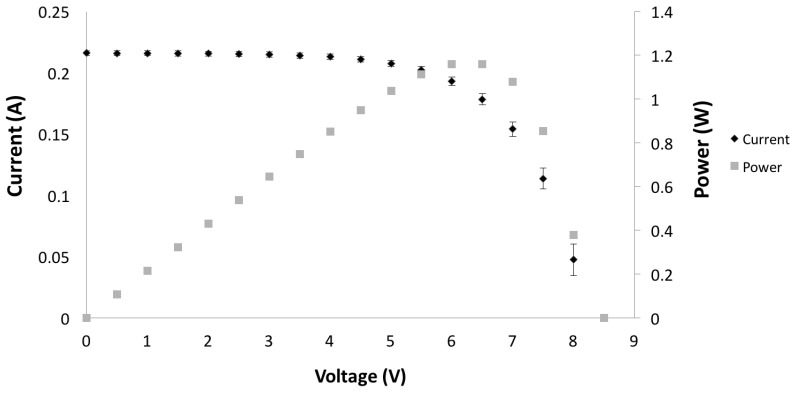

FIGURE 7.16: The average I-V and corresponding power curves measured over 6 GaAs solar cell modules.

The power draw for 1 servo driving an HE wing is compared to 1 servo driving an unmodified mylar wings in Fig. 7.13. Using the analysis in equation Eg. 7.41 and the payload results in Fig. 7.11, it was possible to predict the time to land, as seen in Fig.7.14. A specific energy capacity of 414 J/g for a LiPo battery used for the calculations. The increased payload capacity at the higher flapping frequency does offset the slight increase in power consumption, so that nearly 2500 seconds of flight time is possible after the sun is lost, which is a significant amount of time to allow the platform to find and locate a location to rest and recharge the next day before resuming flight.

At our location, the measured electrical performance of the HE solar cell modules underperforms the specifications provided by the manufacturer. Testing location, time of day,

variation from ideal flux rating, and handling outside of laboratory conditions without encapsulated contribute to the lower performance. The manufacturer provided calibration information for these solar cells using an artificial light source of 1,000 W/m^2, which indicated an open circuit voltage of 8.5 V and short circuit current of 200 mA per module prior to shipping. Although the results reported for less than optimal conditions, it is reasonable to make predictions that it is possible to achieve performance closely matching the specifications of the manufacturer, which is a peak output of 1.5 W per module, when in comparable solar flux.

7.5 Conclusions

Unlike previous work, where low efficiency (<6%), flexible A-Si solar cells were incorporated into the wings of a FWAV to allow for the battery to recharge without using a battery charger, the goal for this work was to develop a framework for designing a multifunctional wing with high efficiency (24% efficiency) flexible GaAs solar cells such that the battery can support power spikes or provide backup power when needed. The framework consisted of: (1) predicting the energy generated by the solar cells, (2) predicting the number of solar cells required to meet the power requirements of the FWAV, (3) determining of the effects of placing solar cells in the wings on the thrust and lift generated by flapping, and (4) a system model of flapping flight to predict the flight mass and the payload available for carrying components such as batteries to provide additional power in the event of power spikes and in the event that the FWAV needs to land to recharge.

The model for the energy generated by the solar cells considers changes between solar cell area and solar flux incident on the multifunctional wing brought about by the various

headings and wing position during flapping. A key finding was the fraction of solar flux incident on the FWAV will be only 0.94 during flight when the sun is at its zenith, and that the fraction of solar flux incident on the solar cells in the wings would be further reduced to 0.88 due to flapping. At the lowest solar altitude, these values will reduce to 0.68 and 0.63 respectively. If a safety factor of 1.25 is employed, then the lowest value for the purposes of design will be 0.51. Flexible GaAs solar cells were integrated into the wings, body, and tail of a FWAV known as Robo Raven IIIv4. The proposed modeling framework showed that a replacement motor and gear train combination with an efficiency of 81% would be capable of matching the power output of the high efficiency solar cell configuration for Robo Raven IIIV4 to achieve flight where batteries are only used in events of power spikes and to provide additional time for the FWAV to land for recharging.

In addition to determining the resulting wing design with integrated HE solar cells capable of meeting the power requirements for flight, the resulting payload capacity for the battery backup was also determined for the wing design. Measurements were made on a test stand in a wind tunnel, and an analysis was developed for predicting the effects of integrating the HE solar cells on the thrust and lift production of the flapping wings, as well as the change in aerodynamic performance. These predictions were validated with the experimental measurements, and it was determined that the integration of solar cells reduced thrust because the wings were 50% stiffer with a 60% increase in drag during flapping. However, the lift coefficient of wings without HE solar cells were 70% less than those with HE solar cells, which offset the lower steady state flight velocity associated with the lower thrust, resulting in a similar payload capacity for both wing designs that enables up to 2500 sec of time to safely land in an area where the batteries can recharge the next day. Outdoor flights in a netted test facility with a

backup battery validated the flight capability of the platform.

Chapter 8

Future Work

8.1 Combining Techniques

Multiple strategies to increase performance of flapping wing aerial vehicles have been presented, including propeller assistance to increase payload via aerodynamic lift, inertial control to provide maneuverability, integration of flexible storage media with discussions of wing scaling, and integration of photovoltaics. These strategies need not be used independently. It is possible that shortcomings of each can be reduced in a favorable way. For example, a wing with solar integration may be unable to fly via flapping because of a combination of high mass and low aerodynamic force generation as a result of deformation reductions. While flight may not be possible using a specific wing design using pure flapping it maybe be feasible when used in conjunction with propeller propulsion. This was the case with the wings shown in Fig. 8.1. The wings were unable to be used while flapping solely but were able to be flown on a propeller platform.

A paradigm of recharging the robots power source through the use of photovoltaics was highlighted by Doyle [2011] as a key feature that a perching capability could allow. The

FIGURE 8.1: Propeller assisted flapping wing aerial vehicle with multifunctional solar cell wings

value of inertial control to provide rapid deceleration to provide favorable conditions to perch is appealing when considered with a solar harvesting capable platform.

Combining the energy storage and solar cells with the propeller assistance provides an interesting trade-off space. It is unlikely that solar cells will be able to provide the necessary power. In light of this energy storage is required. Flexible energy storage in conjunction with traditional batteries would likely be the most favorable strategy. Ultimately, a comprehensive fabrication process for creating solar cell material that creates the outermost layer of a battery structure would be a favorable combination to save mass. Both integrated solar cells and batteries will increase the power required to flap and change flapping performance but the addition of propeller assistance alters the requirements for flapping. A lower flapping frequency may be required or no flapping is required in the case of the multi-modal flight capability. Inertial control may allow for changes between flight envelopes favorable for aggressive maneuvers or energy conservation.

The flight time paradigm expressed previously was the following:

$$t_f = \frac{((F_L/g) - M_{FWAV}) \cdot \xi}{P} \tag{8.1}$$

The inclusion of batteries and solar cells modifies this by changing M_{FWAV} and more than likely increasing the power required, P. The inclusion of energy does provide energy generation, P_{gen} which was based on the incident solar flux.

$$t_f = \frac{((F_L/g) - M_{FWAV}) \cdot \xi}{P - P_{gen}} \tag{8.2}$$

where the lift is represented by a combined model considering thrust.

$$F_L = \frac{C_L}{C_{D,p}}(F_{PT} + F_{FT}) \tag{8.3}$$

Furthermore, in both the battery work and the solar cell work, the wing size was scaled to increase the available area and aerodynamic force generation. A propeller assisted version with scaled wings (33% larger) was utilized to successfully drop a 60 g tennis ball after achieving sustainable flight with both the mass of the release mechanism and the tennis ball. The scaling of wing size offers an additional trade-off space as it modifies the area term. A number of flight capable wing sizes have been identified in other work Gerdes et al. [2015]. Finally, two different propellers have been flown as 5030 propellers were used Holness et al. [2018a] and 5040 propellers were used for thrust in the inertial control presented in this work and to achieve higher flight speeds in Roberts et al. [2015, 2016, 2017]. The contribution of propeller thrust is modified as C_T changes due to

propeller pitch (Eq. 8.4). Additionally, higher pitch increase thrust generation at the cost of increasing power demands.

$$F_{PT} = C_T \rho \Omega^2 D^4 \tag{8.4}$$

8.2 System Modeling for Control

A system model for the platform with propellers and flapping wings has yet to be generated. A plant model can be developed in future work to improve control, increase insights into analysis of platform flight performance, and help clarifying ways to either leverage or improve inertial control.

8.3 Exploration of Intermittent Flapping Flight

Larger bird species which are able to flap intermittently and actuate their wings to adjust seemingly effortlessly to take advantage of airflow phenomena such as unsteady effects and thermal currents. In contrast, robotic platforms require continuous or near continuous actuation to maintain flight. The advantage of mixed mode flight is that it could allow for experimentation using intermittent flapping propulsion. Future work exploring intermittent flapping specifically energy trade offs and aerodynamic advantages associated (as the wings do not have to travel through the wake of a previous wing stroke) with intermittent flapping can be explored.

Chapter 9

Intellectual Contributions

Due to limitations of current technologies and understanding of flapping wing flight, platform endurance, maneuverability and mission capabilities are limited compared to fixed wing aircraft and rotorcraft. In this work, strategies for improving the performance of a flapping wing aerial vehicle were presented to reduce performance shortcomings, specifically: mixed-mode operation with propeller assistance to increase payload which increases endurance by carrying additional energy storage, climb rate given excess power, and maneuverability as a result of the climb rate; maneuverability and flight envelop modulation via inertial control; energy storage with multifunctional battery wings with considerations of flexible high energy density Galvanic cell and LiPo; and endurance via energy harvesting with multifunctional wings. In pursuit of these aims, the following intellectual contributions have been realized.

9.1 Mixed Mode Flight Principles for Propeller Assisted Flapping Flight

The mixed mode approach posed issues of energy efficiency and thrust generation in the face of coupling and interactions between. The viability and a basic understanding of the usage of propeller assistance in a unique hybrid approach was demonstrated. Trade-offs and advantages not seen in either of the parent methodologies were identified. A basic knowledge set was created that it could be extended to explore cost to go for path planning, minimum energy configurations for solar harvesting while gliding or soaring on thermals, and a template for scaling via changes in propeller or wing size was developed. Published in Holness et al. [2015, 2018a]

9.2 Deceleration via Inertial Control on Propeller Assisted Flapping Wing Air Vehicle

The ability to utilize inertial control to vary flight envelope of aerial vehicles was demonstrated. A modeling framework was developed to consider changes in center of mass and moments to describe a means of increasing angle of attack and drag to decelerate the platform. Additional benefits of the mixed model concept are demonstrated given sustained high angles of attack through the use of directed thrust and flapping wings. This work can serve as a basis for collision avoidance strategies given rapid breaking, improving aerial imagining as time over target can be increased as a result of change in flight envelope, and perch and stare capabilities.

9.3 Predictive Modeling of Flight Endurance considering Multifunctional Wings with Energy Storage Media

While this approach does not consider the degradation of performance which occurs as a function of battery performance, it provides a starting approximation for idealized performance considering power consumption and storage. The importance of accounting for the benefits and tradeoffs of the approach naturally yields a predictive model. Specifically, mass effects on energy consumption were elucidated. The consideration of mass efficiency and economy is an interesting metric unique to multifunctional materials which is especially relevant for aircraft. The approach developed should be easily adaptable to other UAV systems, but specifically smaller systems which cannot easily accommodate additional payload. Holness et al. [2016]

9.4 Design Framework to Design for Energy Autonomy via Solar Energy Harvesting

A design framework to consider power generation for aerial vehicles was developed. As part of this framework, a power generation model was described to specifically consider providing energy autonomy for flapping wing platforms where the solar cells move relative to the body of the platform as the body itself moves relative to the incident solar flux. A prediction strategy to describe the time-to-land was described for use when power via solar energy generation is not available. Holness et al. [2018b].

Bibliography

AimDroix. Xray tilt-rotor quad, Dec 2016. URL http://store.aimdroix.com/product-p/adx1501.htm.

J. D. Anderson. *Introduction to Flight*. McGraw Hill, New York,NY, 7 edition, 2012.

S. R. Anton and D. J. Inman. Vibration energy harvesting for unmanned aerial vehicles. In *The 15th International Symposium on: Smart Structures and Materials & Nondestructive Evaluation and Health Monitoring*, pages 692824–692824. International Society for Optics and Photonics, 2008.

N. Beals and A. R. Jones. Lift production by a passively flexible rotating wing. *AIAA Journal*, 53(10):2995–3005, 2015.

W. Bejgerowsk, A. Ananthanarayanan, D. Mueller, and S. K. Gupta. Integrated product and process design for a flapping wing drive-mechanism. *ASME Journal of Mechanical Design*, 131(061006), 2009.

W. Bejgerowski, J. Gerdes, S. K. Gupta, H. Bruck, and S. Wilkerson. Design and fabrication of a multi-material compliant flapping wing drive mechanism for miniature air vehicles. In *ASME IDETC/CIE, 34th Annual Mechanisms and Robotics Conference, Parts A and B*. ASME, August 2010. DETC2010-28519.

Boeing. Boeing: Historical snapshot: V-22 osprey tiltrotor, Dec 2016. URL www.boeing.com/history/products/v-22-osprey.page.

S. Bouabdallah, R. Siegwart, and G. Caprari. Design and control of an indoor coaxial helicopter. In *Intelligent Robots and Systems, 2006 IEEE/RSJ International Conference on*, pages 2930–2935. IEEE, 2006.

J. B. Brandt and M. S. Selig. Propeller performance data at low reynolds numbers. In *49th AIAA aerospace sciences meeting*, pages 2011–1255, 2011.

A. J. Brezina and S. K. Thomas. Measurement of static and dynamic performance characteristics of electric propulsion systems. *The 51th AIAA Aerospace Sciences Metting*, pages 2013–0500, 2013.

R. Briggs, J. Lee, M. Haberland, and S. Kim. Tails in biomimetic design: Analysis, simulation, and experiment. In *Intelligent Robots and Systems (IROS), 2012 IEEE/RSJ International Conference on*, pages 1473–1480. IEEE, 2012.

M. Bronz, J. M. Moschetta, P. Brisset, and M. Gorraz. Towards a long endurance mav. *International Journal of Micro Air Vehicles*, 1(4):241–254, 2009.

C. Casarez, I. Penskiy, and S. Bergbreiter. Using an inertial tail for rapid turns on a miniature legged robot. In *Robotics and Automation (ICRA), 2013 IEEE International Conference on*, pages 5469–5474. IEEE, 2013.

E. Chang-Siu, T. Libby, M. Tomizuka, and R. J. Full. A lizard-inspired active tail enables rapid maneuvers and dynamic stabilization in a terrestrial robot. In *Intelligent Robots and Systems (IROS), 2011 IEEE/RSJ International Conference on*, pages 1887–1894. IEEE, 2011.

E. Chang-Siu, T. Libby, M. Brown, R. J. Full, and M. Tomizuka. A nonlinear feedback controller for aerial self-righting by a tailed robot. In *Robotics and Automation (ICRA), 2013 IEEE International Conference on*, pages 32–39. IEEE, 2013.

R. T. Chen. A survey of nonuniform inflow models for rotorcraft flight dynamics and control applications. Technical report, NASA, 1989.

R. Cory and R. Tedrake. Experiments in fixed-wing uav perching. In *AIAA Guidance, Navigation and Control Conference and Exhibit*, page 7256, 2008.

W. Crowther. Perched landing and takeoff for fixed wing uavs. In *NATO symposium on unmanned vehicles for aerial, ground, and naval military operations*, pages 9–13, 2000.

L. Daler, J. Lecoeur, P. B. Hählen, and D. Floreano. A flying robot with adaptive morphology for multi-modal locomotion. In *Intelligent Robots and Systems (IROS), 2013 IEEE/RSJ International Conference on*, pages 1361–1366. IEEE, 2013.

T. W. Danko, A. Kellas, and P. Y. Oh. Robotic rotorcraft and perch-and-stare: Sensing landing zones and handling obscurants. In *Advanced Robotics, 2005. ICAR'05. Proceedings., 12th International Conference on*, pages 296–302. IEEE, 2005.

K. M. De Clercq, R. de Kat, B. Remes, B. W. van Oudheusden, and H. Bijl. Aerodynamic experiments on delfly ii: unsteady lift enhancement. *International Journal of Micro Air Vehicles*, 1(4):255–262, 2009.

G. De Croon, K. De Clercq, R. Ruijsink, B. Remes, and C. De Wagter. Design, aerodynamics, and vision-based control of the delfly. *International Journal of Micro Air Vehicles*, 1(2):71–97, 2009. ISSN 1756-8293.

M. T. DeGarmo. Issues concerning integration of unmanned aerial vehicles in civil airspace. *Center for Advanced Aviation System Development*, page 4, 2004.

Delfly. Delfly, Dec 2016. URL http://www.delfly.nl/home.html.

N. T. Depenbusch, J. J. Bird, and J. W. Langelaan. The autosoar autonomous soaring aircraft part 2: Hardware implementation and flight results. *Journal of Field Robotics*, 35(4):435–458, 2018.

R. W. Deters and M. S. Selig. Static testing of micro propellers. In *26th AIAA Applied Aerodynamics Conference*, pages 18–21, 2008.

M. Di Luca, S. Mintchev, G. Heitz, F. Noca, and D. Floreano. Bioinspired morphing wings for extended flight envelope and roll control of small drones. *Interface focus*, 7 (1):20160092, 2017.

D. B. Doman, C. Tang, and S. Regisford. Modeling interactions between flexible flapping-wing spars, mechanisms, and drive motors. *Journal of Guidance, Control, and Dynamics*, 34(5):1457–1473, 2011.

C. E. Doyle. *Avian-inspired passive landing mechanisms for perching rotorcraft*. The University of Utah, 2011.

C. E. Doyle, J. J. Bird, T. A. Isom, J. C. Kallman, D. F. Bareiss, D. J. Dunlop, R. J. King, J. J. Abbott, and M. A. Minor. An avian-inspired passive mechanism for quadrotor perching. *IEEE/ASME Transactions on Mechatronics*, 18(2):506–517, 2013.

R. D'Sa, D. Jenson, and N. Papanikolopoulos. Suav: Q-a hybrid approach to solar-powered flight. In *Robotics and Automation (ICRA), 2016 IEEE International Conference on*, pages 3288–3294. IEEE, 2016.

D. J. Edwards. Autonomous locator of thermals (aloft) autonomous soaring algorithm. Technical report, NAVAL RESEARCH LAB WASHINGTON DC, 2015.

C. Ellington. The aerodynamics of hovering insect flight. iii. kinematics. *Philosophical Transactions of the Royal Society of London B: Biological Sciences*, 305(1122):41–78, 1984a.

C. Ellington. The aerodynamics of hovering insect flight. iv. aeorodynamic mechanisms. *Philosophical Transactions of the Royal Society of London B: Biological Sciences*, 305 (1122):79–113, 1984b.

C. Ellington. The aerodynamics of hovering insect flight. vi. lift and power requirements. *Philosophical Transactions of the Royal Society of London B: Biological Sciences*, 305 (1122):145–181, 1984c.

W. Engblom. Novel approach to high-altitude long-endurance stationkeeping. In *30th AIAA applied aerodynamics conference New Orleans, Louisiana*, pages 25–28, 2012.

M. R. Evans, M. Rosén, K. J. Park, and A. Hedenström. How do birds' tails work? delta–wing theory fails to predict tail shape during flight. *Proceedings of the Royal Society of London B: Biological Sciences*, 269(1495):1053–1057, 2002. ISSN 0962-8452. doi: 10.1098/rspb.2001.1901.

Festo. Smartbird, Dec 2016. URL https://www.festo.com/group/en/cms/10238.htm.

J. Gerdes. Design, analysis, and testing of a flapping-wing miniature air vehicle. MS Thesis, University of Maryland, College Park, College Park, MD, 2010.

J. Gerdes, S. K. Gupta, and S. Wilkerson. A review of bird-inspired flapping wing miniature air vehicle designs. *ASME Journal of Mechanism and Robotics*, 4(2):021003.1–021003.11, 2012.

J. Gerdes, K. Cellon, H. Bruck, and S. Gupta. Characterization of the mechanics of compliant wing designs for flapping-wing miniature air vehicles. *Experimental Mechanics*, 53(9):1561–1571, 2013a.

J. Gerdes, L. Roberts, E. Barnett, J. Kempny, A. Perez-Rosado, H. Bruck, and S. K. Gupta. Wing performance characterization for flapping wing air vehicles. In *ASME IDETC/CIE, 37th Mechanisms and Robotics Conference*. ASME, August 2013b. DETC2013-12479.

J. Gerdes, A. E. Holness, A. Perez-Rosado, L. Roberts, A. Greisinger, E. Barnett, J. Kempny, D. Lingam, C. Yeh, H. Bruck, and S. K. Gupta. Robo raven: A flapping wing air vehicle with highly compliant and independently controlled wings. *Soft Robotics*, 1(4):275–288, March-April 2014.

J. Gerdes, H. Bruck, and S. K. Gupta. A systematic exploration of wing size on flapping wing air vehicle performance. In *ASME IDETC/CIE, 39th ASME Mechanism and Robotics Conference*. ASME, August 2015. DETC2015-47316.

J. W. Gerdes, H. A. Bruck, and S. K. Gupta. Improving prediction of flapping-wing motion by incorporating actuator constraints with models of aerodynamic loads using in-flight data. *Journal of Mechanisms and Robotics*, 9(2):021011, 2017.

E. Glassman, A. L. Desbiens, M. Tobenkin, M. Cutkosky, and R. Tedrake. Region of attraction estimation for a perching aircraft: A lyapunov method exploiting barrier certificates. In *Robotics and Automation (ICRA), 2012 IEEE International Conference on*, pages 2235–2242. IEEE, 2012.

D. W. Haldane, M. Plecnik, J. K. Yim, and R. S. Fearing. Robotic vertical jumping agility via series-elastic power modulation. *Science Robotics*, 1(1), 2016.

D. W. Haldane, J. K. Yim, and R. S. Fearing. Repetitive extremeacceleration (14-g) spatial jumping with salto-1p. In *Submitt. to IEEE Int. Conf. Intell. Robot. Syst*, 2017.

M. Hamamoto, Y. Ohta, K. Hara, and T. Hisada. A fundamental study of wing actuation for a 6-in-wingspan flapping microaerial vehicle. *Robotics, IEEE Transactions on*, 26 (2):244–255, April 2010. ISSN 1552-3098. doi: 10.1109/TRO.2010.2041266.

R. Hayashi and S. Tsujio. High-performance jumping movements by pendulum-type jumping machines. In *Intelligent Robots and Systems, 2001. Proceedings. 2001 IEEE/RSJ International Conference on*, volume 2, pages 722–727. IEEE, 2001.

S. Ho, H. Nassef, N. Pornsinsirirak, Y.-C. Tai, and C.-M. Ho. Unsteady aerodynamics and flow control for flapping wing flyers. *Progress in Aerospace Sciences*, 39(8):635–681, 2003.

W. Hoburg and R. Tedrake. System identification of post stall aerodynamics for uav perching. In *AIAA Infotech@ Aerospace Conference and AIAA Unmanned... Unlimited Conference*, page 1930, 2009.

D. Hohm and M. Ropp. Comparative study of maximum power point tracking algorithms. *Progress in photovoltaics: Research and Applications*, 11(1):47–62, 2003.

A. E. Holness, H. Bruck, and S. K. Gupta. Design of propeller-assisted flapping wing aerial vehicles for enhanced aerodynamic performance. In *ASME IDETC/CIE, 39th ASME Mechanism and Robotics Conference*. ASME, August 2015. DETC2015-47577.

A. E. Holness, E. Steins, M. Peckerar, H. Bruck, and S. K. Gupta. Performance characterization of multifunctional wings with integrated flexible batteries for flapping wing unmanned air vehicles. In *ASME IDETC/CIE, 40th ASME Mechanism and Robotics Conference*. ASME, August 2016. DETC2016-6037.

A. E. Holness, H. A. Bruck, and S. K. Gupta. Characterizing and modeling the enhancement of lift and payload capacity resulting from thrust augmentation in a propeller-assisted flapping wing air vehicle. *International Journal of Micro Air Vehicles*, 10(1): 50–69, 2018a. doi: 10.1177/1756829317734836. URL https://doi.org/10.1177/1756829317734836.

A. E. Holness, H. A. Bruck, H. Solheim, and S. K. Gupta. A design framework realizing multifunctional wings for flapping wing air vehicles using solar cells. *International Journal of Micro Air Vehicles*, 2018b. Submitted for review.

T. Hubel and C. Tropea. Experimental investigation of a flapping wing model. *Experiments in Fluids*, 46(5):945–961, 2009. ISSN 0723-4864. doi: 10.1007/s00348-008-0599-9. URL http://dx.doi.org/10.1007/s00348-008-0599-9.

P. Ifju, D. Jenkins, S. Ettinger, Y. Lian, W. Shyy, and M. Waszak. Flexible-wing-based micro air vehicles. In *40th AIAA Aerospace Sciences Meeting & Exhibit*, page 705, 2002.

F. Iida, R. Dravid, and C. Paul. Design and control of a pendulum driven hopping robot. In *Intelligent Robots and Systems, 2002. IEEE/RSJ International Conference on*, volume 3, pages 2141–2146. IEEE, 2002.

G. Jiang and R. Voyles. Hexrotor uav platform enabling dextrous aerial mobile manipulation. In *Proc. International Micro Air Vehicle Conference and Competitions*, 2013.

A. Jones and H. Babinsky. Unsteady lift generation on rotating wings at low reynolds numbers. *Journal of Aircraft*, 47(3):1013–1021, 2010.

A. Jones, C. Pitt Ford, and H. Babinsky. Three-dimensional effects on sliding and waving wings. *Journal of Aircraft*, 48(2):633–644, 2011.

N. J. Kohut, A. O. Pullin, D. W. Haldane, D. Zarrouk, and R. S. Fearing. Precise dynamic turning of a 10 cm legged robot on a low friction surface using a tail. In *Robotics and Automation (ICRA), 2013 IEEE International Conference on*, pages 3299–3306. IEEE, 2013a.

N. J. Kohut, D. Zarrouk, K. C. Peterson, and R. S. Fearing. Aerodynamic steering of a 10 cm high-speed running robot. In *Intelligent Robots and Systems (IROS), 2013 IEEE/RSJ International Conference on*, pages 5593–5599. IEEE, 2013b.

M. Kovač, O. Fauria, J.-C. Zufferey, D. Floreano, et al. The epfl jumpglider: A hybrid jumping and gliding robot with rigid or folding wings. In *Robotics and Biomimetics (ROBIO), 2011 IEEE international conference on*, pages 1503–1508. IEEE, 2011.

J. Kucherovsky, G. Simmons, J. Miller, and C. Mlnarik. Method of making a thin film battery, Apr. 30 2002. URL http://www.google.com/patents/US6379835. US Patent 6,379,835.

X. Li, Z. Jiang, H. Li, Y. Mo, M. Zou, and Q. Huang. Dynamic stability control for a bio-robot with primates-inspired active tail. In *Mechatronics and Automation (ICMA), 2015 IEEE International Conference on*, pages 2035–2040. IEEE, 2015.

T. Libby, T. Y. Moore, E. Chang-Siu, D. Li, D. J. Cohen, A. Jusufi, and R. J. Full. Tail-assisted pitch control in lizards, robots and dinosaurs. *Nature*, 481(7380):181, 2012.

R. Madangopal, Z. A. Khan, and S. K. Agrawal. Biologically inspired design of small flapping wing air vehicles using four-bar mechanisms and quasi-steady aerodynamics. *Journal of Mechanical Design*, 127(4):809–816, 2004.

P. Mancini, F. Manar, K. Granlund, M. V. Ol, and A. R. Jones. Unsteady aerodynamic characteristics of a translating rigid wing at low reynolds number. *Physics of Fluids (1994-present)*, 27(12):123102, 2015a.

P. M. Mancini, A. R. Jones, K. O. Granlund, and M. V. Ol. Unsteady aerodynamic response of a rapidly started flexible wing. *International Journal of Micro Air Vehicles*, 7(2):147–157, 2015b.

S. Mintchev and D. Floreano. Adaptive morphology: A design principle for multimodal and multifunctional robots. *IEEE Robotics & Automation Magazine*, 23(3):42–54, 2016.

J. Moore and R. Tedrake. Powerline perching with a fixed-wing uav. In *AIAA Infotech@ Aerospace Conference and AIAA Unmanned... Unlimited Conference*, page 1959, 2009.

D. Mueller, H. Bruck, and S. K. Gupta. Measurement of thrust and lift forces associated with drag of compliant flapping wing for micro air vehicles using a new test stand design. *Experimental Mechanics*, 50(6):725 – 735, 2010.

F. Muijres, L. Johansson, R. Barfield, M. Wolf, G. Spedding, and A. Hedenström. Leading-edge vortex improves lift in slow-flying bats. *Science*, 319(5867):1250–1253, 2008.

A. Noth et al. *Design of solar powered airplanes for continuous flight*. PhD thesis, Ecole Polytechnique Fdrale de Lausanne, Suisse, 2008.

A. A. Paranjape, S.-J. Chung, and J. Kim. Novel dihedral-based control of flapping-wing aircraft with application to perching. *IEEE Transactions on Robotics*, 29(5): 1071–1084, 2013.

J.-H. Park, E. Yang, C. Zhang, and S. Agrawal. Kinematic design of an asymmetric in-phase flapping mechanism for mavs. In *Robotics and Automation (ICRA), 2012 IEEE International Conference on*, pages 5099–5104, May 2012. doi: 10.1109/ICRA.2012.6225028.

A. Patel and M. Braae. Rapid acceleration and braking: Inspirations from the cheetah's tail. In *Robotics and Automation (ICRA), 2014 IEEE International Conference on*, pages 793–799. IEEE, 2014.

M. Peckerar, Z. Dilli, M. Dornajafi, N. Goldsman, Y. Ngu, R. B. Proctor, B. J. Krupsaw, and D. A. Lowy. A novel high energy density flexible galvanic cell. *Energy Environ. Sci.*, 4:1807–1812, 2011a. doi: 10.1039/C1EE01075A. URL http://dx.doi.org/10.1039/C1EE01075A.

M. Peckerar, M. Dornajafi, Z. Dilli, N. Goldsman, Y. Ngu, B. Boerger, N. Van Wyck, J. Gravelin, B. Grenon, R. B. Proctor, et al. Fabrication of flexible ultracapacitor/galvanic cell hybrids using advanced nanoparticle coating technology. *Journal of Vacuum Science & Technology B*, 29(1):011008, 2011b.

I. Penskiy, P. Samuel, J. S. Humbert, and S. Bergbreiter. A bio-inspired active tail control actuator for nano air vehicles. In *Robotics and Automation (ICRA), 2012 IEEE International Conference on*, pages 4635–4640. IEEE, 2012.

M. Percin, B. van Oudheusden, H. Eisma, and B. Remes. Three-dimensional vortex wake structure of a flapping-wing micro aerial vehicle in forward flight configuration. *Experiments in Fluids*, 55(9):1–16, 2014.

A. Perez-Rosado, G. Griesinger, H. Bruck, and S. K. Gupta. Performance characterization of multifunctional wings with integrated solar cells for miniature air vehicles. In *ASME IDETC/CIE, 38th Mechanisms and Robotics Conference*. ASME, August 2014. DETC2014-34719.

A. Perez-Rosado, H. Bruck, and S. K. Gupta. Integrating solar cells into flapping wing air vehicles for enhanced flight endurance. *Journal of Mechanisms and Robotics*, 2015a.

A. Perez-Rosado, H. Bruck, and S. K. Gupta. Enhancing the design of solar-powered flapping wing air vehicles using multifunctional structural components. In *ASME IDETC/CIE, 39th ASME Mechanism and Robotics Conference*, pages V05BT08A016–V05BT08A016. ASME, August 2015b. DETC2015-47570.

A. Perez-Rosado, R. D. Gehlhar, S. Nolen, S. K. Gupta, and H. A. Bruck. Design, fabrication, and characterization of multifunctional wings to harvest solar energy in flapping wing air vehicles. *Smart Materials and Structures*, 24(6):065042, 2015c.

D. J. Pines and F. Bohorquez. Challenges facing future micro-air-vehicle development. *Journal of Aircraft*, 43(2):1–3, March-April 2006.

M. F. Platzer, K. D. Jones, J. Young, and J. S. Lai. Flapping wing aerodynamics: progress and challenges. *AIAA journal*, 46(9):2136–2149, 2008.

C. Powers, D. Mellinger, A. Kushleyev, B. Kothmann, and V. Kumar. Influence of aerodynamics and proximity effects in quadrotor flight. In *Experimental robotics*, pages 289–302. Springer, 2013.

A. Ramezani, S.-J. Chung, and S. Hutchinson. A biomimetic robotic platform to study flight specializations of bats. *Science Robotics*, 2(3), 2017. doi: 10.1126/scirobotics.aal2505. URL http://robotics.sciencemag.org/content/2/3/eaal2505.

J. Rayner. Form and function in avian flight. In R. Johnston, editor, *Current Ornithology*, volume 5 of *Current Ornithology*, pages 1–66. Springer US, 1988. ISBN 978-1-4615-6789-9. doi: 10.1007/978-1-4615-6787-5_1. URL http://dx.doi.org/10.1007/978-1-4615-6787-5_1.

J. W. Roberts, R. Cory, and R. Tedrake. On the controllability of fixed-wing perching. In *American Control Conference, 2009. ACC'09.*, pages 2018–2023. IEEE, 2009.

L. Roberts, H. Bruck, and S. K. Gupta. Autonomous loitering control for a flapping wing aerial vehicle with independent wing control. In *ASME IDETC/CIE, 38th Mechanisms and Robotics Conference*. ASME, August 2014. DETC2014-34752.

L. Roberts, H. Bruck, and S. K. Gupta. Modeling of dive maneuvers in flapping wing unmanned aerial vehicles. In *2015 IEEE International Symposium on Safety, Security, and Rescue Robotics*. October, August 2015.

L. Roberts, H. Bruck, and S. K. Gupta. Using a large 2 degree of freedom tail for autonomous aerobatics on a flapping wing unmanned serial vehicle. In *ASME IDETC/CIE, 40th ASME Mechanism and Robotics Conference*. ASME, August 2016. DETC2016-60387.

L. J. Roberts, H. A. Bruck, and S. Gupta. Modeling of dive maneuvers for executing autonomous dives with a flapping wing air vehicle. *Journal of Mechanisms and Robotics*, 9(6):061010, 2017.

W. S. Rone, W. Saab, and P. Ben-Tzvi. Design, modeling, and integration of a flexible universal spatial robotic tail. *Journal of Mechanisms and Robotics*, 10(4):041001, 2018.

C. Rose and R. Fearing. Comparison of ornithopter wind tunnel force measurements with free flight. In *Robotics and Automation (ICRA), 2014 IEEE International Conference on*, pages 1816–1821, May 2014. doi: 10.1109/ICRA.2014.6907097.

M. H. Rosen, G. le Pivain, R. Sahai, N. T. Jafferis, and R. J. Wood. Development of a 3.2g untethered flapping-wing platform for flight energetics and control experiments. In *2016 IEEE International Conference on Robotics and Automation (ICRA)*, pages 3227–3233, May 2016. doi: 10.1109/ICRA.2016.7487492.

A. Santamaria-Navarro, V. Lippiello, and J. Andrade-Cetto. Task priority control for aerial manipulation. In *Safety, Security, and Rescue Robotics (SSRR), 2014 IEEE International Symposium on*, pages 1–6. IEEE, 2014.

D. Scheiman, R. Hoheisel, D. J. Edwards, A. Paulsen, J. Lorentzen, P. Jenkins, S. Caruthers, S. Carter, and R. Walters. A path toward enhanced endurance of a uav using imm solar cells. In *Photovoltaic Specialists Conference (PVSC), 2016 IEEE 43rd*, pages 1095–1100. IEEE, 2016.

K. Schmidt-Nielsen. Locomotion: Energy cost of swimming, flying, and running. *Science*, 177(4045):222–228, 1972. ISSN 00368075, 10959203. URL http://www.jstor.org/stable/1734532.

J. K. Shiau, D. M. Ma, P. Y. Yang, G. F. Wang, and J. H. Gong. Design of a solar power management system for an experimental uav. *IEEE Transactions on Aerospace and Electronic Systems*, 45(4):1350–1360, Oct 2009. ISSN 0018-9251. doi: 10.1109/TAES.2009.5310303.

S. Shkarayev, D. Silin, G. Abate, and R. Albertani. Aerodynamics of cambered membrane flapping wings. In *48th AIAA Aerospace Sciences Meeting Including the New Horizons Forum and Aerospace Exposition*. AIAA, August 2010. doi:10.2514/6.2010-58.

W. Shyy, M. Berg, and D. Ljungqvist. Flapping and flexible wings for biological and micro air vehicles. *Progress in Aerospace Sciences*, 35(5):455 – 505, 1999. ISSN 0376-0421. doi: http://dx.doi.org/10.1016/S0376-0421(98)00016-5. URL http://www.sciencedirect.com/science/article/pii/S0376042198000165.

W. Shyy, P. Ifju, and D. Viieru. Membrane wing-based micro air vehicles. *Applied mechanics reviews*, 58(4):283–301, 2005.

W. Shyy, H. Aono, C. kwon Kang, and H. Liu. *An Introduction to Flapping Wing Aerodynamics*. Cambridge University Press, 2013. ISBN 9781139583916. URL http://dx.doi.org/10.1017/CBO9781139583916. Cambridge Books Online.

M. Silvestre, J. Morgado, P. Alves, P. Santos, P. Gamboa, and J. Pscoa. Low reynolds number propeller performance testing. In *5th International Conference on Fluid Mechanics and Heat & Mass*, 11 2014.

C. F. Solutions. Robird, Dec 2016. URL https://clearflightsolutions.com/methods/robirds.

A. Song, X. Tian, E. Israeli, R. Galvao, K. Bishop, S. Swartz, and K. Breuer. Aeromechanics of membrane wings with implications for animal flight. *AIAA journal*, 46(8): 2096–2106, 2008.

S. M. Swartz, J. Iriarte-Diaz, D. K. Riskin, and K. S. Breuer. *Evolutionary History of Bats*, A bird? A plane? No, it's a bat: an introduction to the biomechanics of bat flight 9, pages 317–352. Cambridge Studies in Morphology and Molecules: New Paradigms in Evolutionary Bio. Cambridge University Press, Cambridge, 2^{nd} edition, 2012. URL http://dx.doi.org/10.1017/CBO9781139045599.010.

M. J. Tarascio, M. Ramasamy, I. Chopra, and J. G. Leishman. Flow visualization of micro air vehicle scaled insect-based flapping wings. *Journal of Aircraft*, 42(2):385–390, March-April 2005.

Z. Teoh, S. Fuller, P. Chirarattananon, N. Prez-Arancibia, J. Greenberg, and R. Wood. A hovering flapping-wing microrobot with altitude control and passive upright stability. In *Intelligent Robots and Systems (IROS), 2012 IEEE/RSJ International Conference on*, pages 3209–3216, Oct 2012. doi: 10.1109/IROS.2012.6386151.

B. Theys, G. Dimitriadis, P. Hendrick, and J. De Schutter. Experimental and numerical study of micro-aerial-vehicle propeller performance in oblique flow. *Journal of Aircraft*, 2016.

A. L. Thomas. Why do birds have tails? the tail as a drag reducing flap, and trim control. *Journal of Theoretical Biology*, 183(3):247 – 253, 1996. ISSN 0022-5193. doi: http://dx.doi.org/10.1006/jtbi.1996.0218. URL http://www.sciencedirect.com/science/article/pii/S0022519396902180.

A. L. R. Thomas. On the aerodynamics of birds' tails. *Phil. Trans. R. Soc.*, 340:361–380, June 1993.

J. Thomas, M. Qidwai, P. Matic, R. Everett, A. Gozdz, M. Keennon, and J. Grasmeyer. Multifunctional structure-plus-power concepts. In *Paper# AIAA-2002-1239 (Paper presented at the 43rd AIAA/ASME/ASCE/AHS/ASC Structures, Structural Dynamics, and Materials Conference, Denver, CO, 2002)*, 2002.

J. Thomas, J. Polin, K. Sreenath, and V. Kumar. Avian-inspired grasping for quadrotor micro uavs. In *ASME 2013 International Design Engineering Technical Conferences and Computers and Information in Engineering Conference*, pages V06AT07A014–V06AT07A014. American Society of Mechanical Engineers, 2013.

J. Thomas, G. Loianno, K. Sreenath, and V. Kumar. Toward image based visual servoing for aerial grasping and perching. In *Robotics and Automation (ICRA), 2014 IEEE International Conference on*, pages 2113–2118. IEEE, 2014.

J. P. Thomas and M. A. Qidwai. The design and application of multifunctional structure-battery materials systems. *JOM Journal of the Minerals, Metals and Materials Society*, 57(3):18–24, 2005.

B. W. Tobalske. Biomechanics of bird flight. *The Journal of Experimental Biology*, 210: 3135–3146, September 2007.

T. V. Truong, Q.-V. Nguyen, and H. P. Lee. Bio-inspired flexible flapping wings with elastic deformation. *Aerospace*, 4(3):37, 2017.

J. R. Usherwood, T. L. Hedrick, and A. Biewener. The aerodynamics of avian take-off from direct pressure measurements in canada geese (branta canadensis). *Journal of Experimental Biology*, 206:4051–4056, 2003.

D. Viieru, J. Tang, Y. Lian, H. Liu, and W. Shyy. Flapping and flexible wing aerodynamics of low reynolds number flight vehicles. *AIAA paper*, 503:2006, 2006.

P. M. Wensing, A. Wang, S. Seok, D. Otten, J. Lang, and S. Kim. Proprioceptive actuator design in the mit cheetah: Impact mitigation and high-bandwidth physical interaction for dynamic legged robots. *IEEE Transactions on Robotics*, 33(3):509–522, 2017.

A. M. Wickenheiser and E. Garcia. Longitudinal dynamics of a perching aircraft. *Journal of Aircraft*, 43(5):1386–1392, 2006.

A. M. Wickenheiser and E. Garcia. Optimization of perching maneuvers through vehicle morphing. *Journal of Guidance, Control, and Dynamics*, 31(4):815–823, 2008.

J. Wu and M. Sun. The influence of the wake of a flapping wing on the production of aerodynamic forces. *Acta Mechanica Sinica*, 21(5):411–418, 2005. ISSN 1614-3116. doi: 10.1007/s10409-005-0064-4. URL http://dx.doi.org/10.1007/s10409-005-0064-4.

P. Wu, P. Ifju, and B. Stanford. Flapping wing structural deformation and thrust correlation study with flexible membrane wings. *AIAA Journal*, 48(9):2111–2122, September 2010.

W. Zhang and C. Hu. Solar cell as wings of different sizes for flapping-wing micro air vehicles. *International Journal of Micro Air Vehicles*, 8(4):209–220, 2016.

J. Zhao, T. Zhao, N. Xi, F. J. Cintrón, M. W. Mutka, and L. Xiao. Controlling aerial maneuvering of a miniature jumping robot using its tail. In *Intelligent Robots and Systems (IROS), 2013 IEEE/RSJ International Conference on*, pages 3802–3807. IEEE, 2013.

J. Zhao, T. Zhao, N. Xi, M. W. Mutka, and L. Xiao. Msu tailbot: Controlling aerial maneuver of a miniature-tailed jumping robot. *IEEE/ASME Transactions on Mechatronics*, 20(6):2903–2914, 2015.

L. Zhao, Q. Huang, X. Deng, and S. P. Sane. Aerodynamic effects of flexibility in flapping wings. *Journal of The Royal Society Interface*, August 2009. ISSN 1742-5689. doi: 10.1098/rsif.2009.0200. 10.1098/rsif.2009.0200.